OPTOELECTRONIC SHAPE SENSING FOR FLEXIBLE CONTINUUM ROBOTS

A THESIS SUBMITTED FOR THE DEGREE OF DOCTOR OF PHILOSOPHY

BY

DALIA OSMAN

DEPARTMENT OF MECHANICAL AND AEROSPACE ENGINEERING, BRUNEL UNIVERSITY LONDON

MARCH 2025

ACKNOWLEDGEMENT

I would like to express my greatest gratitude to my supervisor Dr Yohan Noh for the immeasurable impact that he has had on my PhD journey. His profound mentorship and invaluable knowledge has allowed me to develop all aspects of my skill, proficiency, and personal growth as a researcher. He has always dedicated much of his time for my guidance and has pushed me to achieve to the best of my abilities. He has been consistently supportive, and always patient and encouraging, especially during the more challenging parts of the last four years, and I truly would not have been able to reach this point without his mentorship, and for this I am deeply grateful to him.

I express my thanks to my whole supervisory team for their guidance and direction, and to the department for their support in my project activities. I also express my thanks to the Engineering and Physical Science Research Council for making the outcomes of this project possible through their funding (grant number: EP/T518116/1).

ABSTRACT

The advancement of flexible continuum robots has enabled their use in complex environments such as minimally invasive surgery (MIS), industrial inspection, and aerospace maintenance. However, a key challenge remains in achieving real-time shape sensing for precise and stable control and navigation, due to the flexible and curvature-based nature of these robotic structures, as opposed to rigid robots. This research presents the use of optoelectronic sensors, more specifically, a photo-reflective sensing component, to develop a novel variation of shape sensing techniques, for integration into simple planar robot structures, as well as flexible tendon actuated robots.

The sensing principle is based on proximity detection of the optoelectronic sensor to a reflector, a number of which are integrated into the robotic structures. As the robot moves, the proximity changes to the sensor are recorded as a voltage varying signal, which is used to estimate the curvature, or shape, of the robot. Optoelectronic shape sensing overcomes some of the shortcomings of the standard shape sensing: The sensing is non-contact, and based purely on light intensity detection, meaning the sensors are not affected by material properties or load limitations, so that calibration remains intact in almost any scenario. Real time sensing can be achieved through the sensors high sampling rate, which do not require an amplifier. Development of the shape sensing technique is presented, including sensor characterisation, theoretical modelling based on gaussian light intensity, development of experimental rigs and novel calibration platforms for planar and tendon actuated robots integrating this shape sensing, as well as eventual development of a novel technique to target improved shape sensor performance using specialised reflector shapes. The results demonstrate significant improvements in accuracy, miniaturisation, simplicity of integration, adaptability, and robustness, making optoelectronic shape sensing a viable alternative for future applications using continuum robots.

Table of Contents

LIST OF FIGURES

LIST OF TABLES

NOMENCLATURE

Symbol	Unit	Description
α	°	Yaw Orientation
β	°	Pitch Orientation
γ	°	Roll Orientation
φ	°	Angle of reflector surface made with optoelectronic sensor
ω		Cross sectional radius of reflected gaussian light beam
Φ_c		Theoretical flux collected by PT
h_e	mm	Distance between optoelectronic sensor and reflector.
I		Gaussian intensity of reflected LED light
I_o		Initial gaussian intensity of beam emitted by LED
k_v		Theoretical sensor voltage conversion factor
P		Power of reflected LED light
P_E		Initial power emitted by the LED
R		Surface reflectance rate of reflector
R_1	Ω	LED resistance in optoelectronic sensor component
R_2	Ω	PT resistance in optoelectronic sensor component
s	mm	Lateral distance of optoelectronic sensor from the central rotational axis of reflector surface
S_{area}	mm^2	Circular surface area of PT on the optoelectronic sensor
V_{th}	V	Theoretical optoelectronic sensor voltage

CHAPTER 1: INTRODUCTION

Figure 1.1: (Left) Remote inspection for aircraft engines, (Tsinghua University, China, 2022) [123] and (Right) machine maintenance using soft snake-like robots (Rolls Royce, 2020)[124].

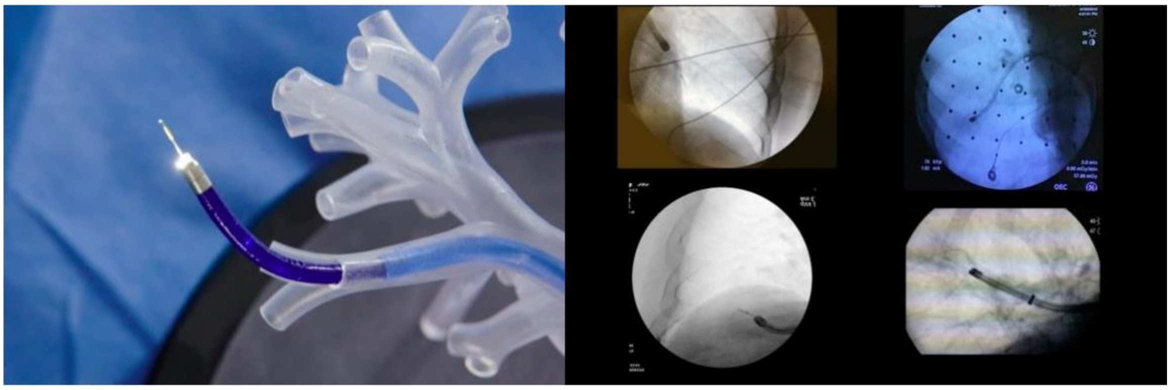

Figure 1.2: Example of concentric tube continuum robotic endoscope used for bronchoscopy, biopsies, and ultrasound scanning (Auris Monarch Platform)[50]

1.1 Motivation

Over the last few decades, there has been a great transformation in the development of advanced soft continuum robotic systems. Soft continuum robots are specialised for navigating complex trajectories and can adapt to various environments, as they are able to form three dimensional continuous curvatures and have high dexterity. They are utilised in a number of industries and fields. These include the manufacturing industry, maintenance and repair within the aerospace industry, medical field, including medical procedures and minimally invasive surgery (MIS), search and rescue operations for natural disasters as well as hazardous environments, and in fields of exploration to reach inaccessible areas. Figure 1.1 shows an example of flexible robots used in inspection and maintenance in aircraft and

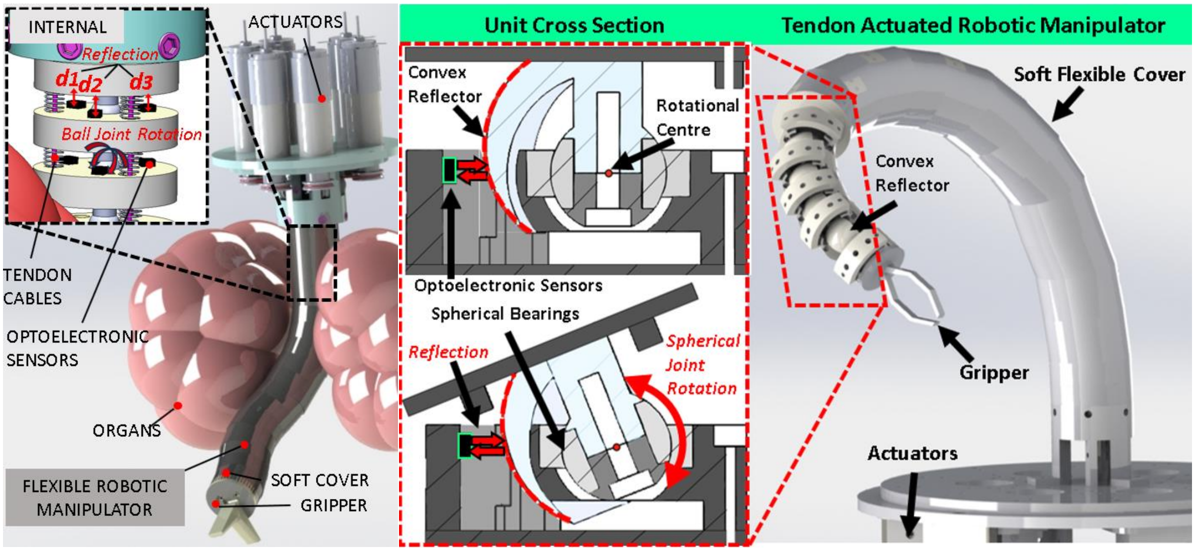

Figure 1.3: Concept images for optoelectronic based shape sensing for tendon actuated robots. Reflective optoelectronic sensors can be used to estimate changing orientations based on proximity to a reflective surface, as signal varies with changing light intensity [115][114].

machines, while Figure 1.2 shows an example of a robotically actuated flexible manipulator used in bronchial MIS [1].

However, one of the main challenges that face the use of these flexible robotic manipulators, amongst other factors such as force feedback, biocompatibility, and sensor integrability, is that of position control [2]. It is important to have a sense of the position and shape of the manipulator inside the pathways of their trajectories, to ensure accuracy and safety in use. Previously, robotic manipulators employed open loop control systems, but it is important that these manipulators utilise closed loop feedback control in order to ensure stability and accuracy in maintaining position control through a control system. This is commonly done by adopting different ***shape sensing*** techniques that can be used as feedback for such control systems. Integrating shape sensing into these robots ensures precise position control and real-time curvature estimation of the robot, enhancing safety and accuracy. The design of shape sensing systems for continuum robots have used a variety of sensor types. The types of soft continuum manipulators in terms of structure, as well as intended applications, often determines different means of shape sensing and the type of sensor used.

Advancements in shape sensing have been achieved over the recent years, utilising various sensor types. For example, inertial sensors have been integrated along continuum robots [3],

[4], [5], [6], [7], [8]; however, they have been known to cause shape sensing error due to magnetic interference, gyroscopic drift as well as mechanical vibration. Similarly, magnetic sensors integrated along continuum robots [9][10] have also been known to suffer from magnetic interference, as well as sensitivity to electrical equipment. Size and rigidity of such components also hinder miniaturisation of the robot system. Strain sensors such as those made with silicone and carbon nanotubes, as well as conductive liquids, polymers and hydrogels are able to detect shape through deformation of these stretch strain sensors [11], [12], [13], [14], [15]. These are thin and flexible and can easily integrate into soft continuum robot systems. However, some of the concerns are the material's inhomogeneity, signal non-linearity and large hysteresis. Assumption of constant curvature is required for modelling for shape estimation, and therefore more complex curvatures cannot be estimated using such shape sensing systems. Alternatively, Fibre Bragg gratings (small gratings integrated into fibres) are most commonly integrated into some of the narrowest continuum robots, due to their flexibility and slender dimensions [16], [17], [18], [19], [20], [21]. These measure strain through deformation, and so also display error during complex curvatures or large bending angles of the continuum robot, and deformation of these sensors must remain within their elastic limit in order to maintain calibration conditions. They have also been known to display error during use of compliant materials or and have high equipment cost requirements, of up to thousands of pounds [22]. It emerges that there is a vast set of literature on different techniques for shape sensing using a variety of methods, which will be explored in the Chapter 2, in which it is established that a gap exists within the design of shape sensing for continuum robotic application, which will be addressed in this thesis. The proposed solution utilises novel optoelectronic shape sensing techniques, that preserves the advantages while overcoming the limitations identified in existing techniques. Figure 1.3 illustrates some concepts for this that will be further explored in the following chapters. The proposed optoelectronic sensors comprise of a coupled light emitting diode (LED) and phototransistor (PT), which emit and detect reflected infrared light. It can be more specifically referred to as a photo-reflective sensor. The sensing principle is based on proximity detection to a reflector. For example, as

shown in Figure 1.3, sets of optoelectronic sensors are fixed into each unit of a tendon actuated robot. As the robot bends, the proximity of the reflector to the sensor will vary, depending on the orientation (pitch and roll), and this will be detected as a varying voltage signal in each optoelectronic sensor. From these voltage values, the orientation in each unit can be estimated, and the curvature of the manipulator, as well as the tip pose can be reconstructed.

1.2 Aims & Objectives

The **aim** in this thesis is to find a solution for a shape sensing method for continuum robots that is simple, cheap, miniaturised, computationally inexpensive, and easily integrated - combining these qualities to develop a robotic application that can utilise this optimised method of shape sensing. It also aims to demonstrate how any optoelectronic sensor can be integrated in various configurations into robotic applications, from simple joint angle sensors to multi-segmented flexible robots and how to optimise the sensor response through optimisation of various design parameters, to improve sensitivity and measurement range.

To achieve these aims, a number of **objectives** are defined:

1. Carry out a study to characterize the behaviour of the proposed optoelectronic sensor and explore how various parameters such as reflector colour and shape, circuit properties, and geometrical positioning of the optoelectronic sensor component affect the output of the optoelectronic sensor.

2. Develop a mathematical model to describe the sensor's response and its relationship the mentioned parameters and compare this to experimental values to validate potential use of the model for optimising design of subsequent optoelectronic shape sensing for a number of robotic applications.

3. Develop a planar joint angle sensor to test the feasibility of the optoelectronic sensor for shape sensing in continuum robots, implementing some of the concepts developed in the sensor study

4. Develop an optoelectronic shape sensing system that can be integrated into a tendon-actuated continuum robot to measure orientation in two directions and optimize sensor configuration for accurate shape reconstruction.

5. Further explore the adaptability of the optoelectronic shape sensing system, through various sensing configurations and robotic design, with the aim of improving shape sensing performance, to demonstrate how the shape sensing system can be developed as a viable alternative for some of the standard shape sensing techniques used for continuum robots.

1.3 Contributions to Knowledge

In completing the objectives within this thesis to achieve the proposed aims by addressing the limitations of existing shape sensing techniques, the work provides innovative solutions that enhance the accuracy, efficiency, and applicability of optoelectronic based shape sensing for flexible continuum robots. The following **novel advancements** have been achieved, and contribute to the research in the area of robotic shape sensing in the following ways:

1. A body of work studying the behaviour of optoelectronic sensors, more specifically photo-reflective sensors was carried out. This included extensive experimental studies to explore the effect of various circuit properties, reflective surface properties such as colour and shape, as well as proximity and angle of a reflective surface to the photo-reflective sensor. With this extensive body of data, one can easily extract the required design parameters or circuit properties to achieve the desired optoelectronic sensor response, for a variety of applications, from simple proximity sensing, joint angle sensing, or multidimensional shape sensing.
2. An original theoretical mathematical model was developed, based on a series of gaussian light intensity models developed for fibre optics. This is adapted to a photo-reflective sensor against a reflective surface, to estimate the flux collected by the sensor depending on various parameters such as surface proximity, angle, or reflectivity. The model is validated against experimental values and closely approximates the real

experimental data. Based on this one may use the mathematical model to propose further optoelectronic sensing configuration beyond that demonstrated in the experimental sensor study and establish feasibility for any proposed robotic design utilising optoelectronic sensing.

3. A one axis joint angle sensor was developed, comprising a simple finger-like link structure, for robotic application. This design offered an alternative to some of the common robotic joint angle sensors, that can be simply integrated directly into robotic joint structures, have a large voltage variation without an amplifier and with low level noise, and offer simple fabrication at considerably low cost in comparison.
4. A single segment tendon actuated robot was created, integrating a novel optoelectronic shape sensing technique. Three optoelectronic sensors per unit of the segment were fitted, and the flat surface of the consecutive unit was used as the reflector. Through motion of the robotic segment, each set of three sensors detected the varying proximity to the upper unit and were used to estimate bending in two orientations. A novel calibration technique, that involves calibrating three sensors per unit successively along the structure of the robotic segment using a motorised motion pattern ensured improved calculation of a calibration matrix, with improved orientation estimation results when compared to an IMU sensor. This shape sensing technique offers sensing that is non-contact, and based purely on light intensity detection, meaning the sensors are not affected by material properties or load limitations and have a hysteresis of almost zero, meaning calibration of the sensors can remain intact in almost any scenario and any complex curvatures. Real time sensing can be achieved through the sensors' high sampling rate, which do not require an amplifier. Photo-reflective sensor are miniature, easy to integrate, and low is cost. Compared to some other robotic structures integrating shape sensing, results showed comparable performance, with maximum RMSE of 3.23° with non-linear fitting in tip orientation estimation.
5. An experimental study was completed exploring how to improve joint angle sensor performance by adapting the geometry of the reflective surface. In using a curved

surface, the optoelectronic sensor response is adaptable, in terms of sensor sensitivity and range, and the technique to achieve the desired response is explored in this study through the design of multiple curved surface reflectors. A 4-link structure is developed to evaluate this concept, and results showed feasibility in use of this technique for planar shape sensing. Results show improved performance in sensing range compared to other joint angle sensors, demonstrating a case with 140° measurement range with 3.5V voltage variation. In all the results provided reasonable basis for the application of curved reflectors in continuum robots for measuring orientation in three dimensions, beyond the planar case.

6. Another single segment tendon actuated robot is developed, integrating a new optoelectronic shape sensing technique based on the use of a curved, spherical reflector. This is based on the prior study in using a curved reflector to improve sensor response in a one-axis joint angle sensor. A pair of sensors per unit of the robotic segment opposing a spherical reflector in each unit is able to measure two orientations in three-dimensional space. The technique offers an alternative shape sensing configuration, utilising a pair of sensors rather than three per disk, and showed comparable results, with a maximum RMS error of 3.27° for tip orientation estimation.
7. A two-segment tendon actuated robot is created, also integrating the spherical-reflector based optoelectronic shape sensing. Improved performance through robot design modifications, circuit modifications, and PCB design is achieved. A power switching circuit is integrated into the system, which alternates power between sets of optoelectronic sensors along the robot manipulator to eliminate interference of signals between each set of sensors, leading to more accurate calibration and shape sensing estimation.

1.4 Thesis Structure

This thesis is divided into seven chapters. While the current Chapter 1 introduces the project motivation and aims, with the literature review in Chapter 2, the subsequent chapters (Chapter 3 – 6) describe bodies of work leading to the eventual final design of an optoelectronic based shape sensing technique integrated onto a multi-segment tendon actuated robot. The outcomes of these bodies of work established in Chapter 3-6 have been published in conference and journal papers. Chapter 3 introduces the basics of the optoelectronic sensor component, and a study into the characteristics of this sensor type as well as the derivation of the mathematical model of the sensor behaviour. In understanding the workings of this sensor and how to manipulate various parameters to gain a desired sensor output. Chapter 4 moves on to the design of a simple one-axis optoelectronic joint angle measurement sensor, and the design and testing of a tendon actuated robot with integrated optoelectronic shape sensing for shape estimation in two orientations. Based on these results, Chapter 5 highlights improvements to be made to the robotic system and shape sensing system design, and this is realised through falling back to the design of a new simple one-axis optoelectronic joint angle sensor, which this time makes use of a curved reflective surface. This allowed progression into the development of an optoelectronic shape sensing system integrated into a tendon actuated robot, utilising a curved, spherical reflector. A final two-segment tendon actuated robot with an improved version of the optoelectronic shape sensing system with a spherical reflector is integrated and various design improvements are exhibited in Chapter 6. The final chapter consolidates on the project and discuss potential for future work. The flow chart in Fig 1.4 below demonstrates how the chapters flow into one another.

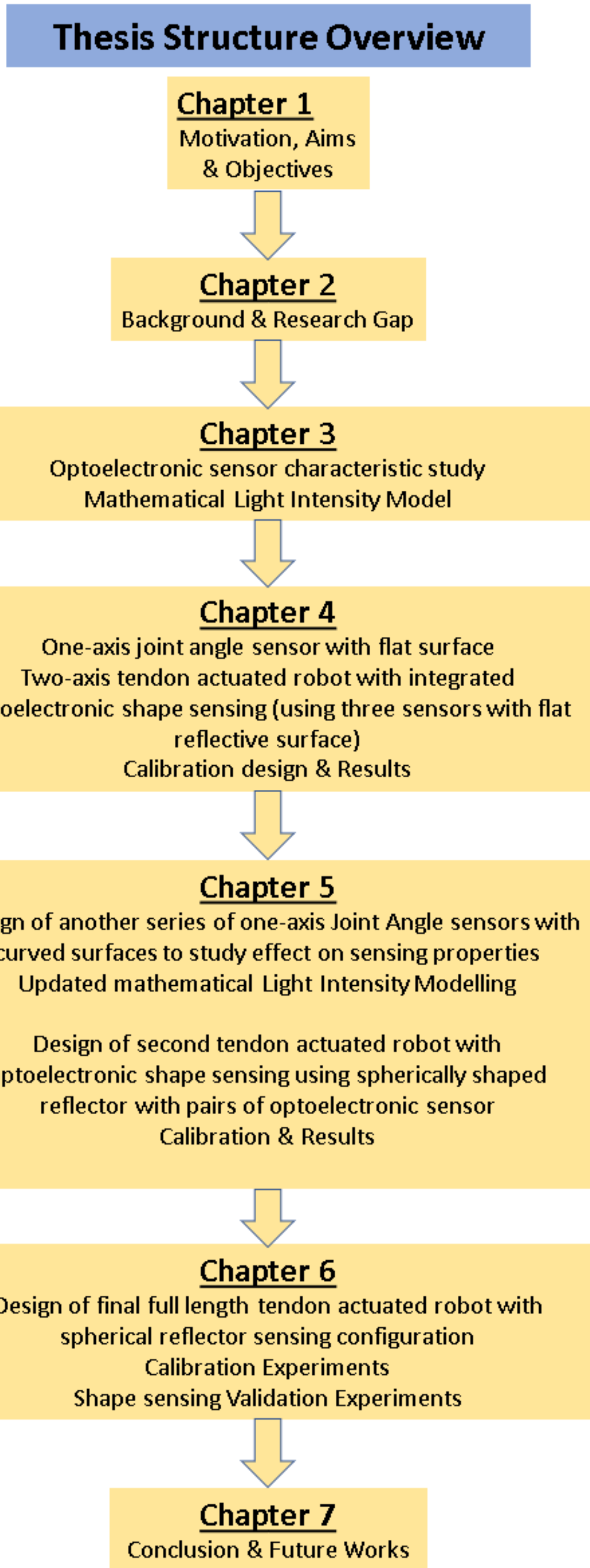

Figure 1.4: Flow chart showing various bodies of work leading to the development of the final design for a two-segment tendon actuated robot with optoelectronic shape sensing.

1.5 Publications

Published works (Peer reviewed Journals, Letters and Conferences) as a result of the research presented in this thesis.

TABLE 1.1 List of Published Works

1.	Conference, Presented online, Sep 2020	D. Osman, X. Du, W. Li and Y. Noh, "An Optical Joint Angle Measurement Sensor based on an Optoelectronic Sensor for Robot Manipulators," 2020 8th International Conference on Control, Mechatronics and Automation (ICCMA), Moscow, Russia, 2020, pp. 28-32, doi: 10.1109/ICCMA51325.2020.9301526.
2.	Published Journal Paper	D. Osman, X. Du, W. Li and Y. Noh, "Development of an Optical Shape Sensing Method Using Optoelectronic Sensors for Soft Flexible Robotic Manipulators in MIS," in IEEE Transactions on Medical Robotics and Bionics, vol. 4, no. 2, pp. 343-347, May 2022, doi: 10.1109/TMRB.2022.3155200.
3.	Published Letter Article	D. Osman, W. Li, X. Du, T. Minton and Y. Noh, "Miniature Optical Joint Measurement Sensor for Robotic Application Using Curvature-Based Reflecting Surfaces," in IEEE Sensors Letters, vol. 6, no. 5, pp. 1-4, May 2022, Art no. 3501304, doi: 10.1109/LSENS.2022.3169915.
4.	Published Conference Paper, Presented in Ioannina, Greece, Sep 2022	D. Osman, W. Li, X. Du, T. Minton and Y. Noh, "Prototype of An Optoelectronic Joint Sensor Using Curvature Based Reflector for Body Shape Sensing," 2022 IEEE-EMBS International Conference on Wearable and Implantable Body Sensor Networks (BSN), Ioannina, Greece, 2022, pp. 1-4, doi: 10.1109/BSN56160.2022.9928463.
5.	Published Journal paper	D. Osman, X. Du, T. Minton, and Y. Noh, “Shape sensing for continuum robotics using optoelectronic sensors with convex reflectors,” Electronics, vol. 13, no. 7, p. 1253, Mar. 2024. doi:10.3390/electronics13071253

CHAPTER 2: BACKGROUND

2.1 Introduction

Before beginning to construct the proposed integrated optoelectronic shape sensing system for a robotic manipulator, it was important to review the current literature and the state of the art of robotic shape sensing. This was done in stages in this chapter, looking at flexible continuum manipulators in terms of structure, actuation and shape sensing. These are discussed in sections 2.3, 2.4 and 2.5. From this, we can identify gaps for which innovation and improvement can be made, as well as identify specifications and standards of a proposed design. This research gap is discussed in section 2.6. Moving forward, it would be reasonable to establish a suitable sensor, hence a review of currently available sensors would be appropriate, which is explored in the following section, 2.6.

2.2 Background of Continuum Robotics

Continuum Robotics has a large market worldwide, due to these vast number of applications. One of the largest markets is for Inspection and Maintenance Robots (such as shown in Figure 1.1), which was valued at $2.75 billion in 2022, and this is expected to reach $8.27 billion by 2030 [23]. Continuum robots used in industry for engine repairs and maintenance reduce the need to disassemble and assemble large turbine engine components. This saves on maintenance and repair costs, as well as reduces hazardous manual labour. Components can last longer through more regular maintenance using these inspection flexible manipulators, and this saves on material cost, and is more environmentally friendly. A second large industry in which continuum robots are used are within the medical industry, specifically minimally invasive surgery (MIS). The global medical robotic systems market size was valued at USD 25.6 billion in 2023 and is expected to expand at a (CAGR) of 16.9% from 2023 to 2030, to revenue forecast of 76.4 billion USD in [24]. MIS has largely become the standard for many medical procedures, such as neurosurgery, cardiac, orthopaedic, urological, gynaecological, and ocular procedures [25], and involves inserting flexible tools through small incisions in the body as well as natural orifices, that are guided to the targeted location where the surgeon may carry out the procedure. The introduction of robotic MIS has transformed the global healthcare industry, through faster recovery and rehabilitation of patients due to reduced blood loss and smaller surgical wounds, leading to better efficiency for healthcare institutions [26]. It is clear that there is importance in ensuing the utilisation of continuum robots in these important industries is enhanced through more robust, safe, and accurate control, that can be achieved through integration of improved shape sensing systems.

2.3 Structure of Continuum Robots

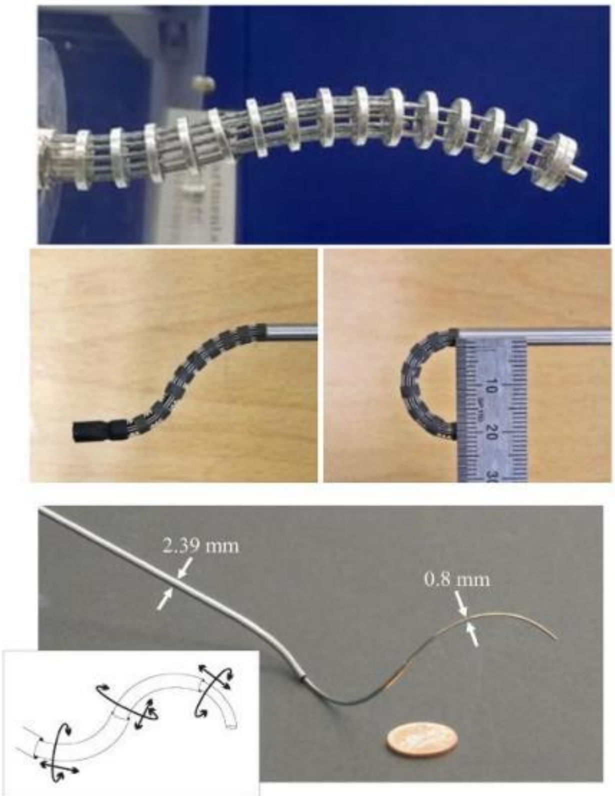

Figure 2.1: (a) Single backbone tendon actuated continuum robot with single elastic rod in centre; (b) multi-backbone endoscopic robot with multiple elastic elements; (c) concentric tube robot [39]

Flexible continuum robotic manipulators have been used over the last few decades for inspection and repairs of machines, search missions in natural disasters and hazardous environments, as well as most commonly in medical surgical procedures, such as endoscopy, laparoscopy, and colonoscopy. An important part of designing a continuum robot for a targeted application is to ensure it has the required safety features, stiffness, range of motion, force, and workspace, as well as size. The varying procedures and requirements have sprung a vast range of flexible manipulators that are adapted for these needs. These introduce features such as minimalistic structure and dexterity – making them perfect for use in confined or hard to reach spaces in an environment.

A continuum robot can be defined as a structure that can be actuated to form continuous curves [27], [28], [29]. Unlike serial robots that are made of discrete rigid links to form many actuated joints, a continuum robot has no rigid links and an infinite number of degrees of freedom (DOF). Closely tied to this is what can be described as a 'hyper redundant' serial robot - these have many links and a large number of DOFs to closely imitate continuous movement, but they aren't necessarily considered continuum robots. Snake like robots that utilise multiple discrete links as well as incorporating some elastic elements can be considered a 'hybrid' of sorts and are referred to as 'pseudo continuum' robots. However, in looking at their core structure, continuum robots can all in essence be classified into three main categories: (1) single backbone, (2) multi-backbone or (3) concentric tubes, (Fig. 2.1) as described in the work in [27].

Single backbone continuum robots consist of a single elastic element that runs centrally along that axis of the structure, that supports the actuation of the entire structure. Such manipulators are seen for example in the work in [30][31]. Kutzer et al demonstrate a dextrous manipulator, with a flexible hollow compliant cylinder forming the body of the manipulator, with notches slit at regular intervals to allow bending, constraining the bending motion to one plane [30].

Similar to this, there are multi-backbone robots. These consist of multiple elastic elements that run parallel along the structure but allow more refined actuation as well as increased stiffness [2]. An example is shown in the work of [32], where a multi backbone robot unit is made up of four elastic beams, separated by spacer disks. Here three of the elastic beams are used for actuation motion, while the central flexible beam assists with stiffness and load carrying.

Pseudo continuum single and backbone robots are common. For example, [33] uses a variable tension manipulator made of multiple discrete links to form rolling joints, with tendon cables that vary in tension to produce varying stiffnesses as well as actuation. [34] shows work on a nasal endoscopic robot, that consists of discrete cylindrical links with ball joints. These are wire driven, and are enclosed within a spring structure, hence can be referred to as another pseudo continuum robot manipulator. Work in [35] demonstrates an arthroscope, consisting of small cylindrical links with double joints. It is wire driven, and two Nitinol elastic wires are added for improved stiffness. Pseudo continuum robots are very common as opposed to purely continuum for a number of reasons: continuum robots have an infinite number of DOFs, meaning that it is substantially more difficult to actuate, and a variety of models must be applied, while pseudo continuum robots have discrete links that can be directly kinematically actuated. However, backbone-based designs allow a large range of motion and evidently can be configured for different applications.

The other categorical group is concentric tube continuum robots. These are made up of pre-curved tubes that are slotted into each other and can allow a set range of rotations and extensions for certain procedures, such as nasal biopsies [36], where paths through narrow and tortuous nasal passages require small, steep manoeuvres to avoid the risk of damaging the nasal membrane and surrounding tissue. Concentric tube robots have also been used in retinal eye surgeries [37] as well as neurosurgery [38]. Each tube in a concentric tube robot can translate and rotate independently and can be designed in smaller dimensions compared to single and multi-backbone robots, with the inner tubes having dimensions down to less than 1mm [39]. As each tube is pre-curved, each concentric tube robot must be specialized for specific paths, depending on the application [40]. Another limitation is the payload capabilities, although this depends on the procedural application [2][41]. Steerable needles are also considered a type of continuum manipulator and can be actuated to form curves to target location to carry out biopsies of different tissues.

2.4 Actuation

As discussed in the previous section, there are many types of continuum robotic manipulators. It can be said that their structure is closely tied to the method of actuation, and two often go hand in hand. Actuation allows the user to manipulate the robot through a workspace. This again is categorised into two main groups – intrinsically and extrinsically actuated continuum robots, as described in the review paper in [27].

Extrinsically actuated robotic manipulators are controlled external to the structure and have a means of transmitting the actuating force externally. An example of this is tendon or cable driven manipulators, such as in [40] or [42]. Tendon driven continuum robotic manipulators, as seen in Fig 2.1(a), are controlled using a number of cables that are coupled to motors at the base and fixed to sections of the body of the robot. As tendons shorten, the sections of the robot form curves. This is a common means of actuation for pseudo-continuum robots. Many concentric tube (Figure 2.1c) robot designs are also controlled externally, using a system of motors and transmission gears located at the base. There has also been work on magnetically actuated continuum robots, such as in [43]. Extrinsically actuated continuum robots can generally allow for reduction of the manipulator size, compared to intrinsically actuated, which has benefits in allowing a larger range of movement and facilitating for use in smaller spaces.

An example of an intrinsically actuated continuum robot (Figure 2.2) is one in which the means of actuation occurs within the structure, for example hydraulic or pneumatically

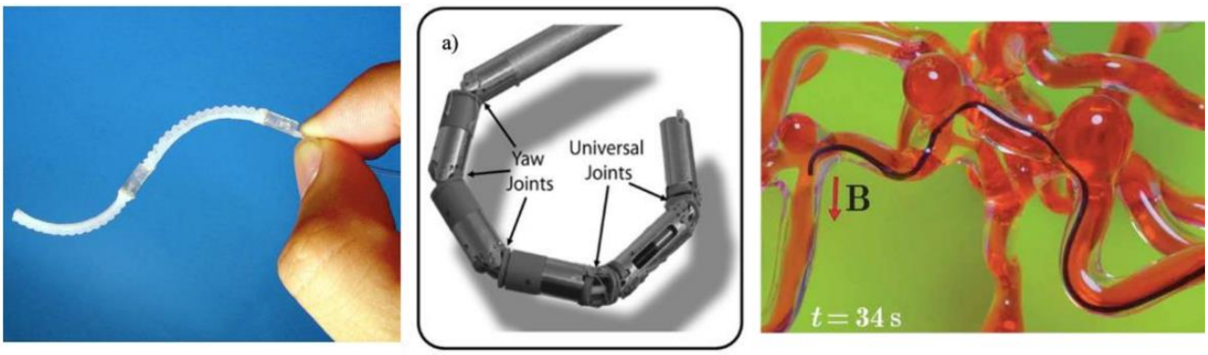

Figure 2.2: (a) Hydraulically active catheter [125], [126], [127], [128], [129]; (b) micromotor actuated links of snake-like manipulator [46] ;(c) magnetically actuated thin ferromagnetic manipulator [46].

actuated robots. Work in [44] demonstrates a catheter with hydraulically activated segments using saline solution, controlled using a pressure pulse control device (Figure 2.2a). Despite advances, hydraulically and pneumatically actuated manipulators are difficult to control with precision [45], however they are associated to softer and more compliant structures. This makes them ideal for minimising tissue damage in MIS but also means lower force transmission. Another example is the use of micromotors within the structure such as in the work of [46], [47] (Figure 2.2b). They demonstrate a multisegmented snake like manipulator, with individual links controlled with micromotors. This allows easier control and direct force transmission, compared to externally actuated techniques, as these may suffer from friction and inefficient force transmission, which makes control more complex. However, this design would not be suitable for many applications such as engine inspection or MIS procedures, due to scale and compatibility required for these applications.

Modelling for the control of continuum robots can be done in a number of ways, depending on the actuation and structure of the robot. The most common are using kinematic techniques, such as constant curvature or variable curvature models, or more mechanics-based models, such as energy-based modelling or elastic theory [48]. Although continuum robots have infinite DOF, the models are based on incrementality, and differ in computational expense, as well as ease of implementation into actuation. Control of the device by the user is often done remotely, using a console, for example as seen in the medical robotic device, the DaVinci surgical system [49], or using handheld controllers, such as in the Monarch system [50][1] using visual reality and sensor information to guide the surgeon.

2.5 Shape Sensing

Continuum manipulators are employed in a variety of environments, that may be confined, complex in trajectory, or have delicate structures. For such operations, it is crucial that the manipulator can be utilised in a safe, reliable, and accurate manner. The flexible device with should be able to manoeuvre through tortuous paths to a targeted location. Factors such as position, orientation and force of the flexible manipulator must be known during actuation of the robot, so that users can carry out actions successfully. **Shape sensing in the scope of flexible robotics is the system by which the shape or position of the robotic manipulator is known along a number of points through its structure, including the end effector where the tool is located, through the whole trajectory.**

In traditional rigid serial robots, this would be done using encoders and sensors mounted on individual joints, where robot configuration could be solved using straight forward kinematic rigid link analysis. However, with miniature multijointed or continuous flexible robots, other methods must be employed. It is important to have a closed loop feedback shape sensing system, that will allow the required position to be maintained at an updated rate through the trajectory.

One of the applications of continuum robots with the most advanced requirements are for MIS. In MIS, incisions are made on the patient's body, and depending on the procedure, these may number between 3-5 incisions [51]. This is to allow a number of tools into the required anatomical region, including grippers, tissue manipulators, retractors and at times video endoscopes. These incisions are usually small at around 1-1.5 cm wide [52], meaning that tools must be of a small diameter. It is a requirement to have a sensing method that is able to track the device in at least three degrees of freedom, constituting x, y, z spatial coordinates, and also be able to obtain orientation information, including Pitch, Roll and Yaw, totalling six degrees of freedom. Positional information of the tip where, for example, incisions or ablation of tumours may be performed, must fall within 1- 2mm of accuracy, while orientation of the tip must comply with 0.5-2° of accuracy, although these ranges are highly procedure dependent and may not call for such a high degree of accuracy [27]. Another specification outlined in guidelines in that the sensing system must have an update rate of 5-20Hz; this allows the pose of the tracked flexible manipulator to be known in real-time and to avoid any misalignment in dynamic conditions [53]. There is a vast literature on the shape sensing principles for different tools, using a range of sensor modalities. One thing that is apparent is that the shape sensing technique is closely tied to the actuation mechanism and structure of the flexible manipulator and are often merged. The following section highlights different shape sensing methods that have appeared in the literature, and explains how these techniques work, their levels of accuracy, as well as a discussion on their advantages and limitations. In this way a clear research gap can be identified in the area of robotic shape sensing for continuum robots.

2.5.1 Visual based Shape Sensing

Methods for shape sensing can be categorised generally into either contact or non–contact [54]. Non-contact shape sensing systems usually refer to visual systems including medical imaging as well as cameras, while the more current contact shape sensing systems utilise a range of sensor types (optical, inductive, inertial, strain sensors, resistivity sensors, micro-electromechanical sensors) that are integrated directly into the flexible manipulator and are able to respond to physical dynamic scenarios such as compression, extension or respond to changing electromagnetic fields. While non-contact methods are more traditionally utilised, methods for contact shape sensing are an active research field and have the capacity for innovation and improvement upon conventional techniques [2].

With the introduction of MIS in the medical field, early procedures were assisted using visual methods. This included video camera via endoscopes, as well as medical imaging modalities such as X-ray, CT, Fluoroscopy, Ultrasound, and MRI interventions. It provides a direct visual of the target region and is often the most straight forward means to visualise the workspace, as no sensors or extra computational modelling is required. In patients of MIS, Biplane Fluoroscopy is a conventional method to provide visual information, using x-ray arms to reconstruct images in three dimensions, and can provide accurate positioning of surgical devices and anatomical regions using methods such as segmentation [55]. Ultrasound is also one of the main imaging techniques, using an external probe to generate 2D images in real time [56]. In procedures such as arterial ablations, catheters traversing though narrow aortic valves can cause ruptures, which can cause internal bleeding. This is usually due to lack of three-dimensional information. At times, a contrast agent is injected into the patient, which aids in interventional CT or fluoroscopy imaging to assist in the visualisation of anatomical targets as well as the catheter paths. However, this exposes the patient to excess radiation, and some patients had reportedly reacted negatively to the toxicity of contrast agents [57].

For such reasons, intravascular ultrasound was introduced, which was a small ultrasound probe directly attached to the catheter to move inside the arterial region to scope 2D images in real-time. Such intraoperative techniques have been adapted, as it offers an easier alternative that reduces hazardous radiation. Although advantageous, the probe could only scan a limited anatomical range and had reduced image resolution. Moreover, surgical teams have utilised a handheld camera that was controlled by an assistant to the surgeon and manoeuvred upon their instruction. This method was not favourable as this led to shaky images as well as limited visual scope, leading to a more time-consuming procedure as well as risk of errors [58]. This leads on to robotically held scope cameras, which could more accurately be manoeuvred by a surgeon using a handheld controller [53]. While this allows more freedom and eased MIS procedures, the concept of a robotically automated visual system based on modelling was introduced [58]. This framework is based on using endoscopic camera images as information from which the shape of instruments, organs and anatomical settings could be modelled, creating a robotic signal that could automatically pan the camera to a target area based on predicted manoeuvres typically carried out by surgeons, and could also be overridden using a voice instructional interface. While user friendly, cameras still face the issue of becoming obstructed, with limited field of view, as well as the unknown overall shape and position of the flexible manipulator.

2.5.2 Micro-electromechanical and Electromagnetic based Shape Sensing

Contact shape sensing methods have led to the use of sensor components directly with the flexible robotic tools being utilised. Electromagnetic (EM) tracking sensors have been used for shape sensing in continuum robotics. One example is within an MIS application, where an electromagnetic field generator near the patient is used to generate a specific magnetic field, the sensors on the flexible manipulator respond to this field by inducing a signal that can be measured by a tracking system. Depending on the pose of the sensor, this signal varies with spatial location and orientation with regards to the generated field. Work in [59] introduces a three-section wire driven continuum manipulator also for MIS. The work describes the use of EM tracking sensors to detect distal tip position and shape of the sections of the flexible manipulator. Three EM sensors are fixed onto the ends of sections, and a transmitter generates a detected orientation of each from the sensors. Experimental results showed a tip tracking error of 1.7 mm when the reconstructed Bezier curve-based estimations were compared to ground truth values. A difference between Fibre Bragg Gratings (FBGs) and EM sensors is that a single EM sensor can measure six degrees of freedom, meaning that fewer are required as opposed to FBG sensors which require many more to reach the same measurement capabilities, although a number of EM sensors would also be needed to the detect shape of a flexible manipulator.

Work in [60] demonstrated the use of radiofrequency (RF) coils with a biopsy needle. In many MRI guided procedures, the scan plane is adjusted manually, which can be time consuming. Hence, it was proposed to use three RF tracking coils on the biopsy needle, so that position and orientation was known, while an FBG optical fibre sensor was used in conjunction to provide shape information. This was tested with angles between -30° to 30°, where average measured root mean square (RMS) error between the needle profile as seen in the MR images and the profile estimated by the sensors was 4.2 mm for bending cases up to 20 mm tip deflection. This large error was mainly caused by noise from each RF coil meaning that filtering is needed. In a medical setting, further errors may have been caused by surrounding electromagnetic fields from CT or MRI imaging equipment, causing disturbances [61].

Conversely, sets of magnets and hall effect sensors were place on the robot in the work show in [62]. Here, the sensors would measure the varying magnetic flux, depending on the curvature. With modulating the changing resistance values, the shape could be estimated in planar cases.

On the other hand, the use of micro inertial sensors embedded in segments along a joint based snake robot for MIS [5] has been explored. This hyper-redundant structure is made up of multiple two DOF joints. On each link, an accelerometer, which measures tilt, or acceleration in three directions in relation to gravity, and a gyroscope are embedded, which can measure orientation. Measurements from these are used to estimate the orientation between consecutive segments, hence deduct the shape of the entire length of the manipulator. Experiments included embedding in each link a motor and encoder to use as a comparison for estimated results. In this way pitch and yaw could be measured, and while the yaw twist was unaffected by gravity, pitch measurements displayed drift when aligned closer to the gravitational axis. Maximum error values for orientation for one link were 1.29° for yaw, and 3.2° for pitch, when compared to the encoder values. Despite relatively accurate results, this work was preliminary and only carried out on three links and lacked in miniaturisation properties if extended to a full-size snake robot, since the gyroscopic and accelerometric sensing units were relatively large.

Micro-electromechanical and electromagnetic sensors are overall more economically advantageous, and can measure a large range of bending angles, compared to the following optical methods outlined.

2.5.3 Stretch-strain Shape Sensing

Strain sensors of various types have been utilised in soft robotic shape and angle sensing due to their various properties. Film and textile-based sensors are very thin, elastic, and light in weight. Examples of this are included in [63]. The skin-like stretch sensor was composed of carbon nanotube layers within a silicone sheet, placed equidistantly around a silicone manipulator. These types of sensors respond to a change in strain upon bending of the manipulator, as a change in resistance is measured due to the deformation. An elastic knit textile coated in a conductive nanocomposite gel for estimating anatomical joint angles as a wearable sensor was utilised in [13].

Other types of material have also been used for stretch-strain sensors, including conductive foams and liquids, for example in [13][14], which used microchannel films filled with eutectic gallium–indium. Such sensors have higher flexibility, and good conductivity and electrical stability. However, one of the disadvantages of these sensors is the inherent properties of the materials, such as the tendency to exhibit signal non-linearity and noise due to inhomogeneities in the material [64]. It has also been reported that these materials eventually wear out with use, and signal drift can occur within time due to change in elastic properties of the material. Fabrication may also involve complex multi-stage layering. Another point is the assumption of constant curvature in the geometrical modelling of the elastic backbones of the soft robot, which means that more complex curves would not be able to be measured using such stretch sensors [65].

2.5.4 Optical based Shape Sensing

One of the most prominent techniques for continuum robot shape sensing demonstrated in the literature is the use of fibre optic sensing systems (FOSS). Optical methods are often employed for their compatibility with various continuum robotic structures, as well as easy availability of materials. They include components such as optoelectronic sensors, optical fibres, Light Emitting Diodes (LED) as well as Fibre Bragg Gratings (FBG). Some of the reasons this seems to be a prevalent choice for shape sensing in a wide range of applications, is due to their narrow dimensions, flexibility, compatibility with electromagnetic fields, as well as lack of electrical wiring [54]. Some of the applications are found in the mining industry, aerospace industry (for measuring wing deflection), not to mention the medical surgery sector. These techniques are based on the behavioural properties of light, such as changes in wavelength, phase, as well as intensity [66].

For example, a displacement sensor can be formed using a light source and a receiving sensor such as photodiode or phototransistor. As light intensity varies with distance from a reflective surface, light intensity is lost with increasing distance from the source, hence a characteristic behaviour can be observed between the distance from a source and the voltage or current level recorded by the sensor. This modulation of light allows such a displacement sensor to be integrated into different robotic systems in a variety of configurations. Schmitz et al. use such modulation of light intensity using optical fibre cables along a snake-like manipulator [67].

Light is transmitted through these, and reflected at unit sections, where it is then collected using phototransistors at the base. The varying voltage signals induced by the sensor are then used to predict the bending angle of the cables at each reflective section using machine learning models, which is then used to reconstruct the robot's shape.

Al Jaber and Althoefer used a similar approach, using a camera to capture images of fluctuating light from the fibres [68]. However, this work was demonstrated on one segment of the manipulator which required four optical cables. These would accumulate in a full flexible manipulator resulting in a larger space required, and the accumulated number of these optical fibres would increase the overall stiffness and size of the continuum robot. Another point was that the update rate of the sensor was relatively slow.

Another application of light modulation in medical flexible manipulators is shown in the work of Sareh et al. [69], who demonstrate an optical sensing method for position measurement in soft robots using macro bend stretch sensors. This consists of three latticed optical fibres configured equally around a soft robot arm. It is based on the idea that light can be modulated based on the degree of bending in an optical fibre, as power is lost with an increase in bending angle. Macro bend optical sensing can be used to do this, where as long as the degree of bending does not exceed the critical angle, light can be transmitted through the optical fibres and modulates with the angle. A Keyence™ sensor was utilised as both light source and receiver, costing around $250 (US) each [70]. Experiments were carried out to characterise how bending radius changes voltage measured. Based on this model, known voltage can give bending radius information; from this, the length, bending angle and tip position can be calculated to give bending elongation and compression of a soft robotic arm. Experiments showed the maximum error in reconstructed arm length was 18% (7 mm) and calculated maximum bending angle error to be 13 % (14°), while the tool tip position error was up to 9.7 mm. It is assumed that error was large due to model assumption of constant curvature, meaning that there was a difference between the actual and theoretical bending behaviour.

Another reason may have also been due to the pressure/stress at cross over locations of each lattice, leading to light loss from the optical fibres.

Another light modulating technique was the work of Searle et al. [71]. They measured the bending curvature of a flexible manipulator, using three pairs of optical fibres placed into channels along core of manipulator, using magnets to hold the fibres in place, as well as serve as a reflecting surface. Experiments showed the sensing range of -90° to 90°, where measurements were used to reconstruct in three dimensions the bending radius, with errors of 4.1 mm, and the bending angle, with errors up to 4.5°. It is claimed that such error could arise from the fact that constant curvature model does not hold well for large bending angles, or could also have come from design complications, where empty space in channel for which the optical fibres were held meant that there was movement of the fibres that was unaccounted for [71].

Light can also be modulated for sensing systems by varying wavelengths. This is commonly done using Fibre Bragg Grating Sensors (FBG). This utilises lengths of optical fibres to detect orientation by detecting strain or bending, using cross sectional FBGs along the fibres. FBG sensors embedded into these fibres are what allows the measurement of strain or bending, hence is used for shape sensing. The most common method for shape sensing in the literature mentions the use of FBGs with optical fibres or polymer tubes to detect pose and torsion in different robotic tools, such as biopsy needles and flexible manipulators for MIS. Larking et al. [72] demonstrate in their patent the use of FBGs in a robotic system for position sensing. Here, many of these gratings of varying reflective indexes are placed along the fibre at known positions. Light is sent down the optical fibre and reflects at these points, hence generating reflections of varying known wavelengths. This wavelength is related to the amount of strain in the fibre and shifts according to the amount of bending. This data is collected from all the FBGs using an interrogator. This allows the signals from multiple FBGs within each optical fibre to be distinguished through multiplexing. Using this data, the shape of the fibre can be reconstructed by calculating the strain at each point that an FBG is positioned.

A common application of this technique in the medical field was in the use of biopsy needles. Park Et al. [73] devised a biopsy needle with hollow channels to place three narrow optical fibres separated at 120° each with two embedded FBGs. Work included the optimisation of the position of the sensors by running a Monte Carlo simulation (of forces applied along needle) to find locations which produced the least tip position error. By finding the optimised placements, the FBG wavelength shifts were found to be linearly proportional to the FBG location and a function could be mapped. Deflection equations were found using beam theory to integrate curvature equations. After experiments the tip deflection RMS error was measured at 0.38 mm (for deflections up to 15 mm). However, it did not take into account the effect other loading would have on bending profile, and sampling rate was at 4Hz, which was due to the sampling rate of the interrogator used. The authors mention that error could have arisen from drift in nominal centre wavelength meaning that it would have to be accounted for with calibration.

A similar configuration was demonstrated by Henken et al. [74] [75], where three glass fibres were embedded into a trocar needle each with a pair of FBGs. Experiments were done where the needles deflect when inserted into different tissues. For tip deflections of up to 12.5 mm, the tip position was estimated with a mean accuracy of 0.89 mm, however adding a second curve deflection led to an increase in error of up to 1.32 mm, signifying that more complex curvatures can be a source of increased error. This leads to the consideration of the application for the robotic manipulator and complexity of the paths and workspace necessitated by the task, with reference to the paths to targeted location, as well as manoeuvres of the tool required.

Roesthuis et al. [76] applied FBGs to the backbone of a tendon actuated robot manipulator. Using kinematic modelling, the shape was reconstructed in three dimensions, using estimations of the tendon cable length. The manipulator was controlled using a closed loop feedback PID controller to carry out experiments. During path tracking experiments, large errors occurred when there was a sharp curve or change in direction. The mean errors depended on the path shape: 0.67 mm (circle), 1.17 mm (square), which were planar cases, while for a 3D helix trajectory, the error was (0.87 mm). Some error was supposedly caused by improper positioning of FBGs during manufacturing.

The model by which the shape is reconstructed is also to be taken into consideration, where strain values are put into this model to solve for shape of the device. This is to ensure that error is minimised, and performance is accurate and efficient. The work of Roesthuis et al. [77] shows a three-dimensional needle shape reconstruction method that uses an array of FBGs. Unlike Henken et al. [74] and Park et al. [73], they use three fibres, with four FBGs in each, rather than two. The work demonstrated the use of two models used for reconstructing the shape, one based on kinematics – using constant curvature at sections along needle, while the other was mechanics based - where the needle is modelled as a beam with a distributed load profile. Experiments consisted of testing on a phantom, using a CCD camera to track tip location. Results showed that using the kinematic model led to deflection errors of 3.77 mm when compared to the camera, while using the mechanics-based model gave better results, with deflection errors of 2.2 mm. Errors were higher when deflection was larger or out of plane, and it was mentioned that a larger number of FBGs would attribute to better performance. Kim et al. [78] consider the placement of sensors for fast and accurate sensing, including the number and spacing, alongside varying reconstruction models. Concentric tube robots for MIS were used, and FBGs embedded in three optical fibres were mounted equilaterally along the innermost tube. Two main reconstruction models were considered, these were: a Piecewise Constant Curvature model and a Basis function model (finding function of the curve). An optimisation algorithm was also employed to find the optimised positioning of the FBGs along the optical fibres, and it was found to have reduced the error compared to uniformly distributed FBGs. The number of FBGs was similarly found, where results showed that although more FBGs within the optical fibre would greatly reduce the average tip position error, this number peaked at around four, after which a larger number of FBGs embedded in the optical fibres would lead to a rise in average error. The basis function model, specifically the section based polynomial regression method was the best reconstruction model, with average tip tracking error at 0.2 mm, while piecewise curvature was the worst, with average tip position error at 6.2 mm.

A similar study was done in [79], exploring different reconstruction methods for shape sensing from sensors such as the kinematic models, basis functions, or statistical models. FBG based sensing systems have also been employed in catheters for aortic valve replacement procedures [57]. Here optical fibres consisting of the FBGs were threaded into the central channel of the catheter, and in a similar way was used to get the catheter shape, however worked alongside electromagnetic sensors to get position information. Here, each optical fibre held eight FBGs, using the Deminsys interrogator that was able to sample at a rate of 20kHz. The shape was reconstructed using Frenet-Serrat formulas to calculate curvature integrals and overlayed in a virtual model of the aortic valve.

Another procedure that FBG based shape sensing had been applied to is Total Hip Replacement, as described in the work of Liu et al. [80][81]. The flexible manipulator body is made of a soft compliant material with slits that allow it to extend and compress, with a hollow lumen. Two FBG optical fibres are fixed in two channels on either side of the body of the manipulator, giving it a larger range of flexibility, that could reach a bending radius of up to 6 mm. This makes it suitable for use for hip replacement to treat osteolysis. Some remarks included that during surgery there may be a temperature gradient between the sections of FBG inside the body compared to that further out, however results showed distal tip error of 0.48 ± 0.3 mm.

While these methods reconstructed curves in both planar 2D cases as well as 3D cases, in both orientations including pitch and roll, they do not take into account torsion of such optical fibres, also referred to as the twist, or yaw orientation. Moore et al. [82] used multicore FBG fibres, using mathematical models including Kirchhoff assumptions and Frenet-Serret equations to mathematically define the bending and torsion of the fibre in three dimensions. The strain measurements were fed into the mathematical solutions to get results and were compared to predefined curves with known coordinates. Maximum error was found to be 7.2%

and is thought have risen due to separation between fibre and sleeve coating, meaning that the sleeve induced its own twists, which did not align with mathematical assumptions (e.g. uniform rod etc).

Xu et al. [21] implement a pre-curved nitinol tube (2 mm diameter) with helically engraved grooves to allow placement of FBG sensors for a continuum robot. This was done to find strain, torsion, as well as force. Using a Micron Optics Interrogator sampling at 100 Hz, the sensor can estimate shape with RMS error of 2.62 mm. The calculation of torsion is not often done in the literature and at times measures are taken to remove this degree of freedom, for example the work of Ryu et al. [16], who explored the use of low modulus material tubes (more compliant), rather that optical fibres so that less strain is experienced. However, this also meant more compliance in torsion. To avoid this, they used a material that is flexible in bending but stiff in the twist direction, by using a flexible polymer infused with a latticed metal wire braid. An interrogator (micron optics) was used to measure the FBG strain values at 1 kHz, and shape was reconstructed with tip position error 0.84 mm ±0.62 mm, and orientation error 1.21° ± 0.91°. This material tube is inserted into the central backbone channel in a robotic manipulator, with three tubes glued 120° apart.

To summarise, optical methods employed in shape sensing is vast and a wide field of research. The most common methods are the use of FBGs with optical fibres, deployed in a range of flexible manipulators. Depending on the application, different configurations are used, depending on the extent of measurement in terms of degrees of freedom of the sensing system required. Fibre Bragg gratings show promising results and often show a high degree of accuracy in terms of tip tracking and falls within the 1 mm guideline. Such FBGs are incredibly small, within the order of micro-meters, meaning that they can fit into small optical fibres, which are flexible. These methods also do not suffer from line-of-sight issues as in visual or image-based techniques for position tracking.

Despite this, one drawback of the use of Fibre Bragg gratings is the costs that are involved. Engraving of the gratings is complex and time-consuming manufacturing procedure, and placing these within the optical fibre is difficult and can lead to uncertainty in the intended positioning of the FBGs along the fibres. As described previously, errors in shape sensing can arise due to this. Along with the cost of production of the FBGs, the use of multiple FBGs for the sake of increasing accuracy means that an interrogator is required to measure all the signals. Such apparatus can cost above £10k, with prices increasing with the number of channels and sampling speeds (HMBshop). Flexible manipulators are often long, meaning that it is likely that a higher number of FBGs would be required, leading to a trade-off between accuracy and incredibly high costs. Fibre Bragg optical fibres are sensitive to temperature drift, and as well as a shift in the central wavelengths over time, which must be accounted for by calibration [83][84]. Another factor to consider is the strain transfer properties of FBG optical fibres. Based on experiments reported through the literature, FBG sensors do not perform well in low stiffness conditions [84], and errors rise with increased deflection radii. In the use of optical fibres with light intensity modulation, where the cost of optical cable and optical components such as photodiodes/transistor were significantly lower, an issue that arose was the fibre's sensitivity to external pressure, leading to loss of light. With such a sensing principle, multiple optical fibres will likely be required, which leads to bulkiness and stiffness if integrated into the backbones of flexible manipulators.

Finally, an optical method that greatly differs from those shown previously is demonstrated in Koh et al [85], as it utilises an optoelectronic sensor. It proposes a tendon actuated robotic manipulator, with circular disk sections embedded with three optoelectronic sensors. These sensors are able to emit an infrared beam of light that is reflected off the consecutive surface and received by the phototransistor that is integrated within the same sensing unit. This sensing principle depends on the modulation of light as previously described, varying the recorded voltage with varying reflective distances between a surface and the sensing units. This configuration allows measurement in real-time of 5 DOF including position (x, y, z), pitch, and roll, while torsion is minimised using springs between the sections of the manipulator. Experimental results show the use of an inertial measurement unit (IMU) sensor to compare measurements to the estimated orientations using a linear regression modelling method. For a three-plate configuration, the maximum percentage difference errors for pitch were 21% and 33% for roll compared to true values. This claims to be due to the regression method chosen, and future work should investigate alternatives such as non-linear regression models for shape estimation. The work presented in this paper forms the basis of this project, and the proposal is outlined in the next chapter.

2.5.5 Shape Sensing overview

Table 2.1 lists all the shape sensing techniques mentioned in section 2.5, providing an overview of techniques used, applications, advantages and limitations of the shape sensing technique, as well as sensing performance. The table also shows some of the error values of the shape sensing performance which can be used for comparison with the forthcoming results in this thesis.

2.5.6 Research gap in continuum robot shape sensing

Considering the variety of different shape sensing techniques discussed in section 2.5, areas for which advancements can be made are identified when considering some of the limitations of these techniques. In proposing to develop a new shape sensing technique, the system must be scalable to be integrated in for example MIS based continuum robots. It would have to allow flexibility, avoiding bulky or unwieldly materials that would limit bending and affect the stiffness of the manipulator. Following this, the shape sensing technique should ensure safety when integrated into the manipulator, in terms of electrical and biocompatibility properties. The system should enable real-time shape sensing, with update rates within the range of at least around 20Hz. It should be low cost, to allow a more accessibility within the industry if considering commercialisation. The system should be able to track shape, with tip position with a 1-2 mm degree of accuracy, and orientation 0.5-2° [27][52][29]. The shape sensing system performance should not be influenced by material properties, in the way that strain or stretch based shape sensors do, to avoid some of the issues mentioned, such as poorer performance at high curvatures, material degradation or material inhomogeneity. This ensured that calibration is robust and maintained. The shape sensing system should also not be influenced by external signals or fields or suffer from interference from external sources. From this, the proposal for an optoelectronic shape sensing technique is justified, as a method with promising potential to meet these requirements, as an advancement to shape sensing for continuum robots. Further justification for why this sensor type was selected is discussed below.

2.6 Sensor Selection

Sensors are electrical devices that can detect changes in the environment by measuring physical properties. This includes properties such as displacement, voltage, electromagnetic fields, temperature, pressure, and many more. This means that not all sensors could be employed in the proposed robotic structure for shape sensing, as a sensor that would be able to detect displacement or respond to motion would be suitable. By looking through other electronic sensors (that have not appeared in any shape sensing technique mentioned in 2.5) that would be able to measure range or deflection within a bending robotic structure; while also avoiding the problems identified in the previous section with the described shape sensing principles, a suitable sensor can be employed for a new shape sensing method for this project. These sensor types are displayed in Table 2.2 below.

While many of these sensors provide a great means of measuring position and orientation, with excellent accuracy, resolution, and sensitivity, the application must be considered for which these are to be implemented in, as well as the environment for which they are to be used. As previously outlined, flexible robotic manipulators must adhere to certain specifications. These included smaller dimensions so that the flexible tool will be able to fit through confined environments and will maintain dexterity and flexibility for complex procedures. This means that the shape sensing technique must support this. Capacitive or inductive proximity sensors require physically large dimensions. It would be difficult to implement multiple capacitive sensors into a robotic manipulator structure to measure deflections at multiple points along the structure. With the addition of long signal cables channelling along the structure, this would introduce increased stiffness and reduced flexibility. For this reason, a shift into the smaller sensors would be practical.

Environments such as in factories, or in surgical rooms commonly use several types of electrical equipment, including biomonitoring and imaging systems such as CT or MRI. These emit radiofrequencies and electromagnetic fields, which may alter the performance of sensors which inherently use these modalities. For example, external magnetic fields from an MRI scanner may distort the signal in magnetic hall effect sensors. This would lead to increased errors in estimation position tracking along a robot.

Resistive based sensors offer a multitude of methods for implementing shape sensing, as different conductive materials have been developed that are flexible and thin. For example, conductive yarn has been implemented in shape sensing for soft robotics, where the bending and extension was measured [86]. However, one consideration is that a material with good conductance often reduces stretch factor, but is necessary to reduce power consumption, which is important for device safety, although the extent to which this significant is dependent on the structure of the sensing configuration and robotic manipulator [87]. Strain based sensing modalities are not ideal for use in stiffness varying actuated robots, such as pneumatically actuated continuum robots, as this variable stiffness affects the properties of the sensor [88]. Resistivity sensors are also affected by temperature.

This leads onto the consideration of another type of sensor, that has miniature qualities, while also unaffected by external field conditions, temperature, or material properties. This is photoelectronic based proximity sensors. Photoelectric proximity sensors can generally be categorised into either (1) through Beam sensors, (2) Retro reflective sensors, or (3) Diffuse reflection sensor [89]. They all consist of a light source, and a receiver, and can detect proximity or presence of an object. Through beam sensors emit light from a source. This path of light travels directly to the receiver. An object crossing this path will interrupt the stream of light, which causes a change in signal output. Retro-reflective sensors rely on continuous reflection of light on a surface, where the source and receiver of light are coupled together. Diffuse sensors have the source and receiver housed together, where within a specified range, an object will diffusely reflect emitted light back to the sensor, triggering an output signal. Of these, a retroreflective photoelectric proximity sensor has been selected. This is most suited to different structures of continuum robotics and allow more flexibility in terms of positioning and configuration of sensing units. Infrared light is used as source, to eliminate the chance of noisy signals due to ambient light. The lower energy waves also reduce heating and power consumption. There are many available sensors of this type on the market, with variety in size, sensing capability and detector type. A phototransistor detector is more sensitive than photodiode since it is a bipolar transistor and also has high level gain; although photodiodes have a higher detection range, phototransistors have less noise than photodiode [90].

Table 2.2 shows such sensors than can be found online. For the current stage of the project, the low cost QRE113 sensor will be used, as this has the dimensional qualities, with good optimal sensing range (0-5 mm) that is not too limited but not unnecessarily large where signal can become noisy. Once proof of concept is completed, this can be substituted accordingly to a smaller or alternate range as required, for example the NJL5901R-2.

TABLE 2.1: OVERVIEW OF DIFFERENT SHAPE SENSING METHODS USED FOR CONTINUUM ROBOTS

Ref	Continuum robot type	Shape sensing technique	Performance	Advantages	Limitations
[1]	Tendon actuated robot, 3 segment	Electromagnetic sensors are attached to ends of each segment to measure pitch and roll orientations. 360mm robot length	Distal tip error: 1.77 mm	EM method does not have the line-of-sight problem, fewer sensors needed compared to FBG	Signal noise
[2]	Planar, pneumatically actuated soft robot	Permanent magnets and Hall Effect sensor is attached to the robot, to measure flux changes during motion. ~ 70 mm robot length	Shape error: 1.308 ±0.15 mm	Small dimensions, accessibility, simple manufacturing, and lack of external processing circuitry requirements.	Magnetic sensor displayed noisy signal
[3]	Planar snake-robot (one link)	Micro-inertial sensors (accelerometers) are placed along the robotic structure, to measure orientation two directions	Tip orientation errors: 1.29 °(yaw), 3.2 ° (pitch).	Relatively miniature sensor components. Large angle measurement range.	Signal drift can occur, as well as disturbance by external signals. Difficulty integrating in soft or flexible robotic structures.
[4]	Planar snake-like robot (one link)	Optical fibres placed along the robotic structure used to measure joint angle at multiple points, using modulation of light intensity against a reflector at each joint. Intensity is measure by a phototransistor.	Tip orientation absolute mean error of 0.71°	Can be deployed in a variety of formats using small, low-cost components	Stiffness can build in longer lengths of the robotic structure
[5]	Tendon actuated (two segments)	Three optical fibres along with magnets are integrated along the structure. The magnets serve as reflectors. 60 mm robot length	Bending radius error 4.1 mm Bending angle error: 4.5	Miniature fibre size. The sensor is low cost and is temperature independent as its intensity based.	Assumption of the constant curvature may not well hold for large bending angle. Gap in fibre channels may cause error in shape estimation.
[6][7]	Two-axis tendon actuated	12 FBG attached to nitinol tube and integrated into tendon actuated robot. 160 mm	Tip position errors for various shape trajectories - Circle: 0.67 mm Square: 1.17 mm Helix: 0.87 mm	Highly flexible, versatile and accurate	Does not perform well at high curvatures, high cost for manufacturing and peripheral equipment.
[8][9]	Tendon actuated planar robot	Pair of optical fibres with multiple FBG nodes are channelled through a tendon actuated robot. 35 mm length.	Distal tip error: 0.48 ± 0.3 mm	One of the more accurate shape sensing methods. High sampling rate, narrow dimensions, versatility.	Clearance between the optical fibres and its lumen may cause curvature detection error. Multiple FBG nodes are required for accuracy but could affect stiffness. Sensors may break under large deflections
[10]	Planar robot	FBG sensors are placed around helical groove in nitinol tubes, for measurement of curvature, torsion and force. Three of these tubes are fused onto soft robot. 90 mm length	RMS shape error: 2.62 mm	This technique allows accounting for torque motion, which improves curvature estimation.	There were many challenges in creating the helical groove and fusing the FBGs. Signal distortion is observed at higher loads (40g)
[11]	Two-axis continuum robot	Shape sensing is based on a wire braided polymer tube with mounted optical fibres, that have FBGs attached. Three of the optical fibres are placed equidistantly. It uses low compliance materials. 80 mm robot length.	Tip tracking error: 0.84 ± 0.62 mm Orientation error: 1.21 ± 0.91°	This technique uses latticed metal wire braid that is stiff in the twist direction to avoid torsion. Less compliant materials allows larger bending radii to be achieved	At higher strain levels, the strain transfer ration may decrease, leading to inaccurate sensing, as material properties within the elastic limit are not maintained.
[12]	Two -axis tendon actuated robot	Optoelectronic intensity-based shape sensing. Three reflective sensors are placed into disks of tendon actuated robot. Levels of reflection during motion modulate the signal, for estimation of orientation. 100 mm robot length	Tip orientation maximum error: 18° (33%) in roll, and 9.7 °(21.2%) in pitch.	This technique offers a non-contact shape sensing method, that also free from effect on material properties. Miniature and low cost	The calibration technique is not fully developed; therefore, orientation estimation accuracy is reduced. Non-linear regression was not considered despite non-linear sensor response of the reflective optical sensors.
[13]	Soft Robot	Skin-like stretch sensor composed of carbon nanotube layers within a silicone sheet, placed equidistantly around a soft silicone robotic manipulator. 80 mm robot length	Tip position error for small deformations: 12.1 mm (3 sensors) to 8 mm (9 sensors). For deformation larger than 40%: tip position error was 23 mm, and 8.9 mm, respectively.	Highly flexible, thin dimensions and adaptable to many applications.	Signal non-linearity and noise due to inhomogeneities in the material. Assumption of constant curvature in the geometrical modelling means that more complex curves would not be able to be measured using such stretch sensors

TABLE 2.2: REVIEW OF COMMERCIALLY AVAILABLE SENSOR TYPES

Sensor Type	Description
Inductive Proximity Sensor: 	These types of sensors use an oscillator to generates magnetic field. When magnetic material enters this field or is in close proximity, a current is induced which depends on proximity to metal object. They usually consist of the sensing tip, with a long signal cable, with smaller models sizing at around 6mm, and can detect surfaces at an average range between <1mm to 60mm. The measured signal is highly sensitive to the material in close range and can be affected by external electromagnetic fields [130].
Capacitive Proximity Sensors: 	These sensors consist of two capacitive plates. Depending on the material of the object in range, the capacitance between two plates increases as it enters the electromagnetic field. This induced a change in potential difference, and a varying voltage signal is outputted. Such sensors can cost around £50, with sensing resolution up to 0.05mm, and dimensional diameter of ~12mm [131].
Ultrasonic Proximity sensors: 	These work by using generated emitted and received reflected ultrasonic pulses using a transducer at the tip. Models report sensing resolution of 0.069mm, and typical dimensions can include [132].
Hall Effect Sensors: 	Hall effect sensors are activated in the presence of a magnetic field, where depending on the strength of the fields the potential difference generated by two plates varies. The cost of one using is around £3. Permanent magnet would be intrinsic to using this as a shape sensor, and distance away from the magnet would indicate proximity due to voltage change [133].
Inertial Sensors: 	Gyroscopes can be used to measure rotation in up to three directions, while accelerometers can measure acceleration with tilt in up to three rotational directions, using a piezoelectric or capacitive plate effect. There are also inertial measurement units (IMU) that combine magnetometers, gyroscopes, and accelerometer to provide acceleration and three-dimensional rotation information. This can give orientation as well as position. Can be sensitive to noise and movements such as cable movement, leading to signal distortion [134].
Encoders 	Linear and rotary encoders are sensors that are able to detect position and velocity. They are often found in DC motors and provide positional feedback of the motor. Optical based rotary absolute encoders consist of a photo source and detector, with digitally encoded rotating unit, and can also work using magnetic effects. Encoders offer excellent accuracy but can also be susceptible to radio interference [135].
Resistive Sensors 	These work on the principle of the resistive properties of a conductor that change with applied strain. Increased strain on such a sensor would change the resistance of the material, and the output signal would vary. Such thin conductive materials can be woven into fabric, to make flexible textile sensors, and is implemented into soft robotics and wearable technology [136].

TABLE 2.3: TYPES OF OPTICAL REFLECTIVE SENSORS, COMPARING HOW SIZE AND DETECTOR TYPE AFFECT THE OPTIMAL SENSING RANGE.

Sensor	 *TAOS*	 *Avago Surface mount*	 *Vishay*	 *QRE1113*	 *Vishay*
Size (mm)	*4x3mm*	*7x30*	*2x2.5*	*4x3*	*10x6*
Detector	*Photodiode*	*Photodiode*	*Phototransistor*	*Phototransistor*	*Phototransistor*
Range (mm)	*<100*	*0-60*	*0-2.25*	*0-5*	*0-15*

Image references: [125][126][127][129][128]

2.7 Conclusion

This chapter introduced the background of continuum robots and the role of shape sensing. A literature review study was carried out to explore the different types of shape sensors, identifying how they work, any advantages as well as limitations. This aided us in understanding where advancements could be made in the proposal of a new shape sensor. Optoelectronic shape sensing target some of the limitations exhibited in common shape sensing techniques, and this is the sensor type that will be researched in this thesis in subsequent chapters. In the following chapter, an in-depth study of optoelectronic sensors, more specifically, photo reflective sensors will be carried out, to understand the characteristics of this sensor type and how to use it to its full potential within a shape sensing system for continuum robot applications.

CHAPTER 3: NOVEL OPTOELECTRONIC SENSOR CHARACTERISATION STUDY

3.1 Introduction

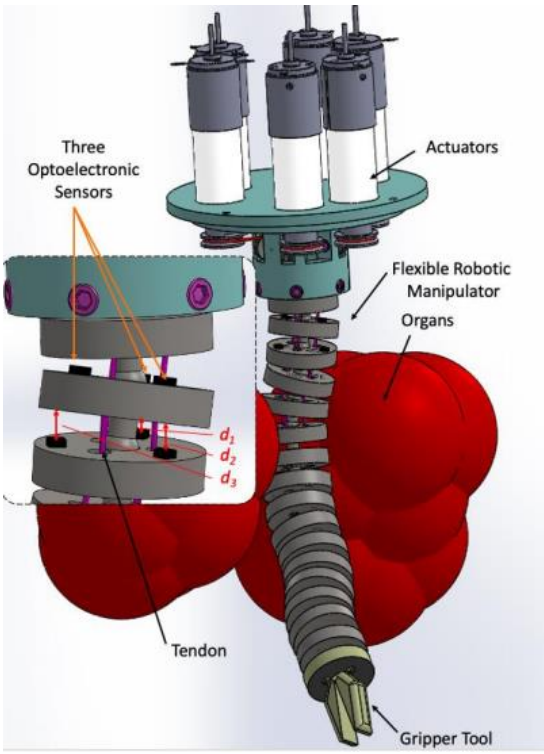

Figure 3.1: Design concept for optoelectronic sensing principle [85], integrated into a tendon actuated robot; three optoelectronic sensors used to detect light intensity reflected from tilted disks, output voltages will depend on degree of amount of light reflected, which depends on displacements (d1, d2, d3). Voltage data is used to estimate orientation of each upper plate and used to reconstruct shape of robotic manipulator.

Before developing the designs for an optoelectronic shape sensing modality to be integrated into a robotic flexible manipulator, some preliminary study needs to be done to understand the workings of optoelectronic sensors, and how these can be utilised to the best of their potential. Chapter 3 will lay out the study of optoelectronic sensor characteristics, electrical properties, and theoretical mathematical modelling of the sensor behaviour. The relationship between the proposed optoelectronic sensor and parameters such as the proximity to a reflector, the angle of the reflector, the surface texture and colour of the reflector, as well as the electrical properties of the optoelectronic sensor component will be experimentally evaluated. Following this, a mathematical model is derived, describing the behaviour of the optoelectronic sensor and the mentioned parameter variables, and is based on a gaussian light intensity model. The model is validated against experimentally derived data.

3.2 Methodology

This section describes the methodology of studying the optoelectronic sensor. For the first part of this project, we must look at the fundamental nature of the optics that we will be utilising as the sensing mechanism. This should include a study of how the optoelectronic sensor responds to varying light intensities when parameters are changed.

In regard to the shape sensing proposal in Figure 3.1, this is based on the work of [85], in which three optoelectronic sensors are embedded into each disk of a tendon actuated robot. As the robot segment bends, the proximity between the optoelectronic sensors and the consecutive upper disk varies, which induced varying voltage signals in the sensor components. From the voltage signals, the bending of the disk in two orientations can be estimated, and further the orientation of the full segment. From this concept, we can presume that the parameters that need to be considered for development of further robotic manipulators integrating optoelectronic shape sensing include **(1)** the power of the transmitted light of the optoelectronic sensor, **(2)** the type of reflective surface as well as colour, **(3)** the linear distance between the optoelectronic sensor and a reflective surface (proximity), **(4)** the angle of the reflective surface relative to the optoelectronic sensor and **(5)** the position of the optoelectronic sensors relative to the central rotational axis of the reflector. In doing this, an optimised configuration can be found for the design and placement of the sensors within the robotic manipulator.

As described in the previous section, the optoelectronic sensor unit is made up of an LED plus a phototransistor (PT) that collects reflected light. The initial intensity of the sensor, which is the power emitted by the LED can be controlled by adjusting the resistors connected to the LED and PT. Higher resistance values would limit the LED current, meaning that a lower initial light intensity would be emitted. This is also true for the PT, where the collector current induced by the reflected light can be limited by a resistor. Thus, it is important to investigate the balance between having a low powered sensing system by using higher value resistors, which would contribute to user safety, and finding a sensitive range suitable for the dimensions of the sensor configuration as well as avoiding saturation of the signal. To do this, the sensor was experimentally investigated using a range of resistive components to characterise the behaviour, which showed how changing values of LED resistance and PT resistance affected the characteristic curve of the voltage measured over a linear displacement away from the reflective surface. A mirror or white surface will have a higher reflectance rate than a darker surface. This was taken into account by repeating experiments on both a white and black coloured surface, to investigate the effects this had on characteristic curves. Once a suitable resistor configuration was identified from the results, the effect of the placement of the sensor at a distance from the rotational axis of the surface, and angular rotation of the surface was investigated.

Initially, a mathematical model was constructed to describe the propagation of light from a light source, that reflects from an angled mirrored surface and is received by an optical sensor. The light leaving the source is assumed to hold a gaussian intensity distribution profile. By modelling the geometrical set up of the sensing modality, the reflected flux/power that is collected by the receiving section of the optoelectronic sensor was theoretically calculated, as a function of the parameters - surface angle, axial distance, and lateral distance. This flux was converted to a theoretical output voltage through a conversion factor coefficient based on experimental data. Hence completing the theoretical model. This was then validated by using the model to simulate characteristic responses based on different parameters and compared to real experimental data. This model can help us understand how these parameters alter the sensor output and how to reach optimal conditions in terms of power consumption and sensor sensitivity. It can be applied to any similar sensor and parameters can be simulated, which is valuable in any future design plan, for example plans to miniaturise dimensions, or for where an iterative design process is likely to be used.

3.3 Working Principle of the Optoelectronic Sensor

The sensor chosen to carry out the shape sensing for a robotic manipulator was the QRE113 Miniature Reflective Object Sensor (Onsemi, Phoenix, AZ, US) (3.6 × 2.9 × 1.7 mm) (Figure. 3.2). This coupled optoelectronic sensor consists of an infrared light emitting diode with a phototransistor voltage output. The diode emits light at an infrared range of 940 nm. As this light is reflected off a surface, light collected by the phototransistor causes a current to flow between the collector and emitter of the semiconductor within the phototransistor. Depending on the distance of the mirror surface from this sensor, the intensity of light collected by the phototransistor will vary. The further the mirrored surface, the more loss of intensity in the path of light to the collector, meaning that a lower current is induced. This behaviour is illustrated in the Figure 3.2 - at small distances away from the sensor, there is little reflection hence the low collector current. From the peak, at around 0.8 mm, the current decreases exponentially with increasing distance between the mirror and sensor. This modulation of light intensity is what will allow essentially a displacement sensor to be used as the basic unit within the proposed sensing principle. The tilting and translation of a reflective sensor away or towards the sensor will modulate the light intensity, resulting in a varying voltage output signal. They are connected as shown in Figure 3.2: with pin 2, the cathode connected to ground, pin 1, the anode connected to a 5V supply with a current limiting resistor, the emitter connected to ground, while the output collector (pin 3) is wired to a 5V supply, with a current limiting resistor.

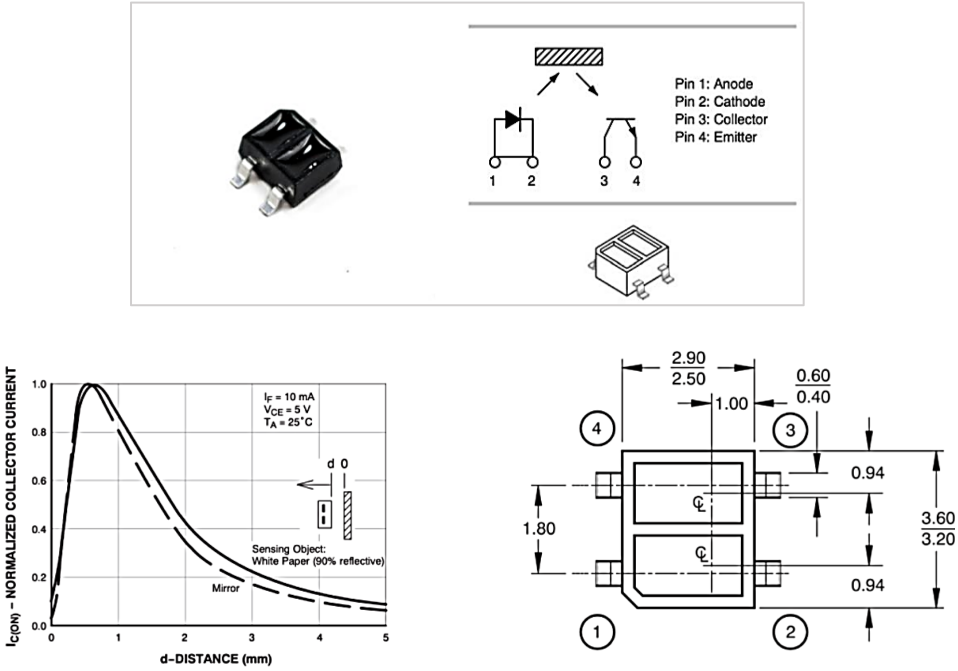

Figure 3.2: (Top) Optoelectronic Sensor - QRE113 showing LED and PT circuit. (Left) The graph shows the normalised collector current against linear distance to a reflector, and dimensions of the sensor are shown (Right).

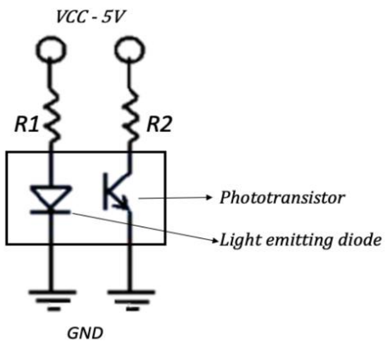

Figure 3.3: Optoelectronic sensor resistance circuit connection. R_1 is LED resistor, and R_2 is the Phototransistor resistance.

3.4 Experimental characterisation of optoelectronic sensors

One of the fundamental experiments to begin this project was to perform basic tests to characterise the behaviour of the chosen optoelectronic sensor with a reflective surface, in terms of how light distribution changes the output signal with varying distances between the planar reflective surface and the phototransistor of the sensor. It is also important to study the effect that resistor values had on this characteristic light distribution. The sensor circuit connection (Figure 3.4) shows two resistor values that must be chosen: these are the LED resistance, labelled R_1, and the phototransistor resistance, labelled R_2. For instance, increasing the value of R_1, would decrease the LED current, hence reducing the intensity of light emitted from the LED portion of the sensor. This light would travel, reflect off a surface, and be detected by the phototransistor portion of the sensor. This would result in a lower collector current and would relate to the voltage signal in inversely. In another instance, decreasing the phototransistor resistance R_2, will have the effect of increasing the current induced by the received reflected light. This would result in a lower output voltage. The aim is to find the balance between the two values, in order to have a large signal range and good sensitivity, whilst also keeping the current levels low in order to factor in safety with regards to overall power consumption in the final device. These tests will also help to validate the theoretical model to be demonstrated in the following section.

The set up for these experiments is shown in Figure 3.5a. It shows a linear guide that is driven by a DC motor (Maxon, Sachseln, Switzerland), connected to a motor driver. This driver is connected to a 24V power supply, and the motor drives the platform on the guide to move along a singular axis. Onto this platform is mounted a planar surface that performs as the reflective plane upon which the sensors' emitted light can reflect. These components were design on SolidWorks and 3D printed using white PLA filament. At the fixed end of the linear guide, is where the sensor is mounted upon a universal circuit board, parallel to the reflective surface component, and perpendicular to the direction of proposed linear motion. The optoelectronic sensor is connected to a National Instrument ADC (NI USB-6008, Texas, US), which sampled the sensor data and transferred to the PC via USB. Motion was controlled by a software program in Visual Studios. The software was used to read and write motor position, hence controlling the distance 'd' between the reflective surface mounted on the platform and the fixed sensor set up at the end of the linear guide. This distance data was recorded by the software while simultaneously recording sensor voltage data and saved onto an excel sheet. The user interface of the software is shown in the Figure 3.5c.

Subsequently, the data that was collected is described as follows: R_1 was set to the low recommended operational value of 150 Ω, to allow for maximal light emission for, for a higher level of reflectance from the surface. R_2 values are varied at resistor values of 1 kΩ – 100 kΩ. For each R_2 value, sensor signal data was collected over a travelled distance of 0 – 15 mm from the surface of the sensor to the perpendicular reflector. Once all this data is collected, the converse is repeated on a range of R_2 values, with setting the value of R_2, and testing a range of R_1 accordingly. This is repeated for white PLA reflecting surface, as well as a black reflecting surface. The results for this are shown in Figures 3.5, 3.6 and 3.7.

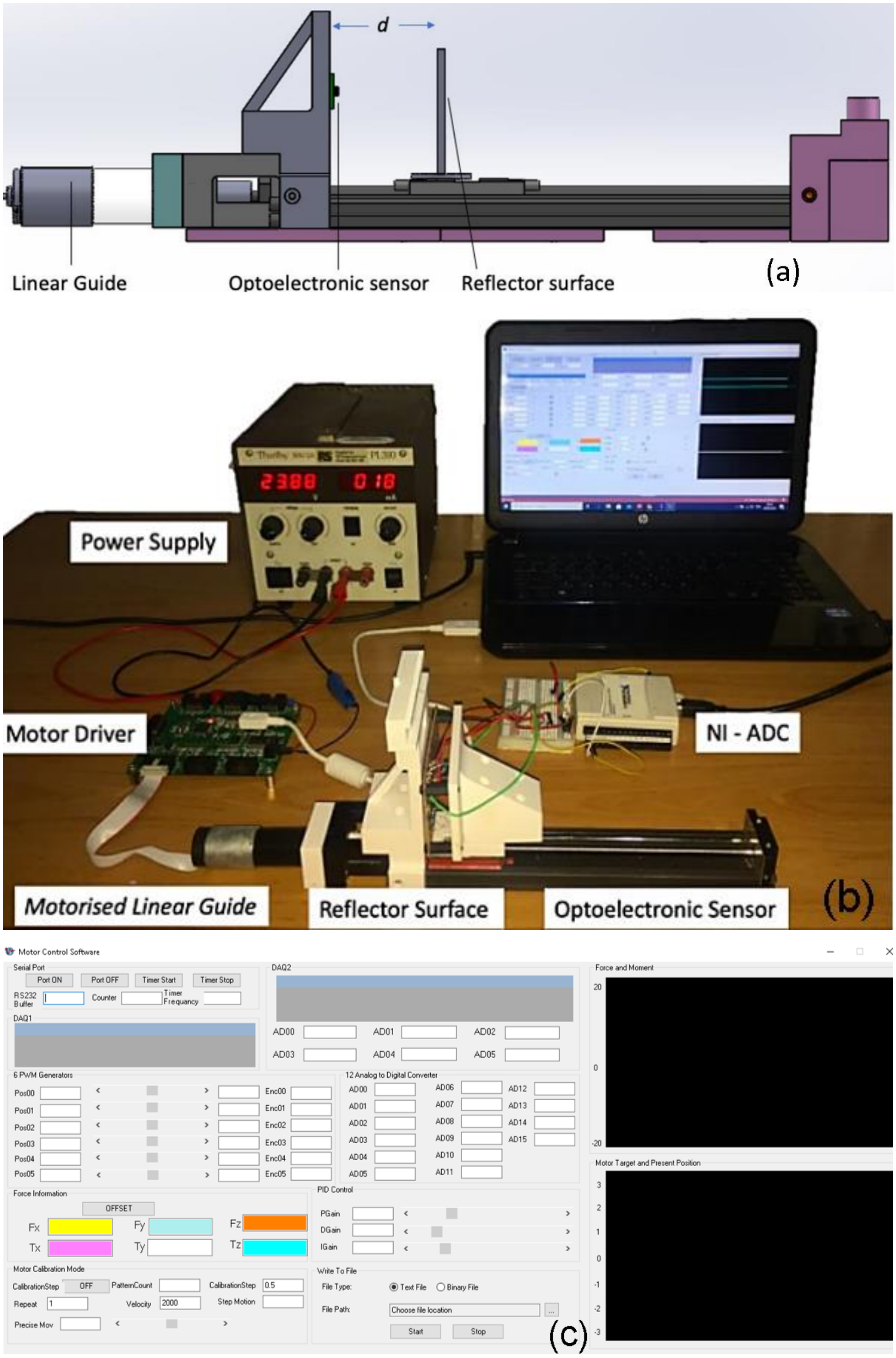

Figure 3.4: (a) CAD model of the experiment rig, using a linear guide. A single optoelectronic sensor is mounted to the fixed end of the guide, while the reflective surface is mounted onto the moving platform. (b) Actual experiment set up: linear motor position is controlled by PC via motor driver. LED and PT resistor values (R_1 and R_2) are varied on circuit board. Guide position and sensor voltage data are recorded simultaneously. (c) software interface for recording multiple sets of data.

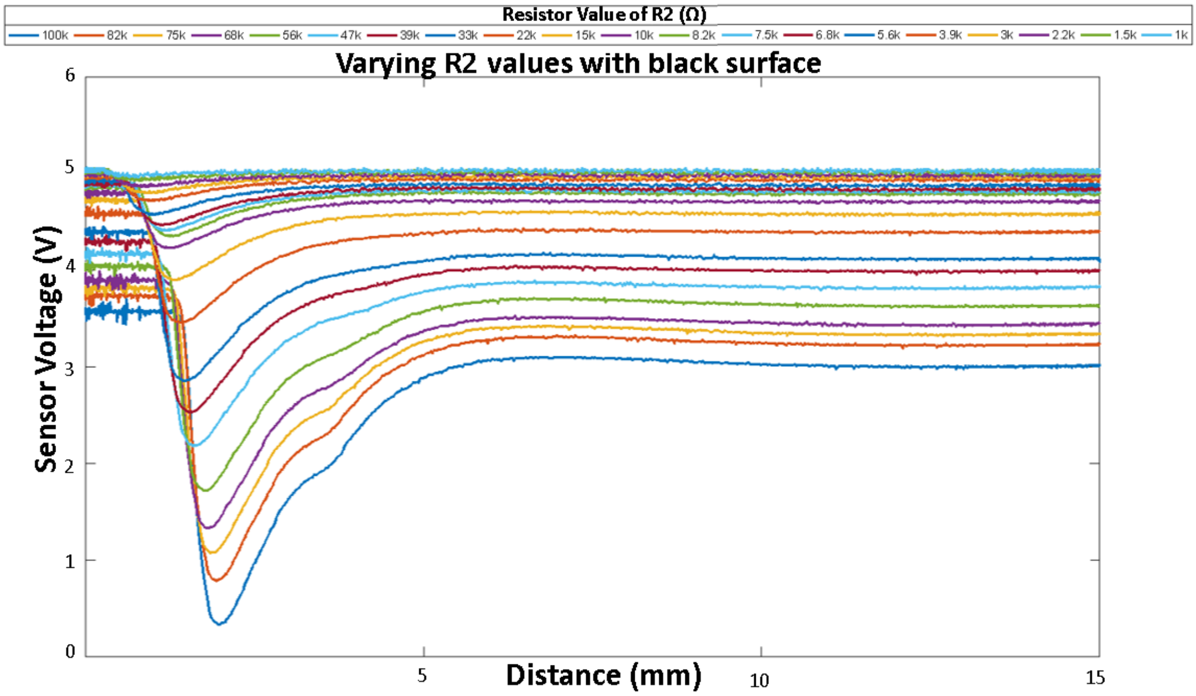

Figure 3.5: Optoelectronic sensor signal over increasing linear proximity to a black surface reflector. The value of the collector current resistance (phototransistor) R2 is varied between 1k-100k Ohms, while R1 is set to 150Ω.

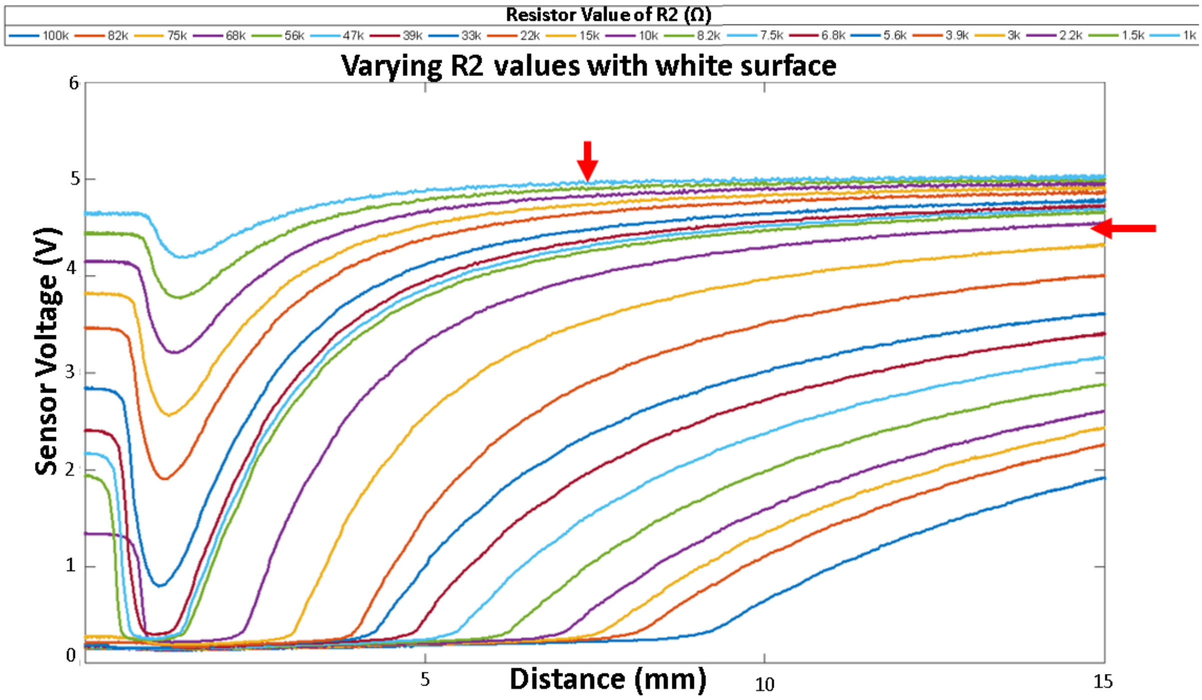

Figure 3.6: Optoelectronic sensor signal over increasing linear proximity to a white surface reflector. The value of the collector current resistance (phototransistor) R2 is varied between 1k-100k Ohms, while R1 is set to 150Ω. Red arrows indicate responses which are discussed in section 3.5

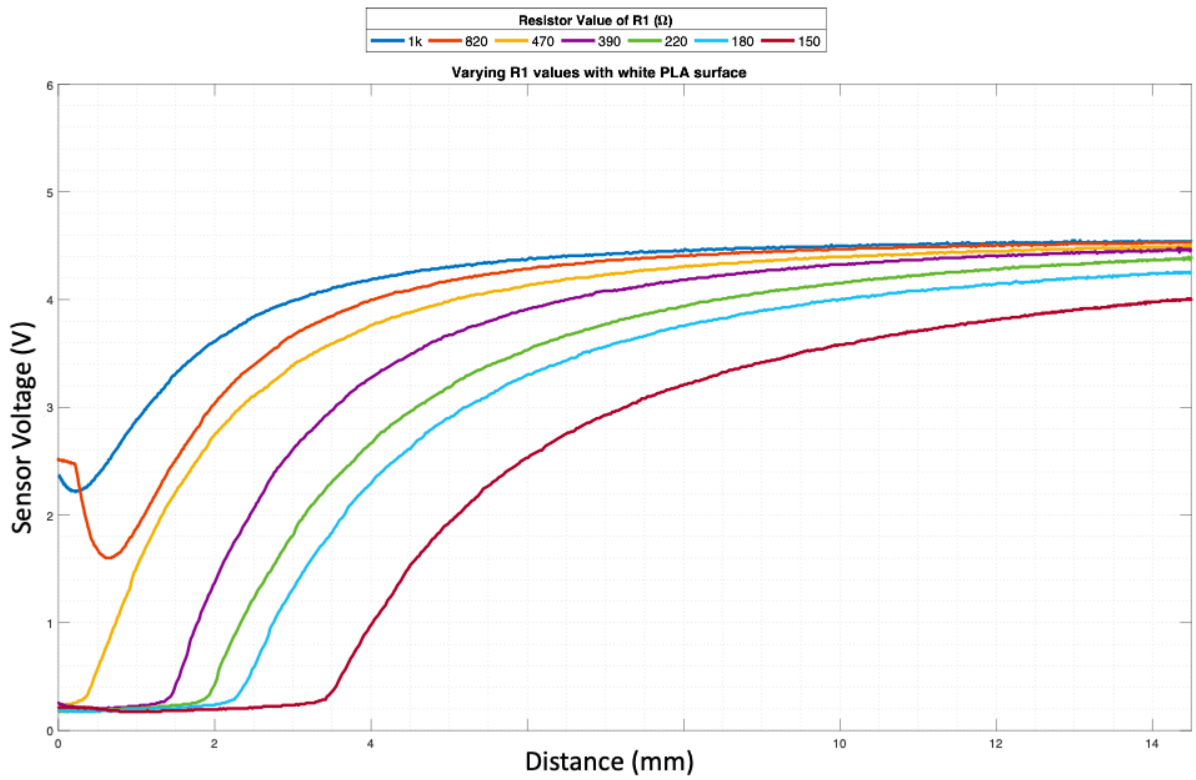

Figure 3.7: Effect of changing the LED resistance R_1, while fixing phototransistor resistor, R_2, at 22kΩ. As results in Figure 3.6 showed better sensing range using a white surface, only a white surface was

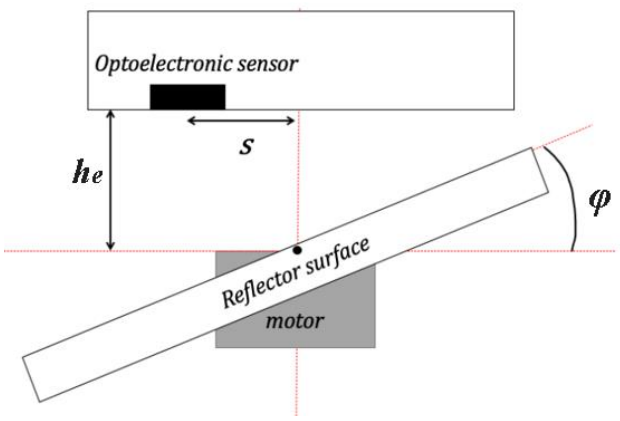

Figure 3.8: Experimental parameters such as reflector angle (φ), linear proximity h_e, and lateral displacement s, away from the central rotational axis, are considered in characterizing optoelectronic sensor response.

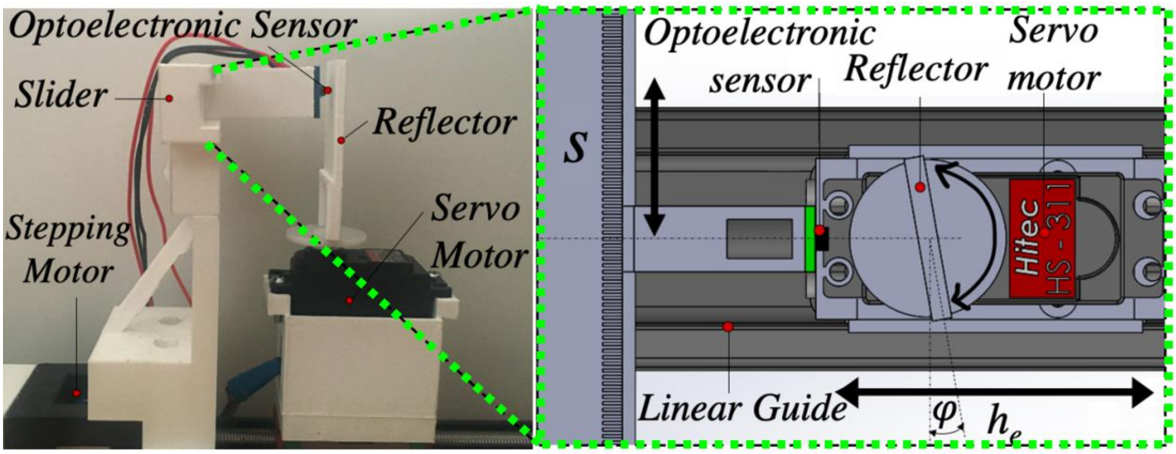

Figure 3.9: Experimental set up with optoelectronic sensor mounted to fixed rig, while reflector is mounted to rotating motor horn of a servo motor, which is attached to linear guide platform that can change linear proximity (h_e) to the sensor. Optoelectronic sensor can be manually adjusted along sliding rig to change lateral distance (s) away from the central axis [97].

Having already looked at the planar relationship between the optoelectronic sensor and a reflective surface with linear proximity and varying resistance values, the next step was to look at how varying the angle between the reflective surface and the sensor would change the characteristic behaviour.

An experiment is set up to recreate the parameters to represent the relationship between two-unit disks of the proposed flexible robot manipulator (Figure 3.1). These parameters are described by the diagram in Figure 3.8, and the experimental set up is shown in Figure 3.9. Figure 3.8 shows the sensor and the reflective surface; the first parameter is θ and described the angle between the reflective surface and sensor plane. The second parameter d, is the distance between the centres of the sensor and the reflective surface, as previously set by the linear guide. The last parameter, s, describes the lateral distance of the sensor away from the central rotational axis.

Considering the set up in Figure 3.9, a range of data is collated that varies within these parameters. A servo motor (HITEC, HS – 311) is mounted to the platform of the linear guide. To this, the reflector is attached, and the motor accurately rotates the reflector to a chosen angle (using Arduino IDE) relative to the sensor plane. The surface is set to 0 - 30° in one orientation relative to the fixed sensor. This reflector is allowed to travel a range between 0-

15mm away from the sensor using the motorised linear guide, whilst the signal data is recorded. This is done in the same way as in the previous experiment, where the Visual Studios Software is able to write motor position while reading in the sensor voltage data into an excel sheet. For each fixed reflector angle, multiple sets of data are recorded for the traversed path, while changing the lateral position (s) of the optoelectronic sensor. These data are shown in Figures 3.10 to 3.13. The collation of this data will give an overview of the behaviour of the sensor and represents parameters to consider in the design of the sensor positioning in the disks that constitute the eventual flexible robotic manipulator. It should help determine the optimal positioning of the sensors on the disk, by finding a combination of good signal strength, and minimalization features.

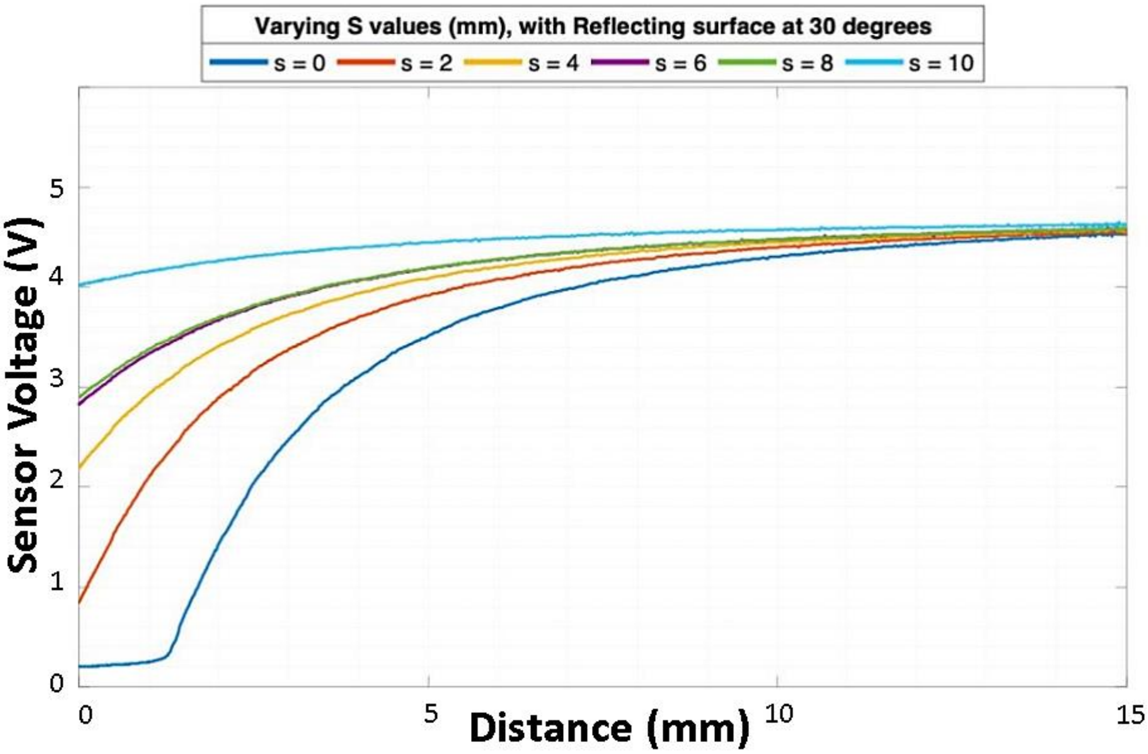

Figure 3.10: Based on experiment shown in Figure 3.9, graph shows varying lateral distances, s, of the sensor, with the reflective plane set at a 30° angle for pitch [97]

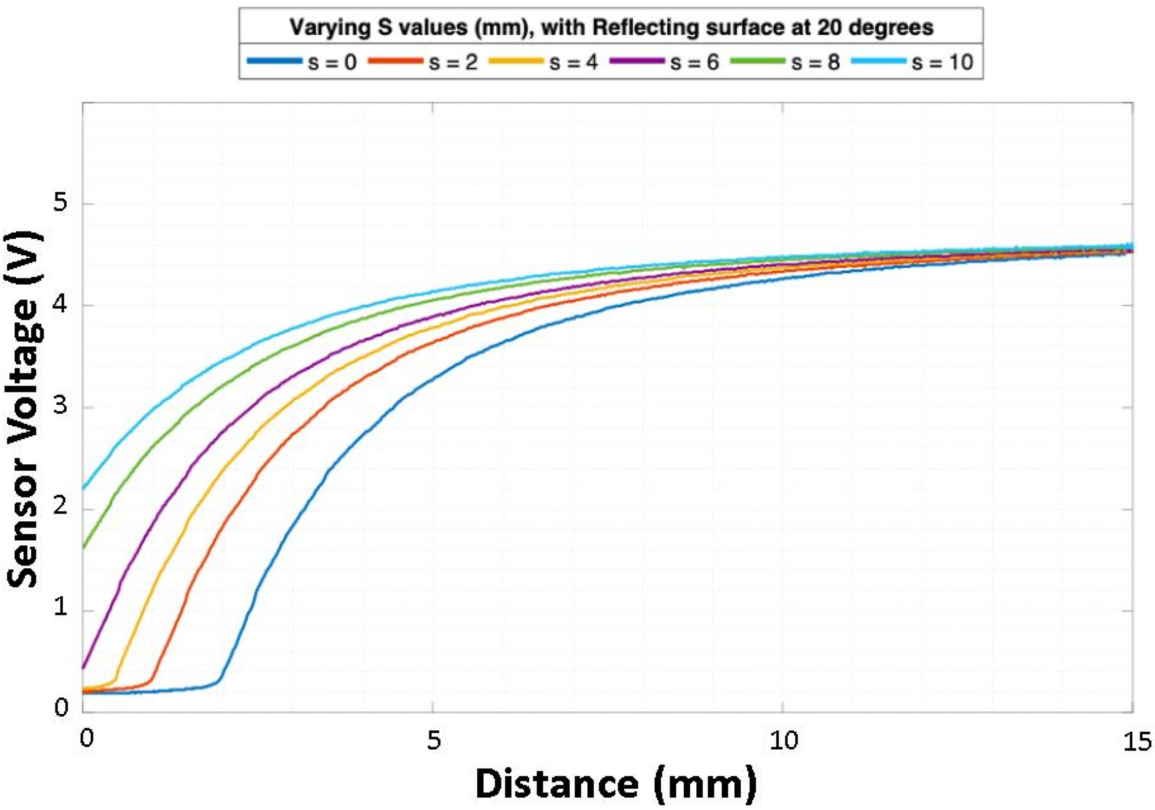

Figure 3.11 Based on experiment shown in Figure 3.9, graph shows varying lateral distances, s, of the sensor, with the reflective plane set at a 20° angle for pitch [97]

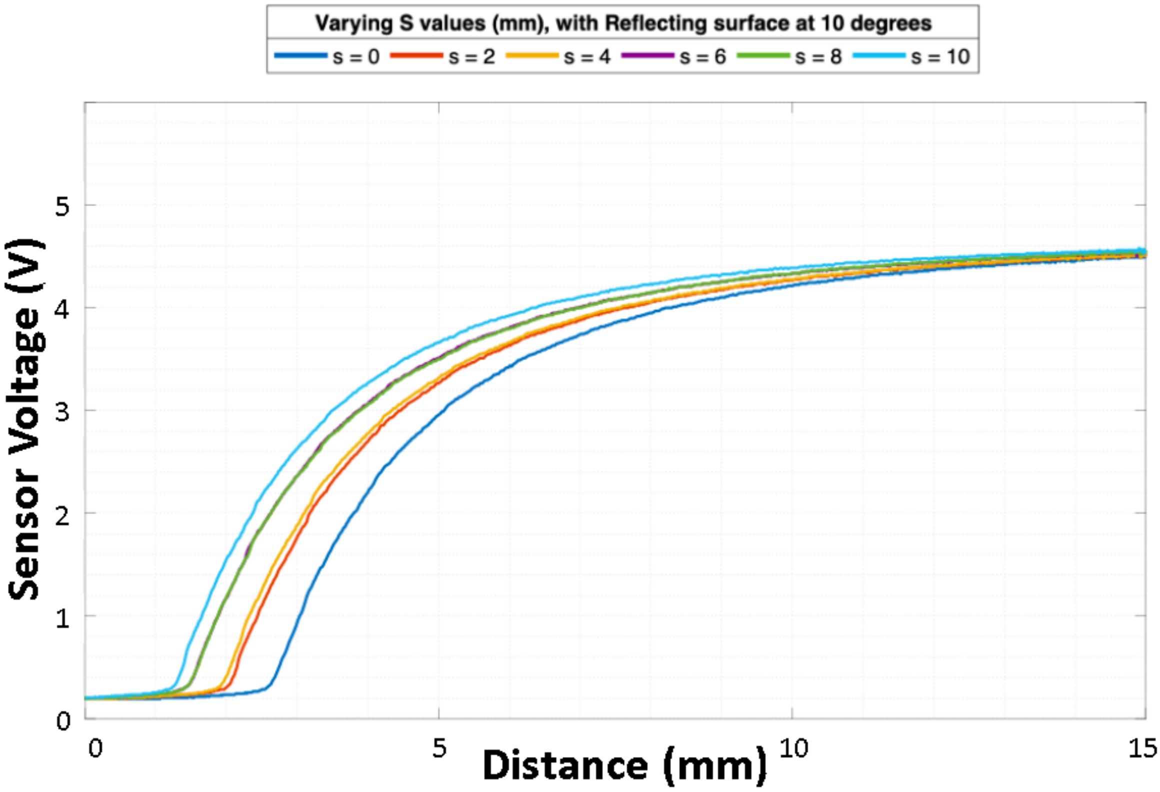

Figure 3.12 Based on experiment shown in Figure 3.9, graph shows varying lateral distances, s, of the sensor, with the reflective plane set at a 10° angle for pitch [97]

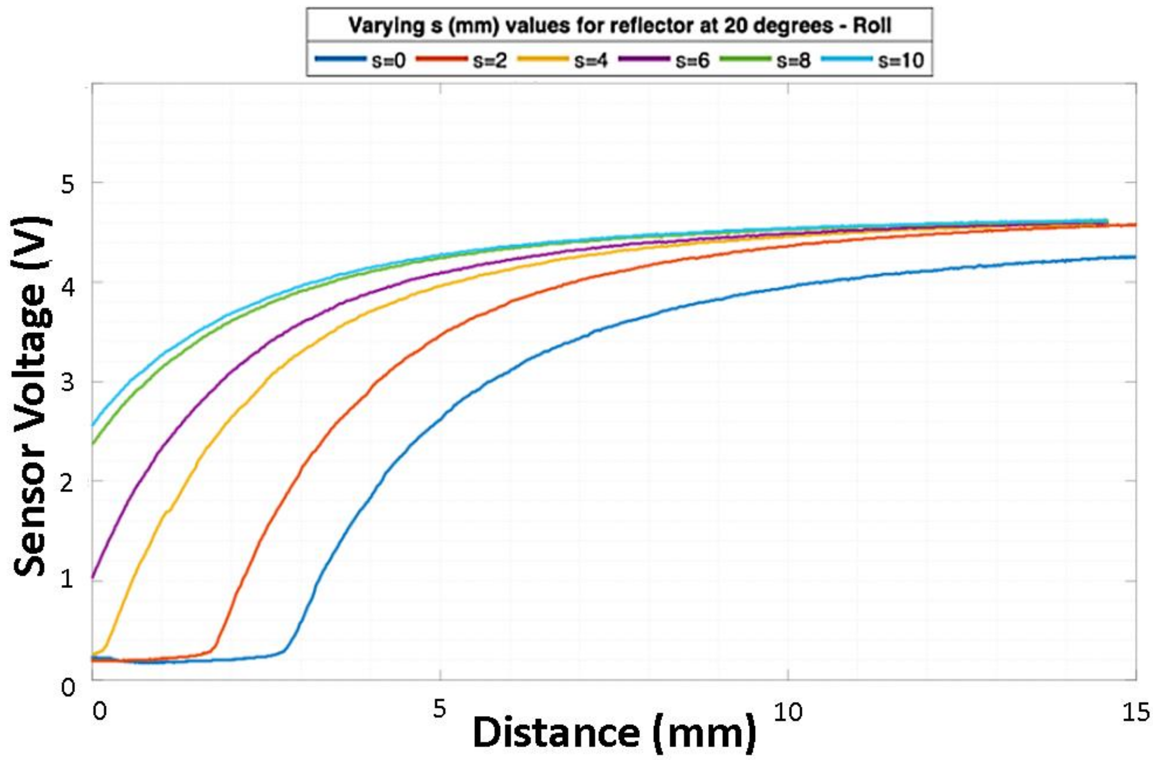

Figure 3.13: Based on experiment shown in Figure 3.9, graph shows varying lateral distances, s, of the sensor, with the reflective plane set at a 20° angle for roll [97].

3.5 Experimental optoelectronic sensors characterisation: Analysis

Effect of changing R_2:

Figures 3.5 and 3.6 show the results of the experiment to identify the sensor behaviour with different reflective surfaces, as well as different resistance values for the phototransistor current. The LED resistor R_1 was set at 150Ω, which is a low operational value to allow a high intensity light level to be emitted from the LED. The response seen in the data follows the expected characteristic behaviour, for example the top-most line seen in Figure 3.6 (light blue, identified with red arrow), for an R_2 value of 1k Ω. At small distances from the reflector, the voltage signal stays relatively constant, this is likely due to the sensor being too close to the surface to be able to reflect the IR light into the collecting phototransistor (beam of light is not able to fully illuminate the phototransistor at this distance). As displacement increases, there is a voltage drop, where more light is being accepted by the phototransistor. This induces a large current, hence the large voltage drop, with inverse relationship. Once the maximum amount of light has peaked, this corresponds to the lowest voltage signal. From this point, the signal increases nonlinearly with increasing distance away from the surface. This corresponds to the inverse proportionality between light intensity and distance, meaning that as intensity is lost with distance as it dissipates, the current collected by the PT is reduced. This continues until the signal plateaus, reaching dynamic range limit of 5V. For a white reflective surface (Figure 3.6), this trend is seen for resistor values between 1kΩ to 10kΩ (identified with red arrows). At higher resistance values for R_2, this initial voltage drop is not seen, and the signal begins to increase at a certain higher displacement point, again in a non-linear fashion. A reason for this may be that at such high resistances, it means that there is not a large current flowing through the sensor.

Another observation is that the initial voltage reading level decreases with increasing resistance. This is probably again due to the low resistance values allowing an amount of light to induce a larger current, becoming easily saturated, compared to larger resistors that limit the current. For example, 1 kΩ had initial readings close to 5V, while 10 kΩ starts at around

1.5V. The section where the signal increases with increasing distance changes in steepness depending on the resistance. At low resistances, this portion of the curve is flatter, and the signal plateaus quickly. At higher resistances, the sensing range increases, with a steeper curve, however this range is reduced again with exceedingly higher resistances as sensitivity is reduced. This is perhaps the most important aspect of the characteristic curve, as it is important to find a suitable sensing range within a specified change in displacement. For example, comparing 10 kΩ and 100 kΩ lines in Figure 3.6, the latter has a smaller dynamic range compared to the steeper former curve. For the design of an accurate sensor, sensitivity is important, hence the steepest and most linear section of the curve over a large displacement range is extracted. For this reason, it was decided that the results for the white reflector surface (Figure 3.6) showed better performance in this aspect. Black reflective surface (Figure 3.5) showed overall a smaller sensing range over the resistors tested, with lower resistance value curves displaying saturation. However, for larger resistance values the curve had a larger voltage range in the space between around 2-5 mm. For the white surface, curves were smoother and also had a larger sensing range between 2-5 mm, however these were for lower valued resistances, for example comparing the curve for 100 kΩ and 8.2 kΩ.

Considering Figure 3.1 shown earlier, depending on the amount of tilting between the two plates in the proposed design, the displacement between the plates is a parameter that can be extracted from the curves to give optimised sensing range. Therefore, as the white reflective surface displayed curves with larger voltage range over larger displacement, this was focused on for choosing a resistor configuration for the remainder of the experiments. However, there is an advantage in choosing a high resistance configuration, in order to reduce electrical current flowing through the system in a final design of a robotic manipulator, improving safety. Yet, amongst all the curves in Figure 3.5 and 3.6, the higher resistance valued curves show a usable range beginning at further displacement, such as 22 kΩ, which has a usable sensing range above 4 mm. For this reason, a way to shift this curve to the left along the x axis, to be able to sense within closer distances to the surface, was investigated by altering the value of the LED resistor, R1. This is discussed below.

Effect of changing R_1:

The LED resistance, labelled R_1, limits the LED current. The effect this has is to limit the light intensity emission, this theoretically results in less reflected light being received by phototransistor, and this effect was investigated, for which results are shown in the Figure 3.7. Here the 22 kΩ phototransistor resistor (R_2) was chosen, as this displayed a large sensing range in Figure 3.6. As explained in the previous section, a pattern seen in choosing a higher phototransistor resistor value for the optoelectronic sensor meant a more distant range of sensor data that could be used. The results show that by increasing the value of the LED resistor from the initial value of 150 Ω, the curve shifted up to the left. This meant that the rising part of the curve increases at shorter distances away from the reflector, and this range also increases with the initial voltages rising. However, as R_1 values continue increasing, this steep curve begins to flatten, meaning that an optimal value can be chosen, depending on the distance range required by the sensing unit.

In the case of the relationship between two disks of the robotic manipulator (such as the concept in Figure 3.1), the middle of the range would be the neutral distance between the plates, with the minimum and maximum distances (d_1, d_2) corresponding to the maximum bending angles, on each side, as shown in the diagram (Figure 3.14). The range with largest change in sensor signal allows higher sensitivity. In the case of the following sections, the configuration of 22 kΩ for phototransistor resistance (R_2) was chosen, with 390Ω for the LED resistance (R_1). At this stage of the project dimensions are scaled up for the sake of studying the behaviour of the optoelectronic sensors. In future steps of the project minimisation of prototypes will be achieved, and this data will be useful to establish design dimensions based on specification requirements.

Effect of changing s position of sensor:

With the reflector surface set at an angle (10°, 20° and 30° in the pitch orientation), it can be seen from Figures 3.10, 3.11, and 3.12 how the placement of the sensor away from the rotational axis (s) can affect the signal, with changing linear distance. With increasing values of s, the geometric distance between the sensor and the point at which reflection occurs at the surface increases. This leads to curves becoming less steep, as there is less voltage change due to decreased current. Depending on the degree of tilting, there is also the signal range change is more significant where the angle is increased, where a change in s can give a largely different response. This data is therefore useful in deciding upon the placement of the sensor relative to the central rotational backbone in the potential design of a two-axis robotic manipulator. As this would be in two orientations – pitch and roll, it means that further investigation is required where two orientations are being used simultaneously.

This is important, as due to the geometry of the sensor, rotating a reflector in the roll position would give different readings to that rotated in the pitch direction (as illustrated in Figure 3.15). A difference can be seen in the graph Figures 3.11 and 3.13, both comparing 20° degrees tilts, where the angle was rotated in the pitch and roll direction respectively to measure some sensor readings with varying lateral distance *s*.

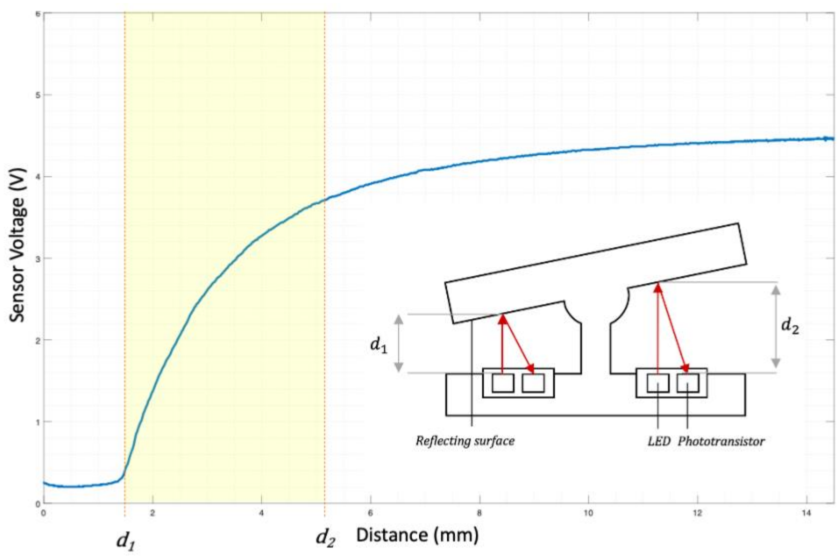

Figure 3.14: Concept of optimising sensing range through identifying ideal linear proximity change ($d_1 - d_2$) with tilting to achieve desired sensor response.

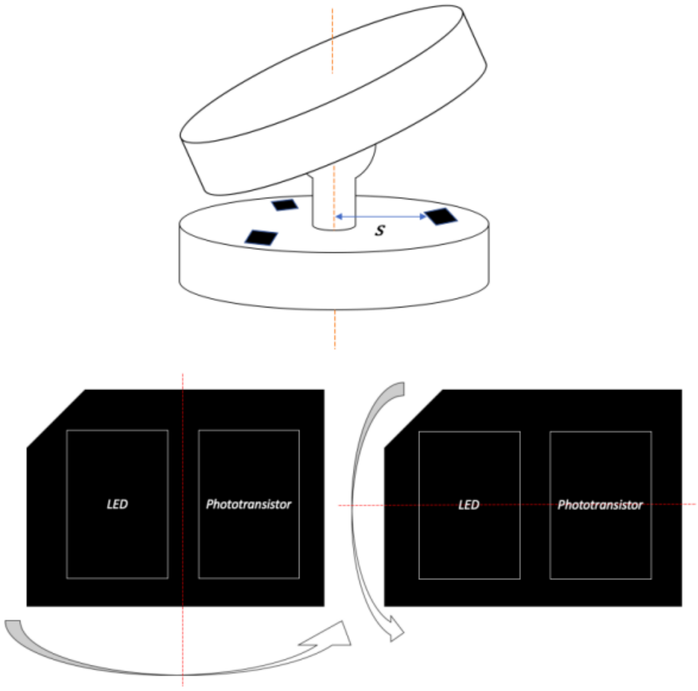

Figure 3.15: Illustration of how reflector angle in different orientations may affect sensor response.

3.6 Theoretical Sensor Model

The gaussian light distribution model is used to explicate the behaviour of light emitted and collected by an optical device. It assumes that light is emitted from a particular source in a gaussian intensity distribution. This means the emitted light follows and intensity pattern shown in Figure 3.16, where the centre has the highest intensity, and diffuses out with increasing radius away from the centre. It also describes the collection of light from a virtual transmitter, that can be modelled based on the geometry of the set up being used. It has been used extensively in modelling of optical fibre sensing devices, such as in [91][92], [93], [94], [95], [96].

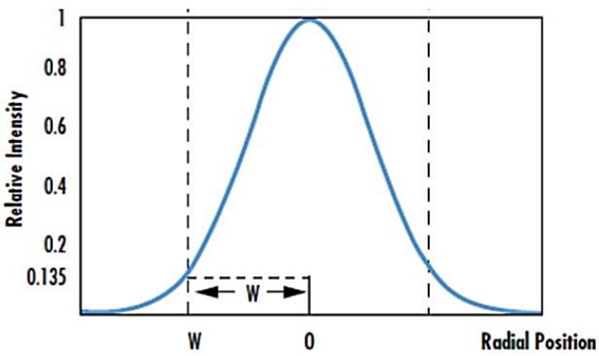

Figure 3.16: Typical Gaussian Light Intensity Distribution

The work of Polygerinos et al demonstrates such a model for describing the behaviour of a pair of optical fibres with an angular surface, assuming that an elliptical cross section of the reflected beam on the projection surface can be used to calculate the flux collected by the receiving fibre [92].

This inspired the theoretical model for the optoelectronic sensors used in this project and are geometrically modelled in a similar way in order to derive the equations, for a novel model. Figure 3.17 shows the geometry of the optoelectronic sensor and the reflective surface, based on the concept of two tilting plates of a tendon driven robotic manipulator in one orientation (as in Figure 3.1). Using this, and assuming gaussian distribution of light, a model can be composed that will relate the light intensity being emitted, to the collected light intensity by the phototransistor and the output signal. Since light intensity is directly proportional to electrical current/power, this allows the link between the emitting current and collecting current to be described. This would be done by finding transforming coefficients to link the quantities. This helps to directly predict signal values from given parameters and geometries, and to see how different parameters affect the signal output. This is validated by experimental trials described in the following section.

Figure 3.17a can be explained as follows: The optoelectronic sensor is fixed, with a reflector set at a variable distance h, that is able to rotate about the central axis normal to the sensor plane. The optoelectronic sensor used in this work (QRE1113) couples an LED and a Phototransistor. The amount of reflected light collected by the phototransistor portion of the sensor will depend on the axial distance h, the angle φ that is formed between the sensor plane and the reflector plane, as well as the lateral 'sliding' distance s between the central axis and the centre of the sensor structure. These variables modulate the light intensity, which outputs as a voltage signal between 0-5 V. To model the intensity level that is collected by the sensor it is first assumed that the light emitted from the LED source has a Gaussian light intensity distribution. For a short range, it can be assumed that the light travels in a conically formed beam. Equation (3.1) shows this general relationship in Cartesian form:

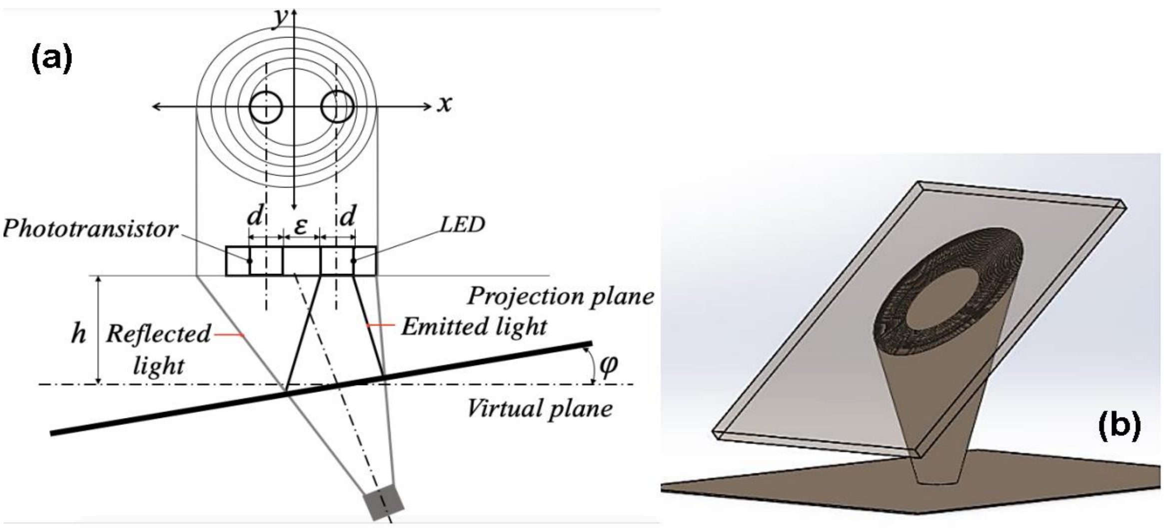

Figure 3.17: (a) Light is emitted from LED (r = 0.4mm) with beam angle θ and projected on to an angled surface. A virtual LED source is modelled on a virtual plane, with max light intensity I_0' along the z' axis, projecting an elliptical beam on the project. (b) reflected light hits the projection plane with an elliptical cross section of this conical distribution [97].

$$I(x,y) = I_0 e^{-2\left(\frac{x^2+y^2}{\omega_0{}^2}\right)} \quad (3.1)$$

where I_0 is the maximum intensity at the centre of the distribution, and ω_0 is the mode field radius which is 1/e of the peak intensity. This light is then reflected on the angled reflector surface and back to the projection plane. With the aid of a virtual diagram to map the path of the reflected projection, it can be seen that the reflected light hits the projection plane with an elliptical cross section of this conical distribution (Figure 3.17b). Hence, the light intensity emitted by the virtual LED source can be described by Equation (3.2):

$$I = I_0' e^{-2\left(\frac{x^2}{a^2}+\frac{y^2}{b^2}\right)} \qquad (3.2)$$

$$\phi_c = \int_{h\tan(2\varphi)-\frac{3}{2}d-\varepsilon}^{h\tan(2\varphi)-\frac{1}{2}d-\varepsilon} \int_{-\sqrt{\left(\frac{d}{2}\right)^2-(y-h\tan(\theta)+d+\varepsilon)^2}}^{\sqrt{\left(\frac{d}{2}\right)^2-(y-h\tan(\theta)+d+\varepsilon)^2}} I^{-2\left(\frac{x^2}{a^2}+\frac{y^2}{b^2}\right)} dydx \quad (3.3)$$

where I_0' is the new maximum intensity, with gaussian elliptical widths a and b. Here, a symmetric intensity distribution is assumed to simplify the model, as the non-centred elliptical distribution pattern can create complexities in solving for the flux. The portion of light that is collected by the phototransistor is solved by calculating the total flux over the area of the phototransistor, represented by Equation (3.3), where ϕ_c is the collected flux, with the limits of integration found by geometrically finding the boundaries of the circular LED and phototransistor structures. Here, a^2 and b^2 represent the major and minor elliptical beam widths. As the reflected light projects elliptically, these widths can be found by setting up an intersection plane onto a conical formula along the z' axis, solving for the equation of an ellipses, as described:

$$\frac{x^2+y^2}{c^2} = my + n^2 \qquad (3.4)$$

$$c = \tan\theta \qquad (3.5)$$

$$m = \frac{\sin(2\varphi)}{\cos(2\varphi)} \qquad (3.6)$$

$$n = \frac{h}{\cos(2\varphi)} + h + \frac{d}{2\tan(\theta)} \tag{3.7}$$

Shown is the equation of a cone with a substitution of the projection plane. c represents the cone slope coefficient, which depends on θ, m represents the slope of the projection plane relative to the central beam axis z', while n is its intersection with this axis. This is evaluated into the general form of an elliptical formula:

$$\frac{(x-x_c)^2}{a^2} + \frac{(y-y_c)^2}{b^2} = 1 \tag{3.8}$$

Which results in the values for a and b being calculated by:

$$a^2 = c^2n^2 + \frac{m^2n^2c^4}{1-c^2m^2} \tag{3.9}$$

And the centre of the ellipses is:

$$b^2 = \frac{a^2}{\cos(2\varphi)(1 - c^2m^2)} \tag{3.10}$$

$$x_c = 0 \tag{3.11}$$

$$y_c = \frac{m^2n^2c^4}{1 - c^2m^2} \tag{3.12}$$

The equation for the theoretical phototransistor signal voltage can then be formulated:

$$V_{th} = \phi_c \cdot R \cdot k_v \tag{3.13}$$

where light losses are represented by reflection rate R and conversion/transformation coefficient is introduced by k_v, that converts the collected flux into a voltage value. Depending on a particular application, it is beneficial to model the behaviour of such a sensor in terms of these factors as this would allow one to set design parameters.

3.7 Validation of Theoretical Optoelectronic Sensor Model

To validate this gaussian theoretical model describing the optoelectronic response to various parameters, experimentally measured sensor voltage outputs were compared against theoretically derived values of sensor output. Using the experimental set up in Figure 3.9, the optoelectronic sensor was placed along the central axis (s = 0), and the reflector was set at various angles (φ) between 0°-30°, while linear displacement (h_e) was changed through linear guide motion. These results are shown in Figure 3.18. Secondly the optoelectronic sensor was placed at various lateral distances (s), 0-10 mm, with the reflector fixed at 20° (φ). Sensor output during linear guide motion (h_e) was also recorded. These results are shown below in Figure 3.19.

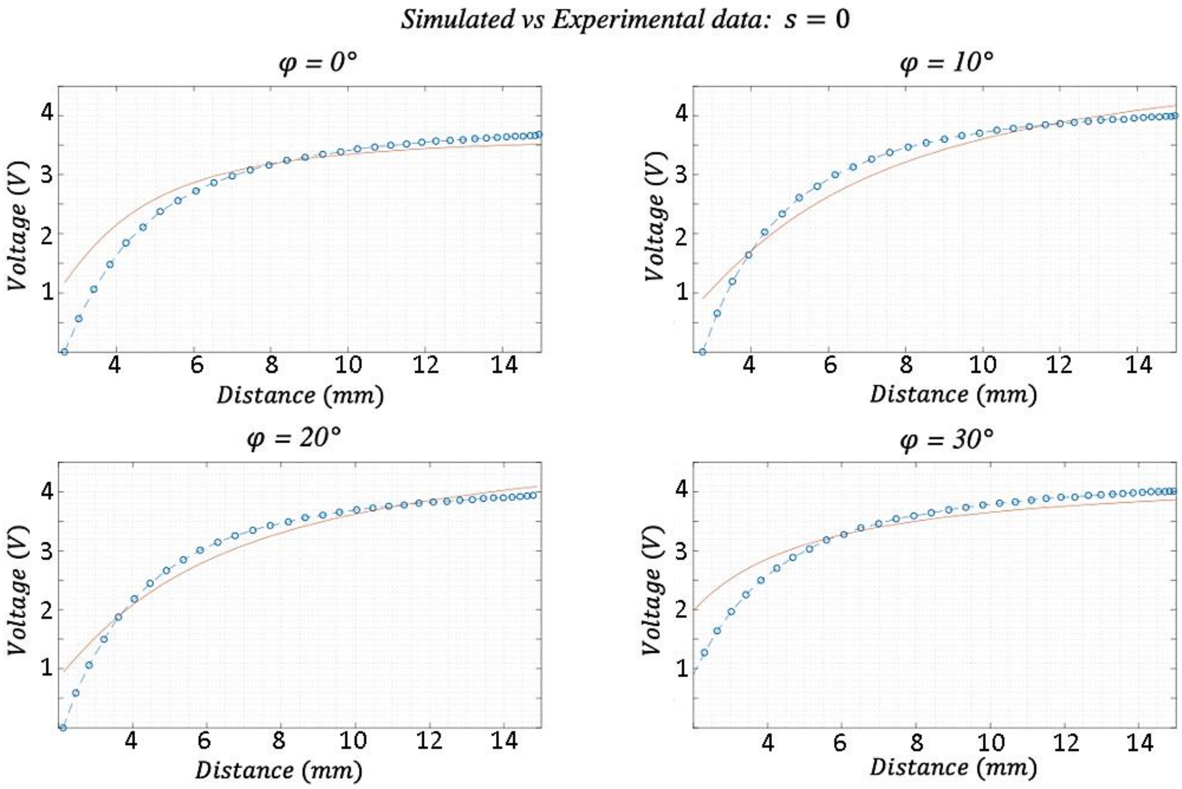

Figure 3.18: Experimentally collected sensor voltage data (blue dotted), with changing reflector angles (φ), compared against model simulated output voltage against displacement (orange), calculated using mathematical model, using the same input equation parameters [97].

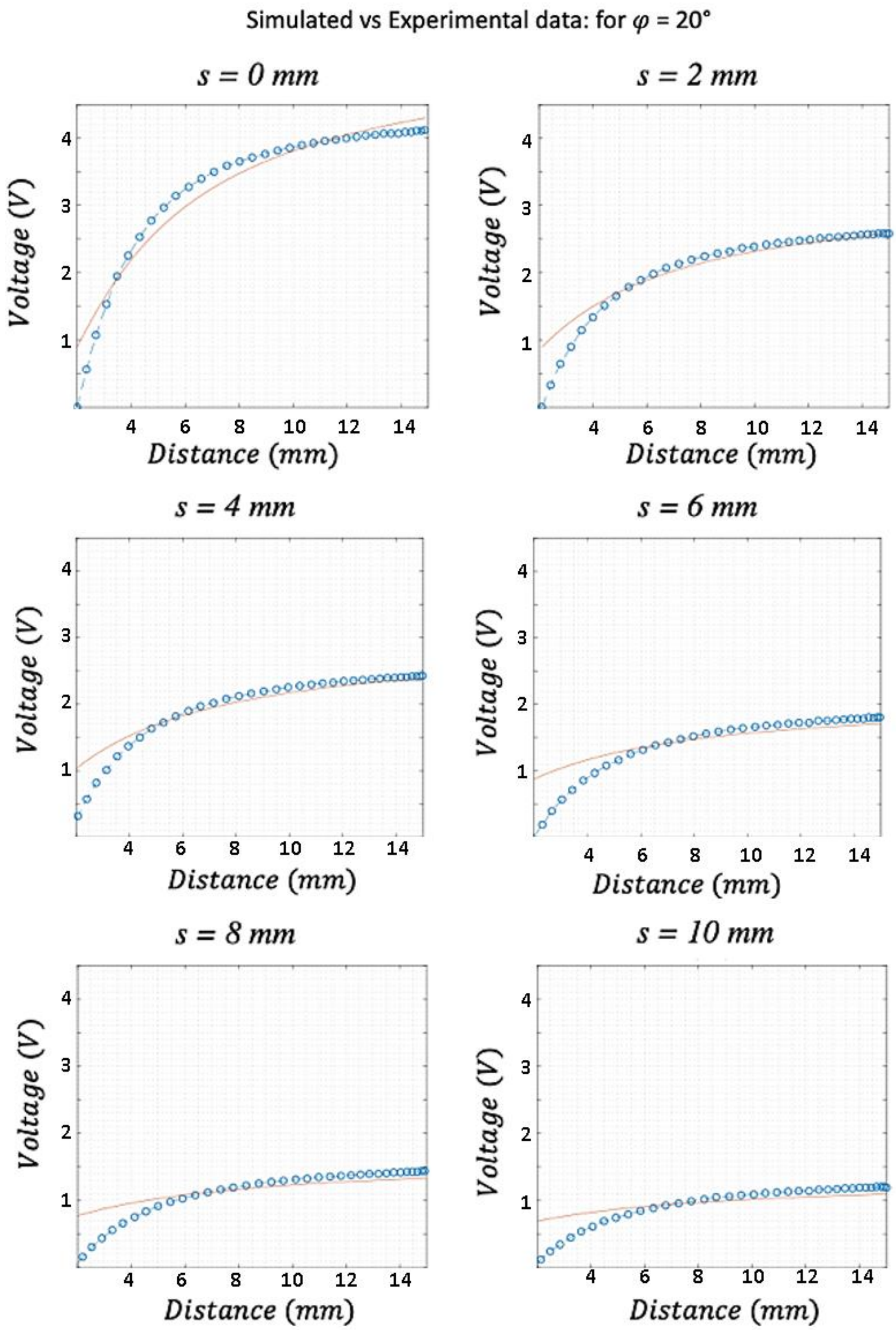

Figure 3.19: Experimentally collected sensor voltage data (blue dotted), with changing lateral sensor placement (s), with reflector angle set to 20° (φ), compared against model simulated output voltage against displacement (orange), calculated using mathematical model, using the same input equation parameters [8].

3.8 Model Validation Analysis

The data collected in the above experiments were for the rotational angle of the reflector set at angles φ: 0°-30°, with s = 0, with another set of data collected where the lateral distances are set to: 0, 2, 4, 6, 8 and 10mm, with φ set to 20° (Figures 3.18 and 3.19). With these parameters set, the voltage over a predetermined linear displacement (0-15mm) was recorded by software and plotted. The same parameters were provided as input to numerically solve equation (3.3) to get required flux. This was done by inputting the model's equations into MATLAB to solve. For a white reflective surface, we can assume 90% reflection rate, as this provided the best fit to the experimental data. The coefficients corresponding to $R \cdot kv$ (from equation 3.13) were calculated through a least of squares regression algorithm and were required to simulate the theoretical output voltage of the sensor.

It can be seen from Figures 3.18 that the experimental data generally fits the simulated curve, however there are noticeable errors. With regards to Figure 3.18, the RMS errors are 0.2973, 0.2161, 0.2105 and 0.4034 for 0°, 10°, 20°, 30° respectively. One reason for this could be due to the assumption taken that the gaussian distribution around I_0' is symmetrical. This may have distorted the mathematical model, leading to experimental data unable to fit the predicted pattern. Another reason could possibly be simply due to the fact that experimentation may have has a source of human error, in the manual placement of the sensors. Resistors were added to the optoelectronic circuit during the experiments, to vary the amount of light intensity emitted and collected by the sensor. Depending on the resistor values, this would have caused a shift in the experimental data due to larger or smaller current induced voltage drops over the region of smaller displacement values. This may be the reason for the difference between the simulated model and the experimental data, as the mathematical model did not take into account resistor values that may have been used, and this could be an improvement in further work on the modelling of the sensor.

For larger displacements however, the model fit improved. Another factor for the deviation of the experimental data from the model may have been due to geometrical set up of the experiment. The reflector surface could potentially have been too small, as well as rough, meaning that less light was collected by the sensor than predicted, and scattering off the 3D printed PLA reflector may have caused an under or overestimation of intensity collected by the phototransistor. Further work may also be done to model based on two orientations, using similar gaussian assumptions.

3.9 Conclusion

This chapter explored the characterization of an optoelectronic sensor. The study examined various parameters affecting sensor performance, including proximity, angle, surface texture, and electrical properties. The insights from this study provide a foundation for optimizing sensor placement and configuration in future shape sensing system designs for robotic manipulators. A mathematical model based on Gaussian light intensity distribution was developed and validated through experimental data. The developed theoretical model closely aligns with experimental results, though minor discrepancies suggest potential improvements in modelling assumptions and experimental setup, although can be used to propose further optoelectronic sensing configurations beyond that demonstrated in the experimental sensor study and establish feasibility for any design.

Chapter 4: Novel One-Axis Joint Angle Sensor And Two-Axis Tendon Actuated Robot Integrating Optoelectronic Shape Sensing With A Planar Reflector

4.1 Introduction

In this chapter, the optoelectronic characteristic study from chapter 3 is considered in the design of both a one-axis joint angle sensor, and two-axis tendon actuated robot, integrating optoelectronic shape sensing.

A simple, novel, one-axis joint sensor is fabricated, consisting of a single optoelectronic sensor, opposing a flat reflector connected by a hinge type joint, similar to a finger-like link mechanism. This is tested using an experimental set up, to establish the feasibility of using optoelectronic sensor for joint angle measurement and for further, more complex shape sensing, for robotic applications.

This leads to the novel design of a shape sensing technique as described by Fig 3.1, which integrates a set of three optoelectronic sensors into each disk of a tendon actuated continuum robot. The sensors emit light, which reflects off the lower surface of the upper disk. This reflected light varies in each of the three sensors, depending on the tilting of the upper disk. This is recorded as a voltage varying signal, where three voltage values from each sensor can be used to estimate the orientation of the upper plate after calibration. Once this is done for each consecutive plate, the overall orientation and shape of the manipulator can be reconstructed.

This is the first type of shape sensing technique known to use sets of optoelectronic sensors directly embedded in a flexible continuum robot to estimate shape in up to 6 DOF.

This chapter will therefore lay out the design and fabrication of the tendon actuated robot and shape sensing integration, the interfacing software and actuation system, the calibration experimentation platform to evaluate the shape sensing, as well as the results of the evaluation of calibration experiments.

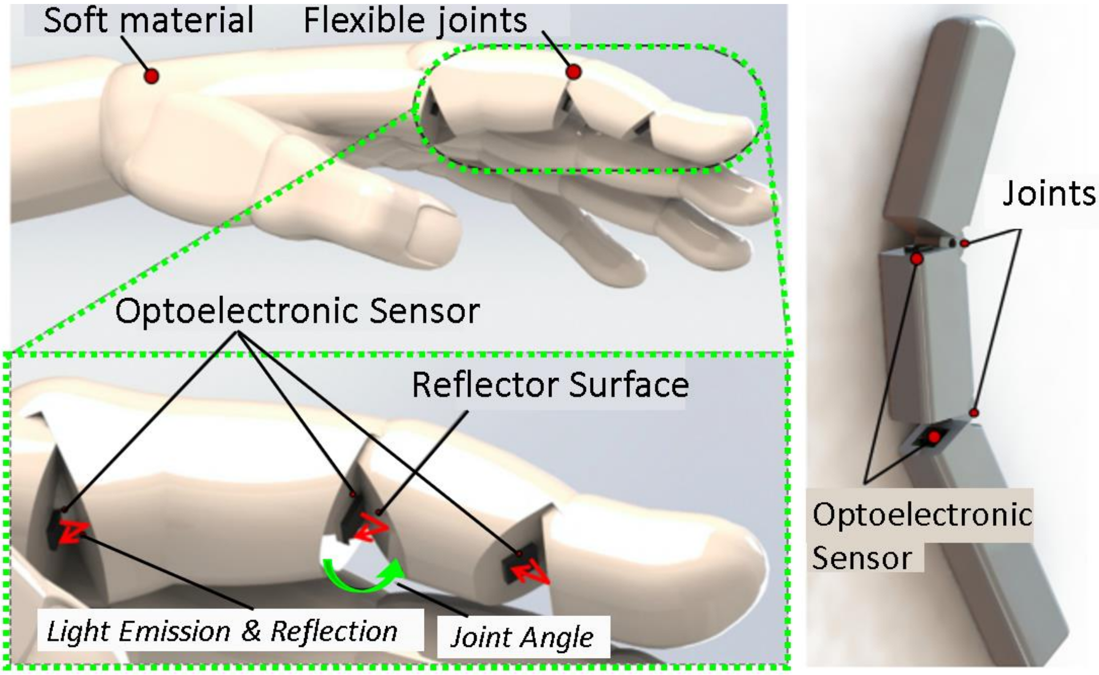

Figure 4.1: Concept idea for one-axis optoelectronic based joint angle sensor for robotic prosthesis application, using a flat reflector. The sensing principle is based on intensity modulation, which depends on proximity of the sensor to the reflector. The proximity, therefore, voltage signal, will vary with changing joint angle [97].

4.2 One-axis Optoelectronic Joint Angle Sensor

4.2.1 Background of one-axis joint angle sensors for robotic application

In Chapter 3, the linear distance between the optoelectronic sensor and reflector is understood. It is possible to consider the use of the optoelectronic sensor as a joint angle sensor, when paired with an angle changing reflective surface. This study was carried out, and was published in [97], by designing a simple optoelectronic joint angle sensor that bends in one degree of freedom. A concept idea for application of this optoelectronic joint angle sensor is shown in Figure 4.1. Some advantages of this design can be identified when considering some of the one-axis joint angle sensors seen in the literature as well as commercially in the field of robotics.

For example, many industrial robot arms, as well as robot hands have utilised single degree joint angle sensors for grasping and manipulating objects to targeted positions in a precise and dextrous way[98], [99]. However soft and flexible robotic tools, such as ones also used in MIS as well as for robotic prosthetics require miniature joint angle sensors embedded directly at the joint in a way that would not hinder its flexibility or material properties is required; and this is different to commonly used joint angle sensors in more industrial applications, as these are commonly larger sensos such as magnetic and rotary encoders, hall sensors [100]. Due to their size, they would need to be installed externally in small joint applications, along with a tendon mechanism. However, this is not always an ideal option, as tendons can experience stretch under large tensions as well as slack, meaning that joint angle position cannot always be estimated accurately externally [101][102].

It is for this reason that miniature sensors are more ideal if they are able to integrate directly within the joint. This can be seen for example in small rotary resistive sensors, although despite their size, it has been known that friction between the carbon film and resistive track are prevalent, leading to shorter mechanical life [103]. There have been cases of optical based method used for joint angle sensing, for example[67], who use fibre optic cables embedded into the joint of a snake-like robotic manipulator. Using a mirror at each joint, the modulation of light intensity with changing angle can be detected by a phototransistor placed remotely. While fibre optics a very flexible and narrow, it is possible that this may not be the best option if multiple fibres a requires for multiple serially linked joints, as this can build up in bulk and stiffness. Another technique utilised an LED and Photodiode detector opposing one another within a 'variable-thickness canal' inside a robotic finger joint, where a similar light modulated principle is used as the joint angle changes [104].

In this following section, the embodiment of a new miniature rotary measurement sensor prototype for integration into robotic joints will be presented using the optoelectronic sensor and utilised to test some of the sensor characteristics with changing reflector angle. Considering this joint angle sensor development, some of the advantages are that the low-cost optoelectronic sensor is small, meaning that it can easily fuse within joint structures, enabling the miniaturisation of the entire robotic structure. These sensors do not suffer from mechanical wear, and their signals are not interfered by external sources such as ambient light or electrical or magnetic interference.

4.2.2 Design of optoelectronic one-axis joint angle sensor

As shown in Figure 4.1, the sensing principle is based on the modulation of light intensity to estimate bending angle in one degree of freedom. The used optoelectronic sensor (QRE1113) is made up of an LED source, coupled with a phototransistor to detect light reflected off an opposing surface.

In employing this principle into the finger joints of a robotic hand application, the joint degree of rotation can be estimated in one orientation, based on the amount of reflected light to the PT. As one end of the link rotates, it functions as a reflective surface, causing fluctuations in light intensity as it reflects onto the PT.

A simple finger prototype (Figure 4.2) is designed comprising of two jointed links, to allow one degree of rotation. One of the links was grounded, while the second link was fixed to a motor horn attached to a servo motor, with the joint screwed at the centre of the motor horn (central rotation axis). The optoelectronic sensor was attached to the flat end of one of the links, while the flat surface of the second link was utilised as the reflecting surface. The parts were designed on SolidWorks, and 3D printed.

This set up was used to gain experiment results on using the sensor output to estimate the joint angle. To do this, the servo motor was set to continuously rotate within a set angle range, while the sensor voltage data was simultaneously recorded, using an Arduino Mega microcontroller board, to collect data into an excel file.

Through use of a regression algorithm, we could use the actual servo angle to map the sensor's voltage data to an estimate of joint angle. The experimental results are shown below, in Figure 4.3 and Figure 4.4.

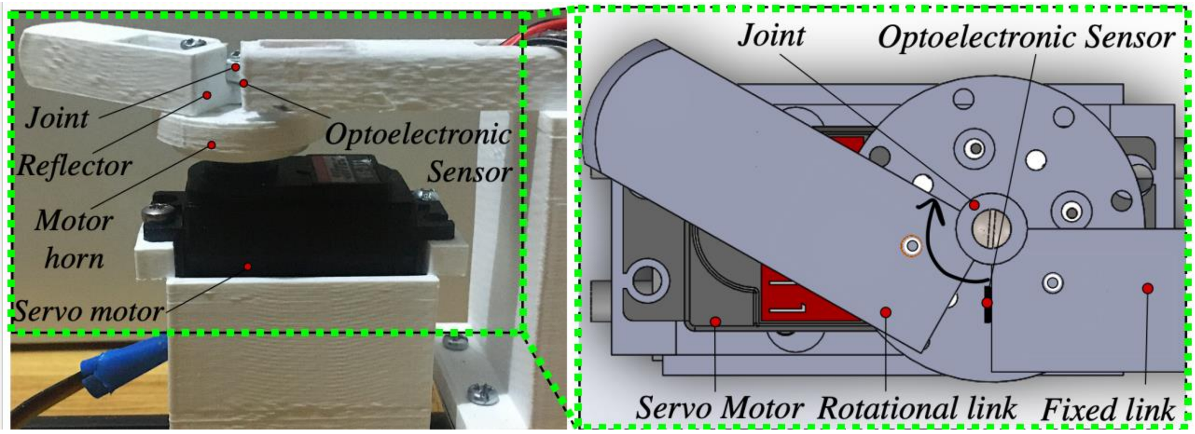

Figure 4.2: Experimental design of finger link joint angle sensor. Optoelectronic sensor is fixed on one face, with the face of the second finger serving as the flat reflective surface. These are coupled with a 'swiveling' hinge joint. This joint is coupled to a servo motor to allow rotational motion to carry out angular tests, while simultaneously recording optoelectronic sensor voltage data[97].

4.2.3 Optoelectronic one-axis joint angle sensor: Experimental results and analysis

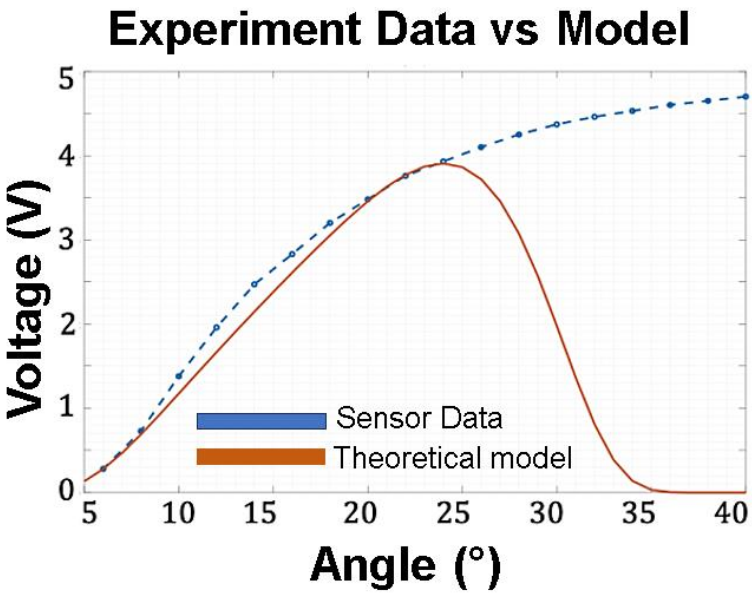

Figure 4.3: Experimental data (blue) of optoelectronic sensor voltage with varying reflector rotation of finger joint, compared with simulated optoelectronic sensor output signal (orange), generated by theoretical model from section 3.6 [97].

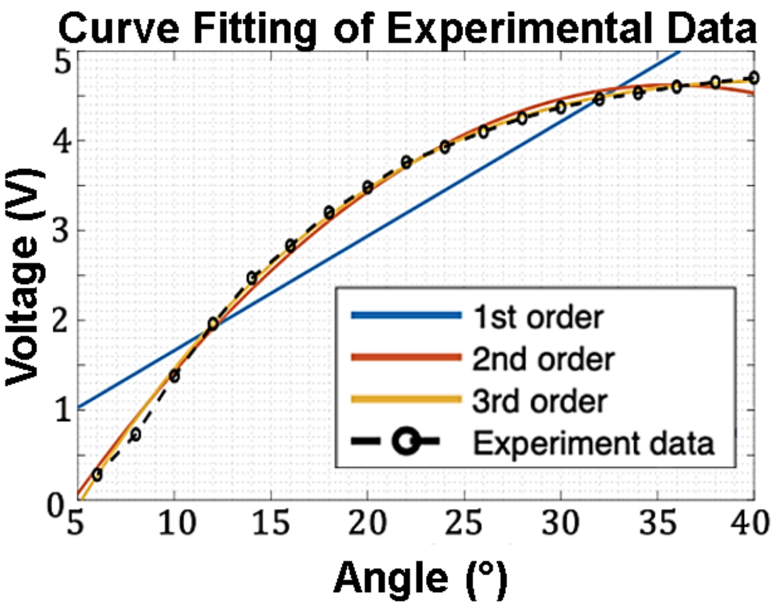

Figure 4.4: Experimental data (black) of the optoelectronic sensor voltage with varying reflector rotation of the finger joint, compared to 1st, 2nd and 3rd polynomial functions, for best data fitting [97].

Figure 4.3 compares the simulated output of continually varying the reflector angle relative to the optoelectronic sensor, based on the model. Although it appears at first to generally follow the tendency of the measured experimental data, the output voltage appears to drop after a certain angle. This can be explained theoretically, in that after a certain angular limit, the infrared light entering the phototransistor begins to reduce, as the beam can no longer be projected on the sensor plane. This presents itself as a drop in voltage in the simulated data. In reality, when this happens, the sensor measures a saturated output voltage equal to the supply voltage, as the light levels entering the transistor are so low that change in voltage is not seen. This property is not reproduced in the mathematical equations describing the model; hence it is not able to fully describe the sensor output behaviour with varying reflector angles. In future work these effects should be incorporated to provide a better estimation of the characteristic behaviour.

For this reason, another approach was taken to find a polynomial function to fit the data as in Fig 4.4, where 1st, 2nd and 3rd order functions are fitted. It can be seen here that the 3rd order function closely fits the experimental data, using least square based methods and can be used to map the output voltage values to the corresponding joint angle. The sensing range of the joint angles is between 0° – 40°. Future proposals may include considering different surface properties to increase the sensing range for application as a joint angle measurement sensor. For practical application, a cover should be designed to block noise due to external light.

4.3 Novel Two-Axis Optoelectronic Shape Sensing for a Tendon Actuated Robot

This section introduces the creation of a tendon actuated robot with integrated optoelectronic shape sensing. Taking the knowledge from Chapter 3, of the workings of the optoelectronic sensor in terms of its sensing characteristics and means by which this can be altered, as well as its use as a one degree of freedom joint angle sensor, these concepts are taken into account for the design of a tendon actuated robot segment which integrates a network of optoelectronic sensors for shape sensing in two orientations.

The robotic structure to be developed in this section is derived from the preliminary work of Koh et al [85], which was an initial proof of concept of the potential for optoelectronic shape sensing within a 3 disk-tendon actuated robot. Here, their design is used as a basis for the prototype, and a 4-disk tendon actuated manipulator is reconstructed with integrated optoelectronic shape sensing.

An experimental platform is designed to carry out an automated calibration process for each set of sensors in each disk of the flexible robotic manipulator. Calibration allows the sensor voltage values to be mapped to orientation estimations in pitch and roll, by finding a calibration matrix of coefficients. These coefficients are multiplied by the sets of sensor voltages to give orientation estimations. This improved calibration process shows improved shape sensing, with more accurate estimation of tip orientation angles. Different regression models are also explored in this section for finding the calibration matrix from data collected during calibration.

4.3.1 Tendon Actuated Robot integrating Optoelectronic Shape Sensing: Design Concept

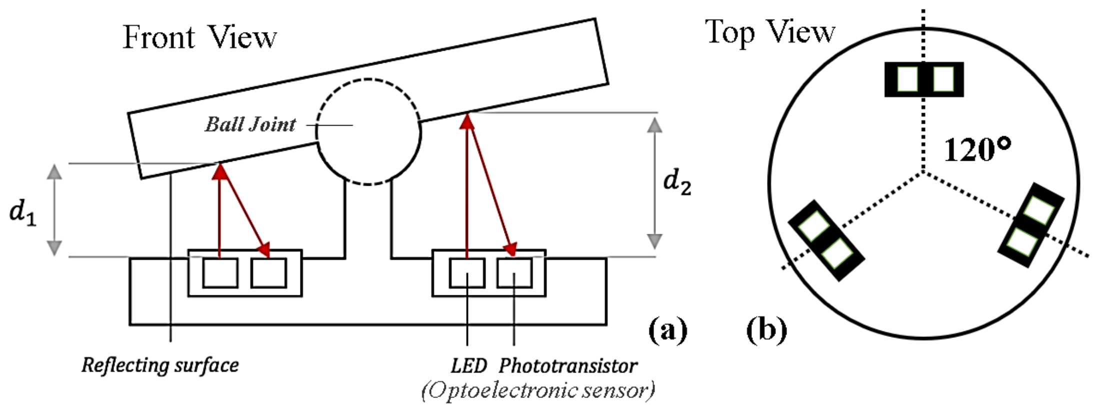

Figure 4.5: (a) Two-unit disks connected with ball joint. The degree of tilting varies the sensor voltage measured due to varied reflection (distance d_1-d_2). (b) Shows optoelectronic sensor placement on the disk, with the three sensors placed 120° apart.

As shown previously in Figure 3.1, the concept is to construct a tendon driven robotic manipulator. This would be made up of individual circular disks that fit together using ball socket connections and spaced using an elastic structure such as springs. As this is assembled using discrete links, while still maintaining elastic properties, this results in a pseudo-continuum robotic backbone manipulator that could be used for MIS purposes. In each circular disk, three optoelectronic sensors are to be placed circumferentially at 120° apart (Figure 4.5). This configuration is repeated at intervals on consecutive disks. As the upper plate tilts in relation to the lower plate, the upper plate acts as a mirror reflective surface, upon which three of the optoelectronic sensors emit and receive light off of (Figure 4.5). Depending on the degree of tilting, three different voltages would be output, that correspond to the distance to the surface, as opposed to the neutral case with the plates parallel to each other (no bending), where all three sensors should theoretically output the same voltage signal. This is the concept upon which this sensing principal works, where the tilt can be mapped to a set of output voltages. This design concept was previously started by Koh et al. [85], where each optoelectronic sensor was individually electrically wired along the flexible manipulator.

Referring to the different configurations of optical fibres as stated in Chapter 2, this was dependent of the DOF capabilities of the sensing principle in question. For example, cases where two optical fibres were used resulted in the device measuring one orientation of pitch and roll (planar case), while the triplet configurations allowed measurement of both roll and pitch in three dimensions. For this reason, the triplet configuration of uniformly spaced optoelectronic sensors will be investigated in this project, however there is potential for other configurations that can be explored, meaning a very adaptable shape sensing principal. As a reconstruction model can be developed to estimate the shape of the entire length of the robotic manipulator, this information, such as tip pose can be used in closed loop feedback control by inputting into a control system.

The reasoning as to why a novel shape sensing technique is required for continuum robots is recapped here, although this is more extensively described in Chapter 2. The focus of this section is to develop an alternative shape sensing technique that is integrated into the flexible robotic device that is miniature as to not interfere with functionality, as well as allow full positional and shape information for actuation and control. This has most commonly been done using microelectronic sensors such as inertial, electromagnetics and radiofrequency coils, as well as optical sensors such as Fibre Bragg Grating (FBG) sensors and fibre optics. Some of the issues with these included large sensor size, as well as signal interference and sensor drift. Shape sensing through optical fibres has also been a common technique, for example [67] using multiple optical fibres along each segment of a snake-like robotic device, to detect proximity change through varying light intensity detection. Such techniques however can affect the stiffness and size of a full-length surgical manipulator, thus affecting functionality of its purpose. Shape sensing using FBGs allow great flexibility and are miniature, there has been note of limitations in shape sensing with larger bending deflections of the flexible robotic tools, as well as in lower stiffness environments, due to increase in sensing error. FBGs can also suffer from temperature and wavelength shift over time and in varying environments, regular recalibration, and are also notable difficult to manufacture – leading to high costs for production.

The proposed optoelectronic based shape-sensing design maintains the advantages of an optical method, ensuring compatibility in an operative and industrial environment, where signals would not be affected by electromagnetic waves from various surgical or electrical equipment, as well as with CT/MRI based imaging modalities, and would not suffer from environmental effects such as temperature, external forces, or varying stiffnesses, due to the non-contact nature of the sensing modality. the system in very simple, and mainly comprises of the optoelectronic sensing units, which have a very low cost of around £0.32/unit. These can easily be mass produced and formed into printed circuit boards using simple fabrication techniques. Minimal peripheral equipment is required, as only an analogue to digital converter (ADC) device is required, which can also be sourced at a relatively low cost. One source of disturbance maybe ambient light, which can be eliminated once a soft cover in used over the flexible robot. These optoelectronics sensors are known to detect a large voltage variation without need for extra amplifiers and filters, and these light dependent sensors by nature ensure a high sampling rate. Additionally, the optoelectronic sensors are inherently miniature, which aid in allowing miniaturisation of the entire robotic structure. Finally, as optoelectronic sensors are based on essentially proximity detection, they are easily adaptable into different configurations other than the way shown here and can therefore be modified to work with different types of continuum robot structures including extensible structures.

For an initial exploration into this shape sensing method, a tendon actuated robot, which can be considered a pseudo-continuum robot, is chosen, for its simple design and actuation, which allows focus of investigating the optoelectronic shape sensing. These advantages demonstrate the great potential for this shape sensing method when compared to some of the existing techniques and demonstrate many features that make it suitable for robotic application.
As mentioned, Koh et al [85] had shown early stages of this shape sensing concept using a 3-disk tendon actuated robot segment. A calibration platform was not developed, and orientation estimation was detected though manual movement of the segment, which led to large estimation errors due to an inefficiently generated calibration matrix, as well as limited

regression models used. In the following sections, a fully automated calibration procedure is developed, with a longer, 4-disk segment of a robot, and more investigation into different regression models is explored, including non-linear regression models to account for the non-linear relationship between light intensity and proximity to a surface, as is inherently characteristic of an optoelectronic sensor.

4.3.2 Tendon Actuated Robot integrating Optoelectronic Shape Sensing: Design Requirements and Fabrication

While previously mentioned, a common area where continuum robots are found is within MIS, where they perform some of the most complex procedures with extensive requirements. MIS encapsulates many different types of surgical procedures, each having different clinical requirements. The general areas where **requirements** are enforced include:

Size: typical trocar ports have diameters that range from 10-15 mm, depending on the surgical procedure

Accuracy: Commonly accepted tool tip errors range from 0.5-2° for orientation, with 1-2mm position.

Sampling rate: Commonly in the range of 5-20Hz.

Range: Orientation measurement in at least two orientations, with 90° bending range per segment of the robotic tool, although again, this is highly procedure dependent.

Biocompatibility: This considers material and signals used within the body to ensure safety.

As such, it can be seen that this novel optoelectronic shape sensing technique introduces potential for these requirements to be attained. For the purpose of preliminary investigation into the optoelectronic shape sensing technique, a larger multi-backbone tendon actuated robot is designed (Figure 4.6, Figure 4.7).

Figure 4.7 shows one segment of a flexible tendon actuated robot, that is made up of 4 disks, connected by a hemisphere ball joint. Three actuating tendons are routed along the segment, placed 120° apart, and three springs are fitted between each disk, which limits some of the torsion motion, while allowing bending the two other orientations. For the integrated shape sensing system, this comprises of three optoelectronic sensors fitted into each disk of the robotic segment, also positioned equidistantly at 120° apart (Figure 4.7). This proximity-intensity sensing is the basis of the sensing principle, and estimations of bending angle in each disk can be transformed into the overall tip orientation and position. The disks of the robotic

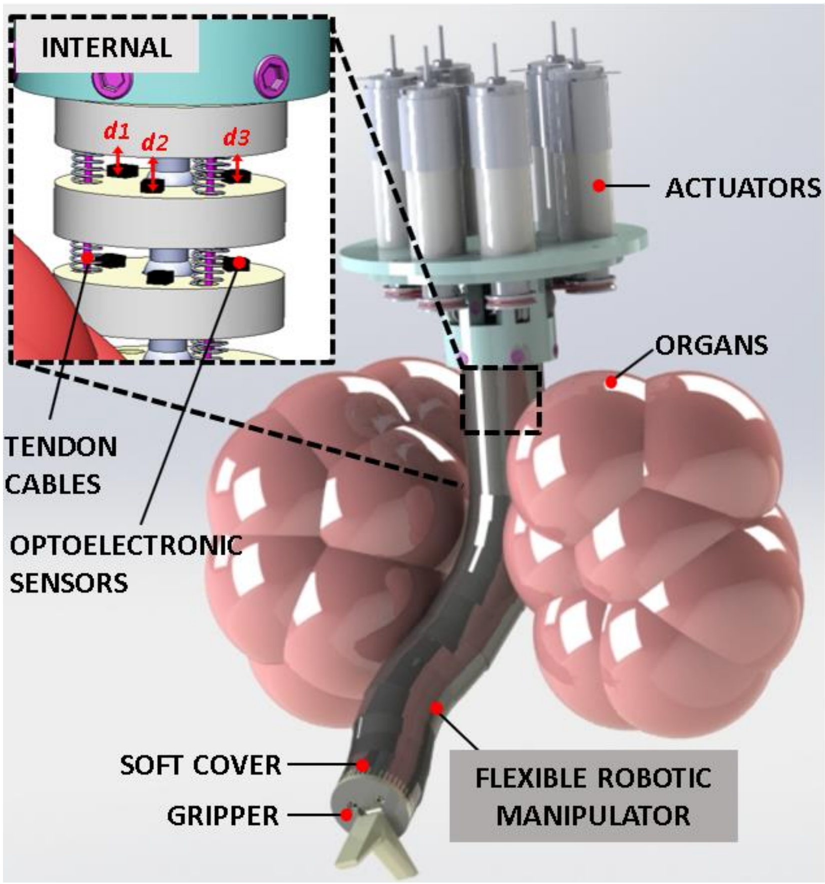

Figure 4.6: Concept image of MIS robotic tool with integrated proximity base optoelectronic shape sensing, utilising three optoelectronic sensors embedded in each disk, for measing continuum robot shape in two orientations [114]

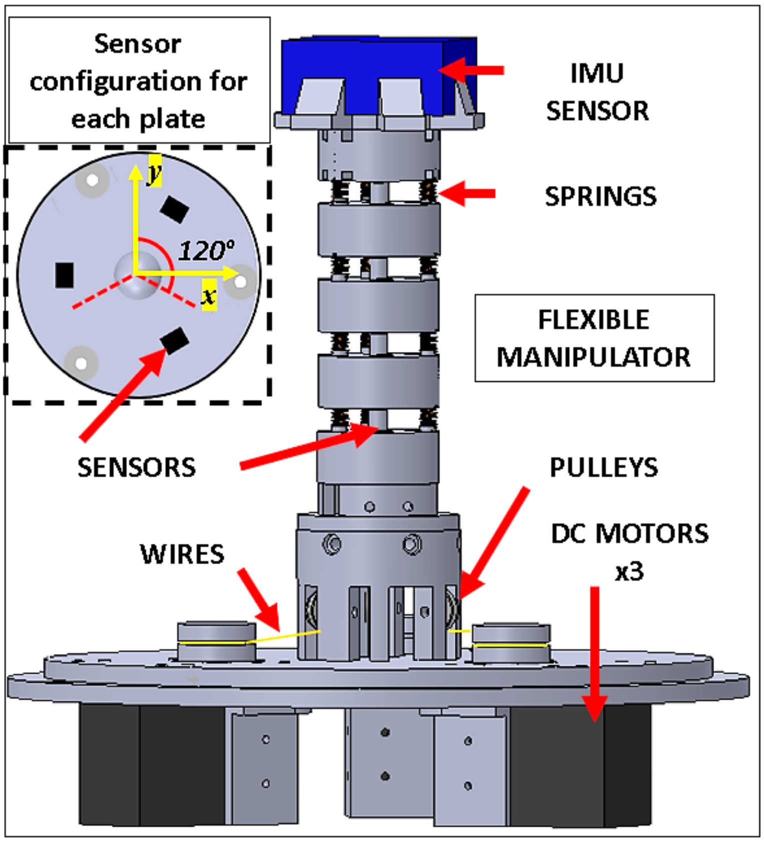

Figure 4.7: 3D design for the four-plate tendon driven robotic manipulator segment with integrated optoelectronic sensors within each of the plates. Tendons are driven using 3 DC motors. Tendon wires are wound over the pulleys, and around motor horns of each motor. An IMU sensor is mounted at the tip location, for ground truth data of tip orientation [114].

structure have a diameter of 32 mm, with an overall length of the segment at 140 mm, and due to this maximum bending angle is limited to 60°, although structural miniaturisation of the segment is possible in further developments. The optoelectronic sensor of choice is the QRE113 ON Semiconductor, with dimensions of 3.6 x 2.9 x 1.7 mm. Other than this, the general requirements can be followed, with careful consideration of safety features in future final prototypes, considering material used as well as features like power limitations for the sensor in that they fall within safety nets for use in the human body, as well as insurance of insulation. The aim is therefore to achieve high estimation of positional and orientation accuracy using the optoelectronic shape sensing that is integrated into the robotic segment, in two orientations.

The tendon actuated robot is constructed from four disks joined with hemisphere ball-socket joints. The three actuating tendons of the robotic segment (Figure 4.7) allow bending in two orientations, namely pitch (β) and roll (γ), and the fitted springs limit unwanted torsion (or yaw (α)) motion. The three tendons are actuated by three DC motors (Dynamixel XL430-W350, ROBOTIS, Seoul, Rep. of Korea) fitted into the bottom platform. The tendons are wound around the motor horns fitted onto the motors. The wires are then routed along the three triaxially positioned pulleys and up along channels in the disks of the robotic segment, where the pulleys transform the rotational motion of the motor to linear motion that pulls the segment into various bending angles. As pictured in Figure 4.7, the top disk houses an inertial measurement unit (IMU) (LPMS B, LP-RESEARCH Inc, Tokyo, Japan) sensor, which provides information on the orientation (pitch (β), roll (γ), and yaw(α)) of the tip of this segment. This is used in later calibration experiments, to give ground truth values of the overall orientation of the robotic segment. For the integration of the optoelectronics sensors, three sensors are placed triaxially in each disk of the robotic segment. This gives a total of 12 optoelectronic sensors, for 4 disks. The bottom side of each disk is used as a reflective surface for the sensors in the disk below it. The sensors are soldered to a piece of universal circuit board and attached (using glue) to a slider that fits into rectangular channels in the disks. These rectangular sliders that have a handle that allow vertical movement, that allow for testing of different conditions of initial proximity of the sensor to the upper reflective surface. These sliders can be fixed in place using small screws. These sliders are simply for experimentation purposes and are not intended to feature in the final prototype, as the initial positioning for the sensor will be known in final prototypes.

4.3.3 Tendon Actuated Robot integrating Optoelectronic Shape Sensing: Sensing Principle

As seen in Figures 4.6 and 4.7, the three optoelectronic sensors at each disk are placed at a radial distance of 10 mm. During bending of each disk of the manipulator, the distance ‘d’ between the sensors and surface of the upper disk are changed during motion, which is the distance travelled by the light reflected from the surface and detected by the PT of the sensor. These three detected signals are recorded as voltage values. Once sensors are calibrated, that is, the voltage data is passed through a regression algorithm, they can be used to map two orientation values. Once done for each unit, the estimated orientations can be used to build a kinematic transformation matrix to calculate the overall shape along the manipulator, as well as the overall orientation at the top of the segment and its position, which is crucial as this is where tools are fixed for the various flexible robotic applications.

4.3.4 Optoelectronic Shape Sensing Optimisation

To construct the prototype manipulator integrated with optoelectronic sensors, the placement and configuration of the sensors and the robot had to be established. As depicted in Figure 4.8, the distance between sensor and upper plate (d_{min} - d_{max}) during rotation must be within the sensing range and optimized for increased sensor sensitivity for maximised accuracy during calibration. This was done by using the initial sensor study carried out in chapter 3, which sought to understand the output characteristics of the sensor with linearly changing distance between the sensor and the flat reflector. This experiment was previously undertaken using a motorised linear guide used to vary proximities of a surface to the optoelectronic sensor. The graph in Figure 4.3 shows the results of multiple variation curves over 0 – 15mm displacement, where each time the phototransistor resistance value, R_2, was changed. Results showed that a curve with large output range was demonstrated by the R_2 = 15 kΩ configuration, while R_1 was selected at 150 Ω, which corresponded to a displacement range of 2-10 mm (d_{min} - d_{max}). This chosen curve displayed a large voltage range, which would enhance sensor sensitivity (V/°) and subsequent accuracy due to this increase in range, as it holds the

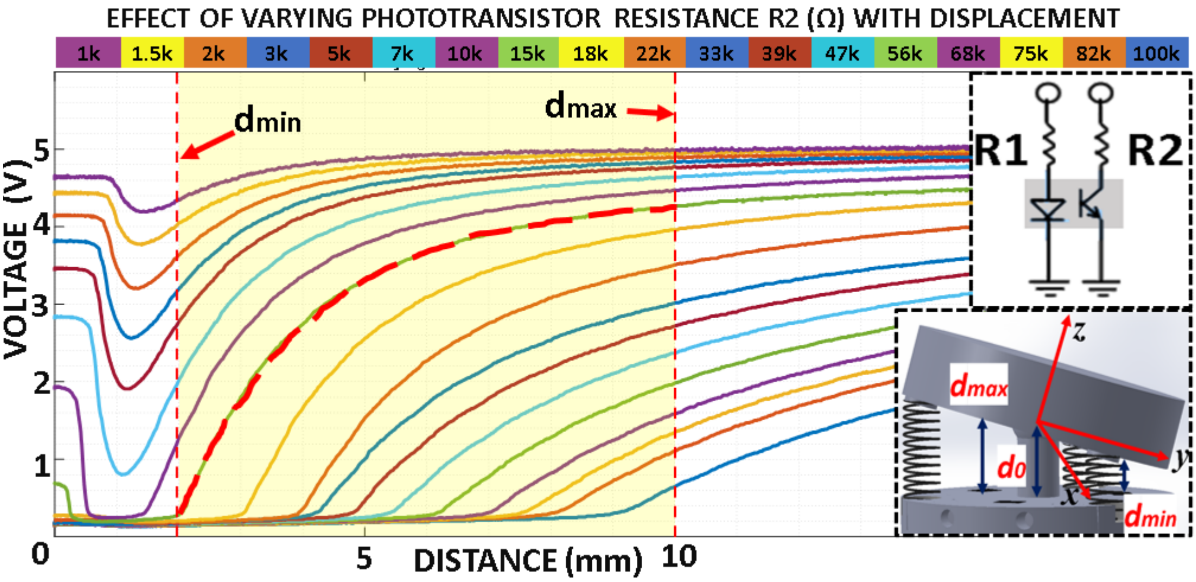

Figure 4.8: Left: Sensor output with varying phototransistor resistor values (R_2), to identify which offers a large voltage variation. Right: Once resistor response is chosen, optimised sensor proximity variation can be identified [114].

most linear characteristics of the curve, which again aids in minimising the effect on optical non-linearity tendencies and boosts resolution properties of the sensor when using this range. Thus, this range provided guidance for the dimensions of the disks of the robotic structure as well as guided the initial sensor placement, as the amount of bending of the disks would need to cause deflection away from the sensor that would remain withing the 2-10 mm boundary sensing range. If too much deflection was enabled, then the signal would saturate, or signal level would be too low if the reflector were too close to the sensor. By setting the initial distance between disks around the halfway point of this range, at 6.5 mm (d_o), then a ±15° was found to be an angular range that enables proximity change upon deflection in pitch and roll within this boundary range. In this way, as much of the sensor range was used as possible, and the shape sensing method could be fully explored in terms of its capabilities.

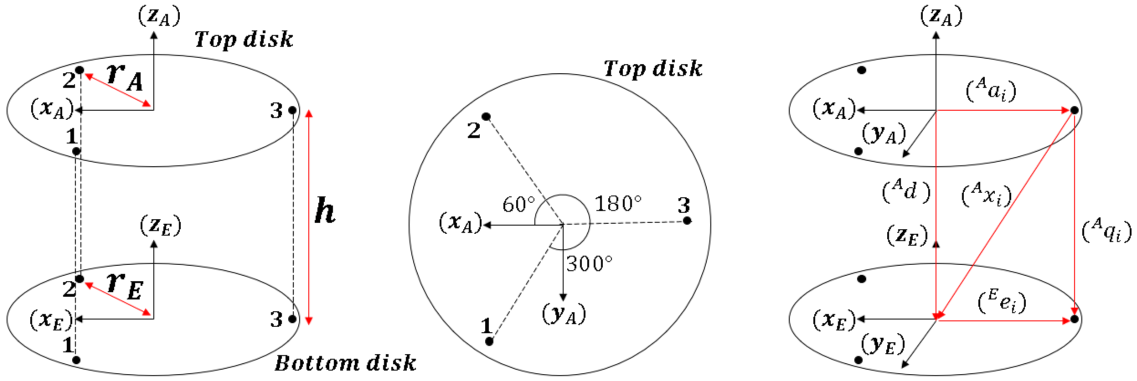

Figure 4.9: Diagram showing vector and node variables for the calculation of tendon lengths between disks of the tendon actuated robot, given an input disk orientation.

4.4 Robot Actuation

For the motor control, software was developed using Python to control the motion of the three DC motors (Dynamixel XL430-W250T), which in turn would pull the tendon cables to varying lengths. Clockwise turning of the motors would shorten the tendon cable length as it wound around the motor horn, while the reverse would restore length to the tendon cable. As seen in Figure 4.7, the tendon cable is able to wind around the motor horn into grooves spiralled onto the motor horn. In order to map a certain rotation angle of the motor to a known tendon cable length, a vector-based model was used. This allowed the calculation of three tendon cable lengths into orientation of the disk plate. The vector-based model was based on a model developed for a steward platform force/torque sensor [105]. Given an input target orientation of the top plate relative to the base, the model was used to calculate the required tendon lengths and then converted to three target motor positions. As the three motors move simultaneously, each pulls a tendon wire over the pulley for continuous motion while achieving the target orientations of the disks. The model is outlined below:

Vectors $({}^A a_i)$ and $({}^E e_i)$ are vectors pointing from the coordinate origin to the nodes $i = 1, 2, 3$ on their respective frames A and E. The angles between each node to both $\boldsymbol{x_A}$ and $\boldsymbol{x_E}$ axes on each disk can be described as $\sigma_i = [60°, 180°, 300°]$, as labelled in Figure 4.9. As such, vectors $({}^A a_i)$ and $({}^E e_i)$ can be defined as:

$$\left({}^{A}a_i\right) = \begin{bmatrix} r_A \cos\sigma_i \\ r_A \sin\sigma_i \\ 0 \end{bmatrix}, \left({}^{E}e_i\right) = \begin{bmatrix} r_E \cos\sigma_i \\ r_E \sin\sigma_i \\ 0 \end{bmatrix} \qquad (4.1)$$

Following this, it can be said that:

$${}^{A}x_i = {}^{A}d - {}^{A}a_i \qquad (4.2)$$

Next, a rotation matrix ${}^{A}_{E}R$, that transforms coordinate frame A to frame E is defined, which considers three orientation rotations in pitch, roll and yaw, such that:

$${}^{A}_{E}R = R_{\alpha\beta\gamma} =$$

$$\begin{bmatrix} \cos(\alpha)\cos(\beta) & \cos(\alpha)\sin(\beta)\sin(\gamma) - \sin(\alpha)\cos(\gamma) & \cos(\alpha)\sin(\beta)\cos(\gamma) + \sin(\alpha)\sin(\gamma) \\ \sin(\alpha)\cos(\beta) & sin(\alpha)\sin(\beta)\sin(\gamma) + \cos(\alpha)\cos(\gamma) & \sin(\alpha)\sin(\beta)\cos(\gamma) - \cos(\alpha)\sin(\gamma) \\ -\sin(\beta) & \cos(\beta)\sin(\gamma) & \cos(\beta)\cos(\gamma) \end{bmatrix}$$

(4.3)

Using this, we can define ${}^{E}e_i$ with respect to frame A as:

$${}^{A}e_i = {}^{A}_{E}R\,{}^{E}e_i \quad (4.4)$$

Using this, and the fact that

$${}^{A}x_i = {}^{A}d - {}^{A}a_i \quad (4.5)$$

we can then define the vector between respective nodes between two disks as:

$${}^{A}q_i = {}^{A}x_i + {}^{A}e_i = \left({}^{A}d - {}^{A}a_i\right) + \left({}^{A}_{E}R\,{}^{E}e_i\right)$$

$$= \begin{bmatrix} x \\ y \\ z \end{bmatrix} - \begin{bmatrix} r_A \cos\sigma_i \\ r_A \sin\sigma_i \\ 0 \end{bmatrix} + {}^{A}_{E}R \begin{bmatrix} r_E \cos\sigma_i \\ r_E \sin\sigma_i \\ 0 \end{bmatrix}$$

$$= \begin{bmatrix} x - r_A\cos(\sigma_i) + r_E\cos(\sigma_i)\cos(\alpha)\cos(\beta) + r_E\sin(\sigma_i)\cos(\alpha)\sin(\beta)\sin(\gamma) - r_E\sin(\sigma_i)\sin(\alpha)\cos(\gamma) \\ y - r_A\sin(\sigma_i) + r_E\cos(\sigma_i)\sin(\alpha)\cos(\beta) + r_E\sin(\sigma_i)\sin(\alpha)\sin(\beta)\sin(\gamma) + r_E\sin(\sigma_i)\cos(\alpha)\cos(\gamma) \\ z - r_E\cos(\sigma_i)\sin(\beta) + r_E\sin(\sigma_i)\cos(\beta)\sin(\gamma) \end{bmatrix}$$

$$= \begin{bmatrix} q_{xi} \\ q_{yi} \\ q_{zi} \end{bmatrix} \qquad (4.6)$$

$$l_i = \sqrt{q_{xi}{}^2 + q_{yi}{}^2 + q_{zi}{}^2} \qquad (4.7)$$

By finding the magnitude of ${}^{A}q_i$, the length of the tendon (l_i) between nodes can be know, and is a function of pitch, roll and yaw orientations. As twist is limited by the springs in the robotic structure and is not an actuatable degree of freedom, this variable is set to zero. This equation is entered into the python software, and where the constant variables are set. The input is given as pitch and roll target orientations, and this is converted to tendon lengths using the above equations. This length is the converted to a target motor position p which is a value between 0-4096, corresponding to 0-360° motor encoder position. This is done by calculating the difference in length, ∂l, since the last targeted position ($l_{i(t-1)}$) and converting this to a motor horn angle rotation $\partial\theta$ which would shorten the tendon wire by ∂l. This is calculated for each of the three tendons ($i = 1,2,3$).

$$\partial l_i = l_i - l_{i(t-1)} \tag{4.8}$$

$$\partial\theta_i = \partial l_i \cdot 360/2r\pi \tag{4.9}$$

$$p_i = \partial\theta_i \cdot \left(\frac{4096}{360}\right) + p_{i(t-1)} \tag{4.10}$$

For continuous motion, this value p is constantly updated for each node (tendon), to each of the three motors simultaneously, to achieve required pitch and roll motions.

4.5 Software Design for tendon actuated robot control

Next, a software platform needed to be designed, that was able to record and save multiple streams of data, display the data, as well as transfer and receive motor control commands. To do this, Python was chosen as a suitable language upon which to build the software, as it allowed simple integration of different devices, along with fast serial communication, for real-time two-way communication and display of data. The map in Figure 4.10 shows the architecture of the software interface, with its features and functions. The software interface was required to:

- Read multiple sensor analogue voltage data simultaneously over USB-serial interface with an Arduino Uno Micro-controller board.
- Simultaneously send motor position targets to three actuation motors, while reading the actual motor position from the encoder via USB-U2D2 converter device for TTL serial communication.
- Read three orientation angles from an IMU sensor over a Bluetooth connection.
- Provide a graphical interface for user input for motor commands.
- Provide a graphical interface for user control over file saving of data.
- Display motor position, sensor readings, and IMU readings with real-time graphics.

To incorporate all these functions, thread libraries were utilised to allow multiple task streams to run simultaneously. Three separate threads were created, one to write and read motor encoder data, one to read multiple optoelectronic sensor data over serial connection, and the third was to read in orientation angle data over a maintained Bluetooth connection. These three tasks could run concurrently without causing lag, allowing update of the most current data for real-time performance. As such, these threads run alongside the main thread, which updates graphical data with the most up to date data field. The graphs are updated at a rate of around 50ms, although the background streaming of data is much faster, at a rate of around 5-10 ms, which is around 100-200 samples per second (Hz). All streamed data is stored in small size buffers – arrays limited to 90 data points, so that only the most updated data is on hand, while old data is discarded. All streamed data is collected from the buffers during the running of experiments at a given time point, so that the multiple streams of data are time stamped synchronously. This data is saved into an excel file upon completion of a certain experiment or generated motion pattern. For the real-time graphical displays, the 'Matplotlib' library is used, along with its animation features. For serial communication with the ADC and Arduino devices for reading the optoelectronic sensor voltages, the 'serial' library was installed and imported into the software. Similar library was imported, 'dynamixel_sdk', which allowed specialised communication with the ROBOTIS Dynamixel DC motors, allowing the use of specific functions for accessing the control table of the motors, as well as writing and reading encoder data from three motors synchronously. Lastly, the 'OpenZen' library was used, which allowed direct communication with LMPS Bluetooth IMU device, to read in pitch, roll and yaw angles, from the IMU sensor.

Figure 4.11 shows the GUI of the software. On the left, 'sliders' were designed to allow finetuning of the tendon tension before starting any motion procedure. For this to work, the motor encoder positions are read upon running of the software and this position is updated on the slider. As the user slides the dial along different values, this is given as input to the respective motor as a target position. Once reached, the new read motor position is displayed.

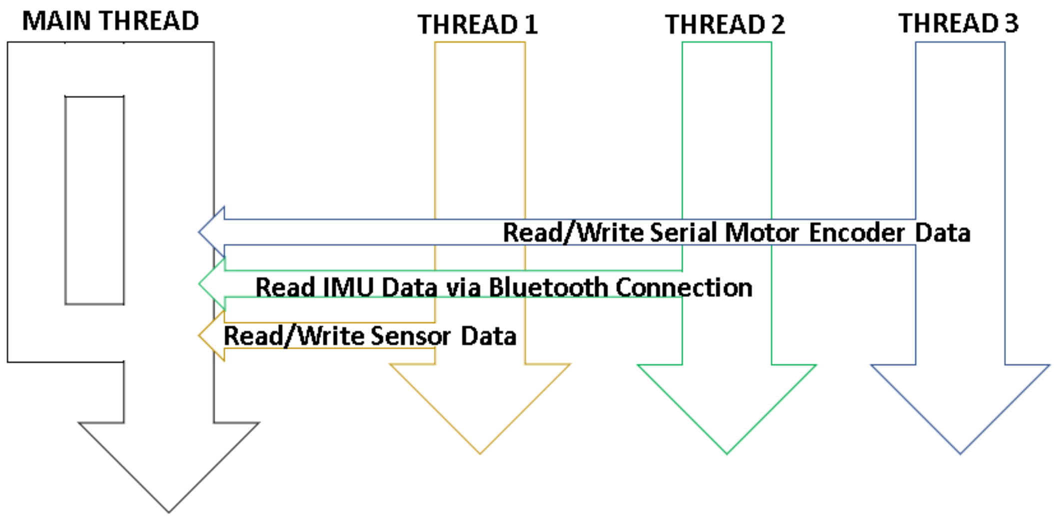

Figure 4.10: Schematic of the workings of the graphic user interface (GUI) software developed in python to control multiple device reading/writing and data display in real-time, using threading of multiple functions to fun simultaneously.

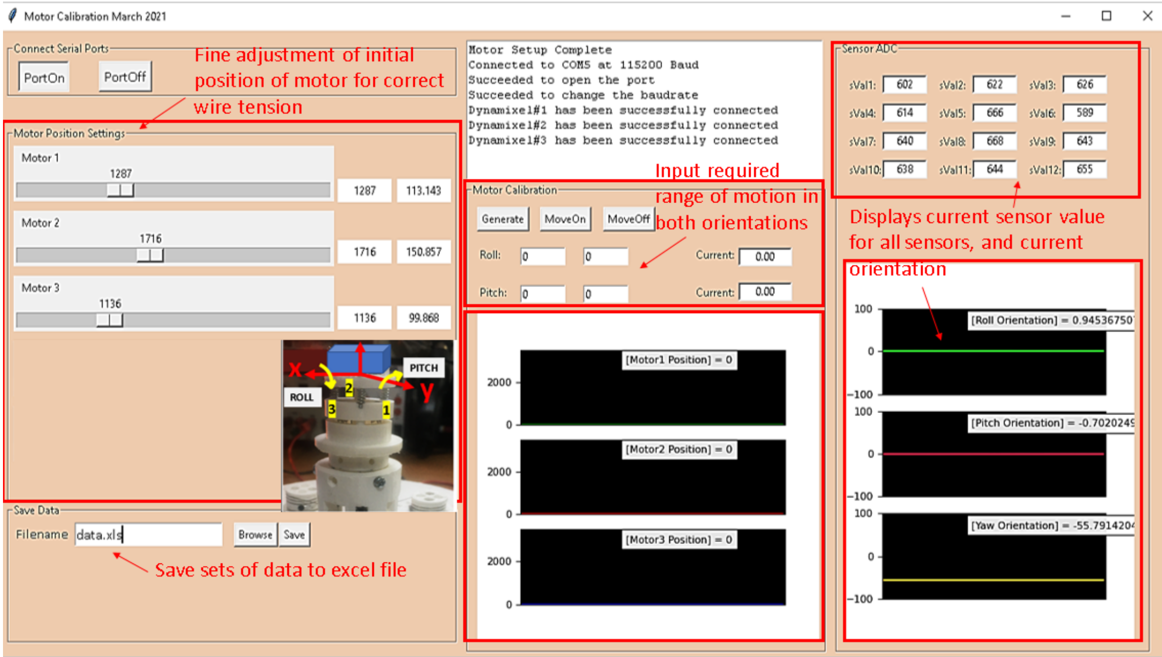

Figure 4.11: Screenshot of developed graphical user interface using python, with multiple graphical windows showing real time data streams display, graphical displays, motor position adjustment slider, file saving, status updates, as well as motion pattern generation.

For generating more complex patterns, the user inputs an angle range for both pitch and roll for the disk orientation. This generates a set of target positions in steps of 0. 09°.While running, the slider function is disabled, until the motion is completed. As such, this multipurpose GUI allows tracking of multiple variables and allows completion of calibration experiments to be described in subsequent sections in this chapter.

4.6 Methodology & Experiment Design

Before testing calibration for the integrated sensors using the full constructed tendon actuated robotic segment shown in Figure 4.12a, initial optimisation experiments were carried out. For this, the tendon robot was scaled back to just one base disk with an upper disk for surface reflectance (Figure 4.13), and the process for this is described in section 4.6.1. Further experiments described in sections 4.6.2, consist of the methodology for the full calibration of the four-disk robotic segment. These both use the same base platform housing the three motors with the pully tendon system. The platform was designed using CAD software (SolidWorks) and 3D printed using white PLA (Polylactic Acid) plastic. The 12 sensors were connected to a design circuit board, which consisted of all the resistors R_1 and R_2 set at 150 Ω and 15 kΩ respectively. The sensors were connected to a National Instruments USB-6501 DAQ device to reading of ADC signals from the sensors via USB serial connection. The IMU, as previously mentioned, was connected via Bluetooth, while a USB connection between the U2D2 device and the motors allowed serial communication, with an external power supply used to power 12V to the three motors.

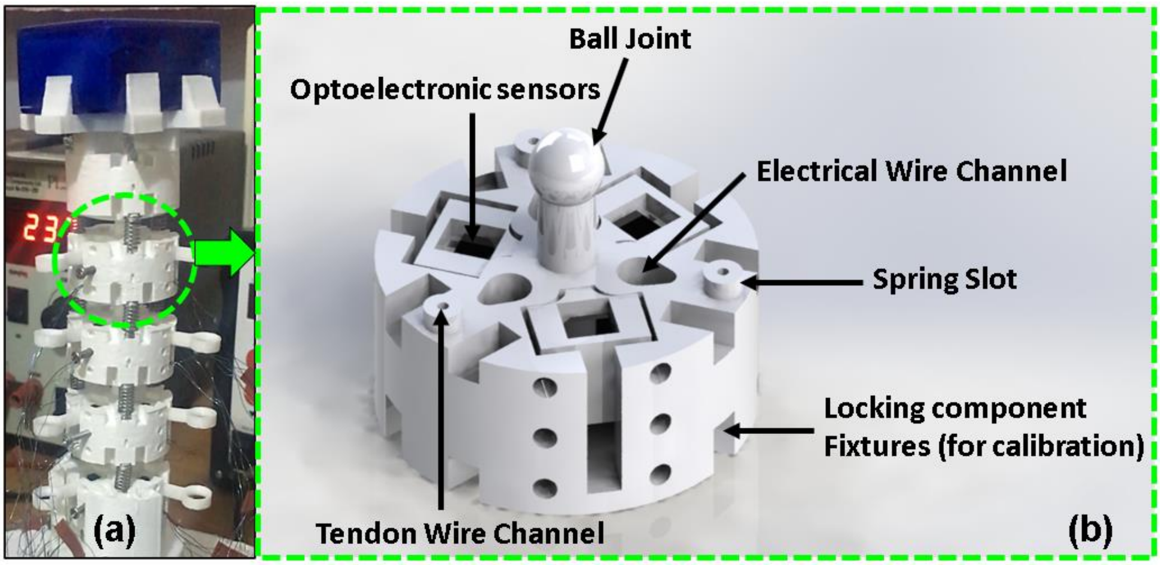

Figure 4.12: (a) Image of 4-disk tendon actuated robot with integrated optoelectronic sensors. (b) Inner working of the sensor placement within each disk [114].

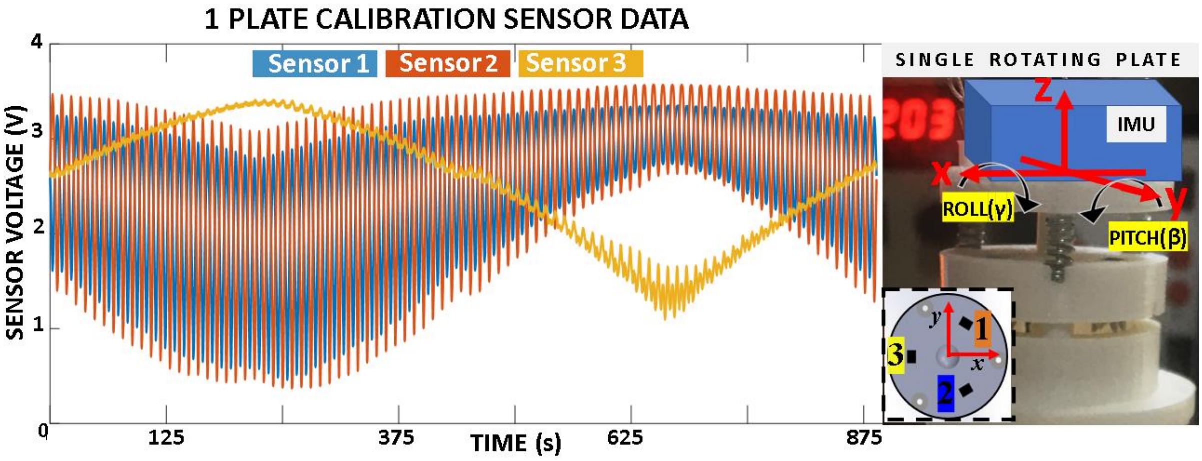

Figure 4.13: Graph (left) - Full sensor data (three optoelectronic sensors) recorded during calibration motion of one disk (right), with IMU fixed on top of disk to recorded ground truth orientation values (pitch and roll) [114].

4.6.1 Single Unit Calibration

Once the design for the manipulator and sensor configuration was optimised, the next step was to test the calibration algorithm. Calibration here is defined as the process by which the set of three voltage readings from the three optoelectronic sensors fitted into each disk of the robotic structure, are used to estimate orientation of the disk. This is done by deriving a calibration matrix from both sensor data and ground truth data and using this to generate a calibration matrix of coefficients. These coefficients could then be multiplied by the sensor values to transform voltage readings into angle estimations in pitch and roll. This was first done using just one disk, as in Figure 4.13, using the tendon driven platform described prior.

The base disk was fixed while the upper disk, through programmed control by software, rotated over a full angular range between ±15° in both orientations, pitch, and roll simultaneously, in steps of 0.09° while the sensor data was recorded simultaneously. This provided a comprehensive set of optoelectronic sensor data that covered all combinations of pitch and roll within the range. The IMU mounted on top of the upper plate was used to measure actual angular data for pitch and roll to serve as ground truth data. Figure 4.8 shows all the sensor data collected for the three sensors over this motion pattern. For the calibration, this data was first passed through a linear regression model. This was done in MATLAB, using the set of sensor values with ground truth data of the IMU sensor. With the improved and automated calibration technique compared to [85], the aim was to compare previous linear regression results to the current results to validate that the calibration method has indeed been cause for an improvement in orientation estimation accuracy. While linearity as a sensor property is desirable in terms of stability, it was evident that the sensor variation curves of output voltage vs displacement in Figure 4.8 were not completely linear. For this reason, a nonlinear regression model was also used. Shown in the linear model below, in Eq. (4.11), pitch and roll (β and γ) are calculated using a set of three coefficients per orientation, of matrix k, multiplied by the set of sensor values (v_1, v_2, v_3). Eq. (4.12) shows the nonlinear model, where a series of 16 coefficients per orientation are multiplied by the model to estimate β^i and γ^i , for each plate (i). Results are shown in Figure 4.7 comparing the two regression models.

$$\begin{bmatrix} k_{11}^i & k_{12}^i & k_{13}^i \\ k_{21}^i & k_{22}^i & k_{23}^i \end{bmatrix} \begin{bmatrix} v_1^i \\ v_2^i \\ v_3^i \end{bmatrix} = \begin{bmatrix} \beta^i \\ \gamma^i \end{bmatrix} \qquad \textbf{(4.11)}$$

$$i = 1,2,3,4$$

$$K_1^i(v_1, v_2, v_3) = k_1^i v_1^i + k_2^i v_2^i + k_3^i v_3^i$$

$$K_2^i(v_1, v_2, v_3) = k_4^i v_1^{i^2} + k_5^i v_2^{i^2} + k_6^i v_3^{i^2} + k_7^i v_1^i v_2^i + k_8^i v_1^i v_3^i + k_9^i v_3^i v_2^i$$

$$K_3^i(v_1, v_2, v_3) = k_{10}^i v_1^i v_2^{i^2} + k_{11}^i v_2^i v_1^{i^2} + k_{12}^i v_1^i v_3^{i^2} + k_{13}^i v_3^i v_1^{i^2} + k_{14}^i v_3^i v_2^{i^2} + k_{15}^i v_2^i v_3^{i^2} + k_{16}^i v_1^{i^2} v_2^{i^2} v_3^{i^2}$$

$$i = 1,2,3,4$$

$$\mathbf{(4.12)}$$

4.6.2 Four Unit Calibration

This calibration process was repeated for each disk in the 4-disk robotic manipulator segment, and each set of sensors within each disk had to be calibrated separately. This was done using the set-up described in Figure 4.14. In this instance, for the calibration of a disk, all other disks were fixed using interlocking components that prevented motion through compression or extension of a unit when the tendons would be pulled. In this way, all but one disk was allowed to move, while others remained fixed. In the same manner to the single plate calibration

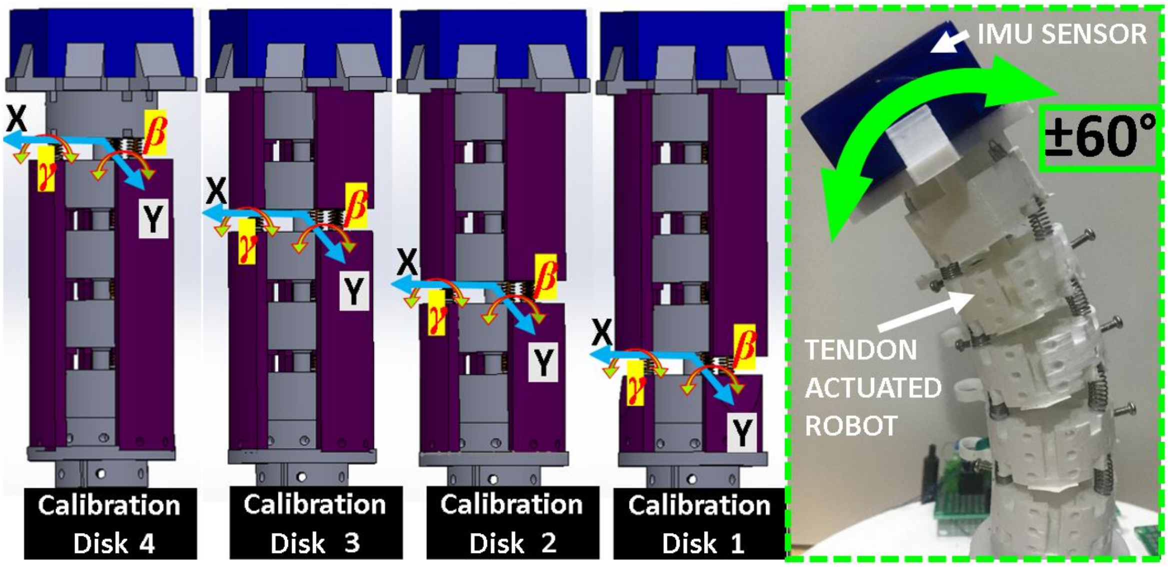

Figure 4.14: (Left) Multi-disk calibration method, by fixing sets of disks, using rigid frames (purple) to allow only one disk to bend when full robot segment is actuated, to collect all sensor data during this motion [114]. (Right) Once the calibration matrix is generated for all disks, the segment if freely actuated to full bending range (±60°) for final validation tests. During this motion, sensor data is recorded and used to estimate tip orientation using the calibration matrices and compared to orientation given by IMU sensor mounted at the tip location.

process in the previous section, a motion pattern would be generated by the control software to set the disk to move over the full angular range of ± 15° in both pitch and roll orientations, while the sensor voltages were recorded. Again, an IMU was mounted above the top plate, to record all orientation values through the motion as the ground truth data. As all other disks were fixed, this meant that the imu unit was always parallel to the disk undergoing motion, and as such provided ground truth values for that disk undergoing calibration data collection. This is repeated for each plate. The data for each disk was similarly passed through linear and non-linear regression models to calculate the coefficients as in Equations (4.11) - (4.12) for the generation of the calibration matrix. Next, for the validation of the calibration results, the locking components were removed from the segment, so as to allow the full robotic manipulator segment to move freely under changes in tendon lengths. The segment was set by the software to oscillate between a range of angles, up to maximum range of ±60° in both pitch and roll orientations, that is, a maximum of ± 15° for each disk, while sensor data from all 12 sensor was recorded, as well as the IMU sensor data. Coefficients belonging to each set of disks were used to estimate pitch and roll of that plate though multiplying the coefficients by their sets of voltages in each disk. Each of the estimated pitch and roll angles are consecutively summed to give the final orientation of the end plate on which the IMU sensor was fixed. In this way, the final orientation estimation was able to be compared to the angles given by the imu sensor, as a means of validation of the orientation estimation and this validation for use of this technique as a shape sensor. Results are shown in Figures 4.15-18, where the estimated orientations are compared against the real orientation data collected from the IMU sensor.

4.7 Results & Analysis

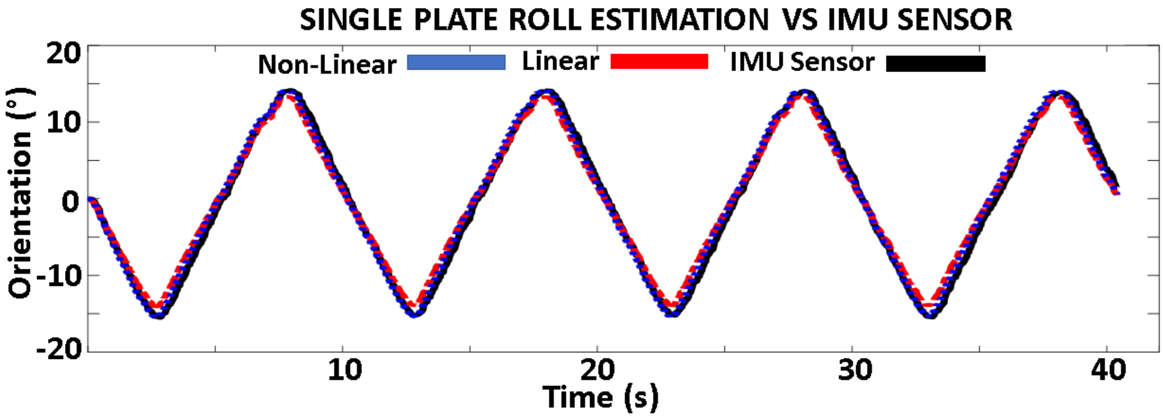

Figure 4.15: Data for single disk configuration, showing comparison of estimate of tip roll orientation during motion of the pair of disks between ±15°, using both linear (red) and non-linear (blue) regression-based calibration coefficients, and against the ground truth orientation data given by the IMU (black) [114].

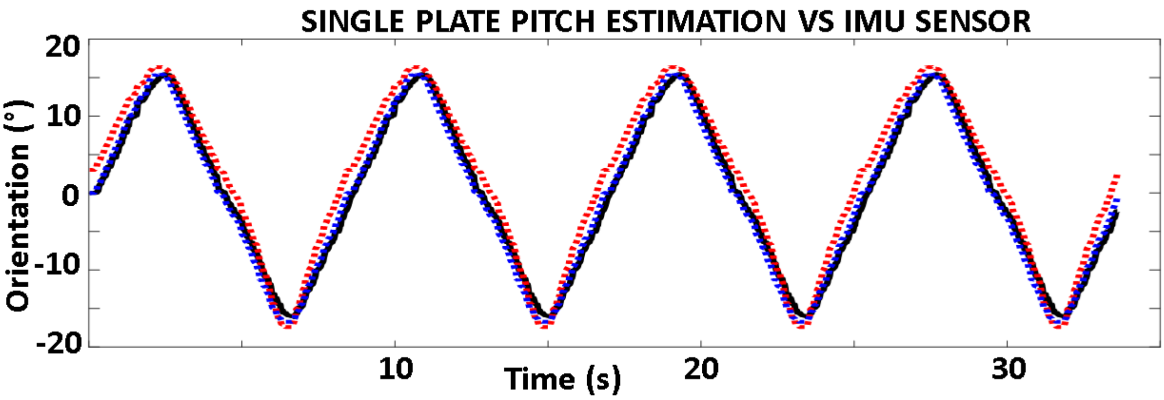

Figure 4.16: Data for single disk configuration, showing comparison of estimate of tip pitch orientation during motion of the pair of disks between ±15°, using both linear (red) and non-linear (blue) regression-based calibration coefficients, and against the ground truth orientation data given by the IMU (black) [114].

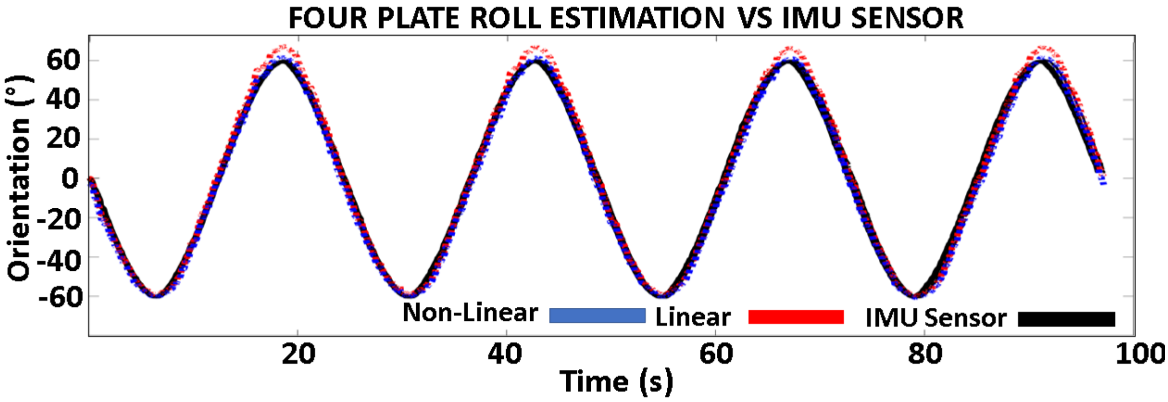

Figure 4.17: Data for four-disk configuration, showing comparison of estimate of tip roll orientation during motion of the full robot segment between ±60°, using both linear (red) and non-linear (blue) regression-based calibration coefficients, and against the ground truth orientation data given by the IMU (black) [114].

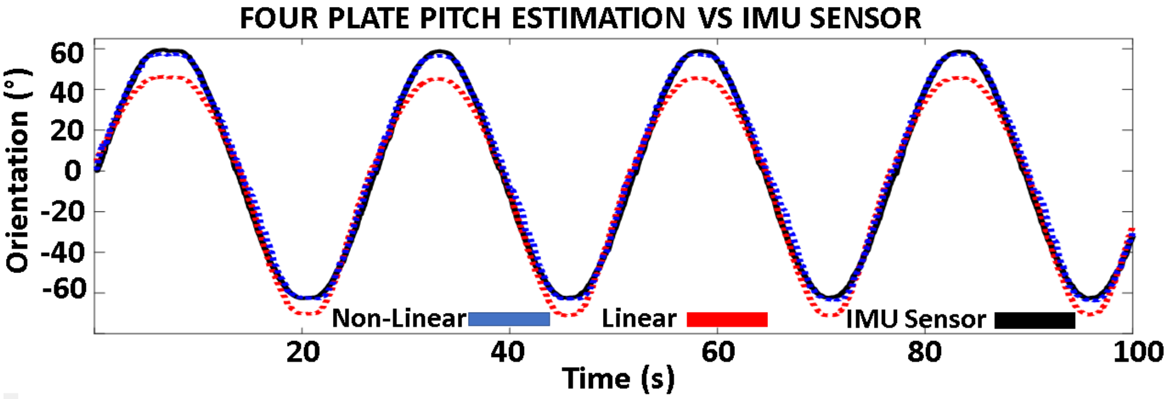

Figure 4.18: Data for four-disk configuration, showing comparison of estimate of tip roll orientation during motion of the full robot segment between ±60°, using both linear (red) and non-linear (blue) regression-based calibration coefficients, and against the ground truth orientation data given by the IMU (black) [114].

TABLE 4.1: SINGLE PLATE CALIBRATION RESULTS

Regression method	Orientation (±15°)	RMSE (°)	% Error
Linear	Pitch	2.45	4.57
	Roll	1.14	2.92
Non-Linear	Pitch	0.85	0.69
	Roll	0.76	0.46

TABLE 4.2: FOUR PLATE CALIBRATION RESULTS

Regression method	Orientation (±60°)	RMSE (°)	% Error
Linear	Pitch	7.12	8.73
	Roll	3.44	4.41
Non-Linear	Pitch	3.23	1.31
	Roll	2.52	1.11

In looking at the results for both the single and four plate calibration validation experiments, the sensing principle using optoelectronic sensors can successfully be utilized for estimating orientation in a flexible robotic structure for shape sensing. In reference to Table 4.1, and Figure 4.15-18, it is seen that a nonlinear regression model used to estimate orientation was more accurate than the linear regression model, with maximum percentage errors reducing from 4.57% to 0.69%. A similar trend is seen considering four plates where orientations were tested to the maximum angular range of ±60°. Here the maximum percentage error seen for linear regression was 8.73% compared to only 1.31% for nonlinear regression estimations (Table 4.2). As previously mentioned, the non-linear nature of the sensor with increasing distance is cause for this trend. Although, when comparing to [85], we can see much improved accuracy with regards to the linear regression model, where maximum percentage errors fell from a reported 39.4% to 4.57% shown here for a single plate configuration, and from 33.8% to 8.73%, from a three plate to a four-plate configuration. This indicates that despite this weak regression model, the refined automated calibration platform allowed for significant increase in accuracy for shape sensing. An observation from the results is the increase in error when transforming from the single to four-plate configuration of the manipulator with both regression models. There may be many reasons for this. For example, the 3D printed PLA material used to construct the structure may have suffered some deformation during larger tensions required for the actuation of the four-plate configuration. This may have caused some unpredicted motion, leading to some unforeseen errors. PLA 3D printing resolution error may have also caused some small clearance between the joints of the plates which could have affected the motion. There is potential in future prototypes to perhaps use alternative materials with more rigidity such as aluminium or stainless steel, which may be used to withstand excess tension and allow for a more precise fit. While fitted springs, alongside programmed motion control was used to limit yaw motion, another potential cause for errors may have been summations of small twist motions in each consecutive plate, causing an overall larger tip error, and this is a point of investigation within further prototypes. There perhaps is a possibility that further estimation of this third yaw orientation using another sensor and incorporating additional geometrical design of the reflective surface for light modulation in this direction, with aim to boost the resulting shape sensing estimation accuracy. As this sensing technique is based on the modulation of light intensity, a soft material cover for the robotic manipulator to block external light signals should be included to exclude any ambient level light for better consistency.

4.8 Conclusion

Upon evaluating the results at this stage, some points of improvement were identified for consideration in the design of the next prototype. The potential causes of error during calibration are to be addressed, primarily friction issues within the ball/socket joint due to deformation and wearing of the PLA 3D printed ball joint, which may have hindered smooth motion and affected the quality of the calibration data. Further consideration was also needed in the circuit design, as electrical wiring had become excessive with multiple sensors, and some heating effects were detected. As such, the subsequent prototype would require further miniaturised robotic structure, for targeted applications in MIS, as well as structural and design improvements mentioned. As mentioned in the design requirements, commercial trocar ports for multi-backbone continuum robots for surgery are found in the range of 10-15mm. With the shape sensing validated to maximum RMSE of 3.23° with non-linear fitting, these results at this stage show promising potential for applications in MIS with modification to target further accuracy. To do this, one aspect is to use smaller sensors, such as the NJL5901R-2 (1 x 1.4 x 0.6 mm, New Japan Radio), as to reduce size as well as effect of any ambient light despite use of a cover. To simplify the design, the sensors will be integrated into a flexible circuit, and the use of ADCs as well as power switching circuits would cut down on electrical wiring and massively cut down on maximum current use, as switching of power to sensors would allow one or two sensors to be powered at a time. As such, an improved flexible robotic manipulator can feasibly be targeted, with increased plate numbers to extend workspace with reduced disk size. An alternative approach in order to target more linear regions of the sensor variation curves with reduced rotation per plate can theoretically be achieved through changing the reflector shape, hence potentially increase in estimation accuracy, and this is the topic outlined in the next chapter.

It is also noteworthy to mention the use of an IMU sensor as ground truth, as it is inevitable that this sensor itself will have some error. However, the documentation for the IMU sensor utilised (LPMS B, LP-RESEARCH Inc, Tokyo, Japan) states that the accuracy for the sensor is: < 0. 5°(static), < 2° RMS (dynamic). The IMU sensor firmware also includes autocalibration features, and accounts for noisy magnetic fields [9-Axis Bluetooth IMU LPMS-B2 Series - LP-RESEARCH]. Despite this, there is still some potential for error in using this type of sensor as ground truth. At the current stage, the IMU sensor was used as ground truth to determine the feasibility of the optoelectronic shape sensor integrated into a tendon actuated robot, and to allow comparison to previous stages of development of optoelectronic shape sensors. However, in future developments, it would be more ideal to calibrate the shape sensor system using a vision-based marker tracking system, for more reliable accuracy.

Overall, there is great potential for further development of this shape sensor for MIS tools, and steps for improvement will be outlined in the next chapter including using curved reflector shapes, as well as implementing the improvements outlined in this section.

CHAPTER 5: NOVEL ONE-AXIS JOINT ANGLE SENSOR AND TWO-AXIS TENDON ACTUATED ROBOT INTEGRATING OPTOELECTRONIC SHAPE SENSING WITH A CURVED REFLECTORS

5.1 Introduction

Upon undertaking a study into the one-dimensional behaviour of an optoelectronic joint angle sensor and applying these concepts in a two-axis tendon continuum robot with integrated optoelectronic shape sensing in Chapter 4, much could be said on the performance of the sensors in these areas. As previously mentioned at the end of Chapter 4, some sensor performance improvements could be identified that could help to improve accuracy of the shape sensor during application. Alongside this, in the results of the hinged joint angle sensor in Chapter 4, it could also be seen that certain sensor output characteristics against joint angle could also be improved. For example, considering this one-axis joint angle sensor in section 4.2, which uses a flat 'hinge' reflector, the results showed that optical sensors for joint estimation had areas for improvement – namely:

(1) sensor measurement range

(2) sensor sensitivity

To address these areas, the idea is that this can be targeted by adapting the shape of the reflector this time, rather than the sensor properties and positioning. This chapter will introduce designs for another joint angle sensor using optoelectronics. While maintaining the properties of an ideal joint angle sensor as described in the review of 1DoF joint sensors in Chapter 4, such as miniaturisation and direct joint integration, the further listed features will be targeted through the new designs. To target *(1)* sensor measurement range and *(2)* sensor sensitivity improvement, a curved convex-like reflector will be used in the design of this new joint angle sensor (Figure 5.1). These concepts are novel, in that they target characteristic sensor properties without any physical changes to the sensor. This is an ideal concept, as it allows flexibility in adapting designs to different applications and scales, and the ideas can be translated to two-dimensional shape sensing, as will be done in further stages in this chapter, which will present the new design of a tendon actuating robot integrating optoelectronic shape sensing, this time using curved reflecting components to achieve improved sensing capabilities. Targeting these limitations will allow us to break through and expand the use of such sensors in many more applications.

5.2 One-axis Optoelectronic Joint Angle Sensor using a Curved Reflector

The proposed optoelectronic joint sensor using a curved reflector aims to increase the sensor sensitivity and sensing range. This will be done through testing a range of reflective surfaces that vary in curvature, and the effect this has on the sensor output will be studied through experimental results as well as through mathematical modelling, using a light intensity model to estimate theoretical light intensity output.

5.2.1 Optoelectronic vs a Curved Reflector: Mathematical Light Intensity Model

The sensing principle for this curved reflector is based on the modulation of emitted and reflected light intensity. The previously evaluated light intensity model [106], in Chapter 3, is used to study the behaviour of the sensor under specific geometrical conditions. It is assumed that the light is emitted conically from the LED, following a Gaussian distribution. The intensity model is employed to estimate the sensor output by considering the light reflected from a surface that rotates at varying angles, denoted as φ. In the current construction of the sensor configuration, φ is set to zero because the sensor is positioned opposite the reflective surface, as shown in Figure 5.1. Despite the surface's curvature, we take the assumption that the area interacting with the reflected light is flat due to its relatively low curvature in comparison to the sensor size. The flux (ϕ_c) collected by the phototransistor (PT) can be calculated using Equation 3.3. This involves integrating the initial light intensity distribution within the boundaries of the LED and phototransistor structures over the conically formed projection on the projection plane. Here, h represents the varying distance between the sensor and the reflector surface, which changes as the joint rotates about a vertical axis. d denotes the LED diameter, θ represents the LED beam angle, and ε is the distance between the PT and LED. Finally, a^2 represents the conical beam width. To convert this flux into a theoretical voltage value, it is multiplied by a conversion factor k_v and the reflectance rate R, as shown in Equation 3.13 below.

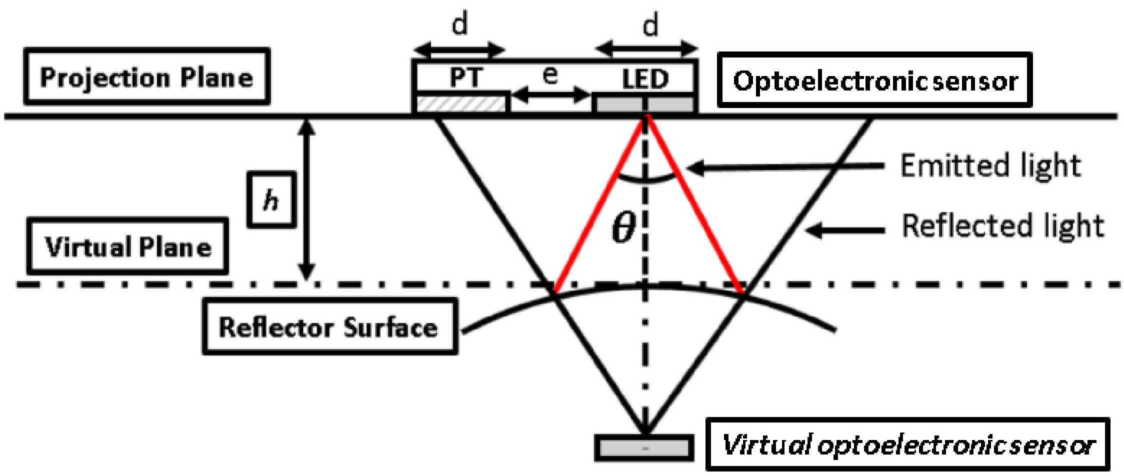

Figure 5.1: Light is emitted from the LED (d = 0.4mm) with beam angle (θ = 50°) onto a curved reflector. Modelling of a virtual LED source on a virtual plane allows finding of the path of the reflected light to the projection plane [137].

$$\phi_c = \int_{-\frac{3}{2}d-\varepsilon}^{-\frac{1}{2}d-\varepsilon} \int_{-\sqrt{\left(\frac{d}{2}\right)^2-(y-h\tan(\theta)+d+\varepsilon)^2}}^{\sqrt{\left(\frac{d}{2}\right)^2-(y-h\tan(\theta)+d+\varepsilon)^2}} I_0 e^{-2\left(\frac{x^2+y^2}{a^2}\right)} dydx \qquad (3.3)$$

$$V_{th} = \phi_c \cdot R \cdot k_v \qquad (3.13)$$

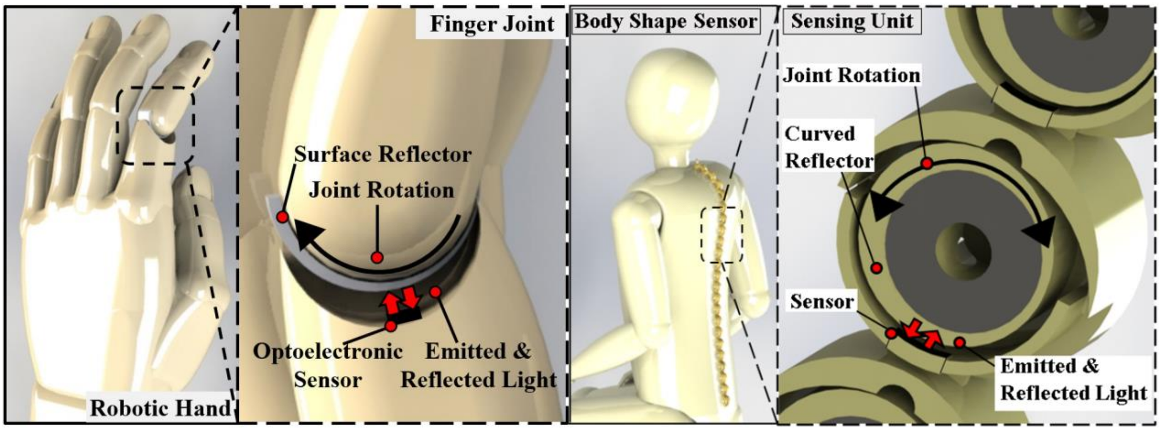

Figure 5.2: Concept images for the proposed optoelectronic joint angle sensor using a curved reflector, for example in robotic finger joints (left) [137], or planar body shape sensors (right) [138].

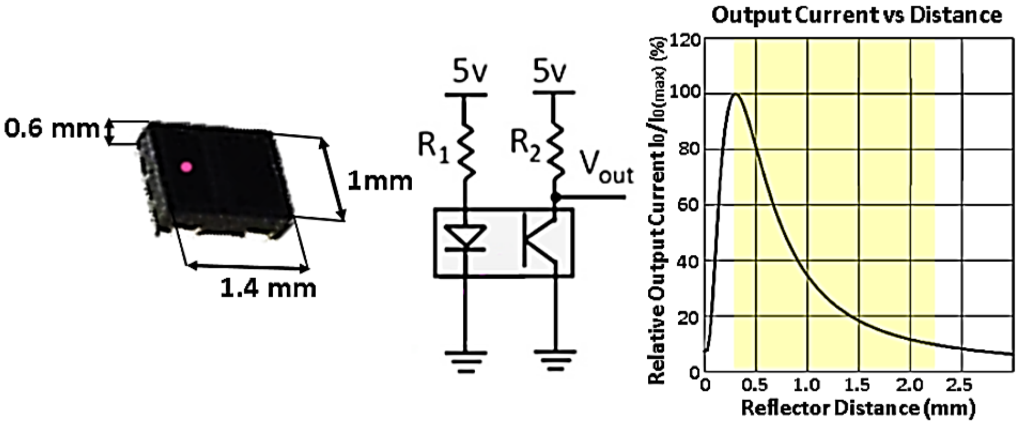

Figure 5.3: (Left) NJL5901R-2 optoelectronic sensor dimensions and circuit. LED resistance R_1 and PT resistance R_2 are set to 1 kΩ and 10 kΩ respectively. (Right) NJL5901R-2 datasheet graph shows sensor displacement vs relative output current, against an ideal (aluminium) reflector [137][94].

5.2.2 Optoelectronic Joint Angle Sensor Using a Curved Reflector: Design and Experiment

As previously described, a curved reflective surface was designed with the aim of achieving a larger sensing range compared to previous attempts that utilized flat reflective surfaces. A concept image for how this would work is shown in Figure 5.2, illustrating the placement of optoelectronic sensors coupled with a curved reflector into joints of a robotic hand, or a wearable body sensor. The graph in Figure 5.3 supplied by the datasheet of a new optoelectronic sensor (NJL5901R-2) shows the response with linear displacement to a reflective aluminium evaporation surface under ideal test conditions. This model of sensor is smaller, measuring (0.6 x 1.4 x 1mm), compared to the previous sensor model (QRE113).

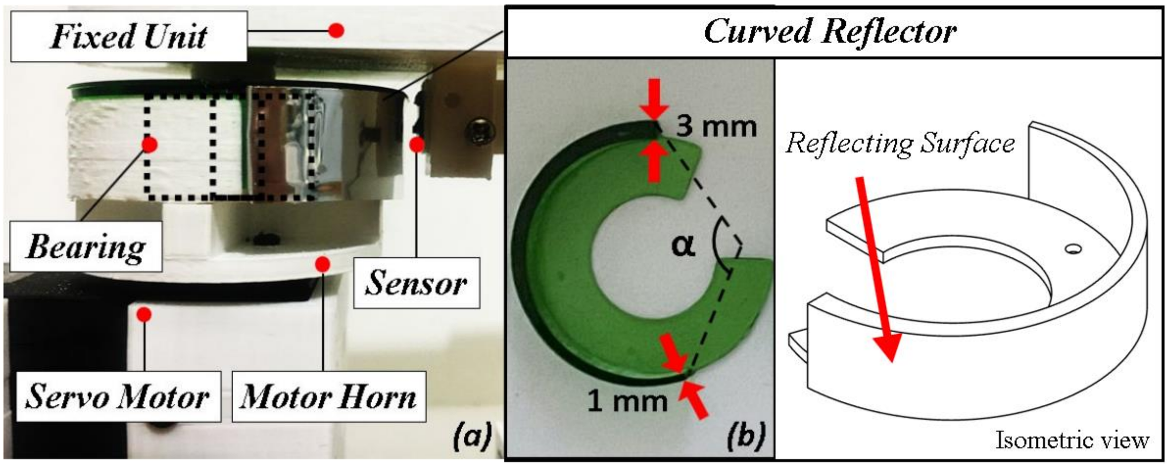

Figure 5.4: (a) Experimental platform – The curved reflector component is fixed onto the rotating motor horn that is attached to a DC servo motor. The optoelectronic sensor is mounted onto the fixed component that is rotationally coupled to the motor horn with a ball bearing (b) Curved reflector surface design parameter; while thickness from start to end of the reflecting surface changes from 1-3 mm, the area, or angle (α) over which this variation occurs differs between designs. Surface is covered in silver tape to for high reflectance, to achieve response seen in Figure 5.3 [137].

Based on this data, a usable sensor range can be selected. A generally linear range between 0.3 – 1 mm is seen, with a less sloped response beyond this distance as it plateaus. From this data, the 0.3-2.3 mm sensing range is used as the starting point for the design of the reflective curved surfaces, as highlighted in yellow colour. Apart from the size, and sensing range, this new optoelectronic sensor operates in the same way as the QRE113, and the characteristic behaviour studies in Chapter 3 can be applied here.

The fabricated curved reflector design is shown in Figure 5.4; this curved surface follows a circular and can be regarded as a convex surface. This is fixed to the experiment rig shown in the same image (5.4a). Here, the reflector is attached to a component that is screwed into the motor horn of a DC motor (Dynamixel, XL430-w250). The centre of the motor horn component has a bearing, where the shaft of the fixed component sits. The optoelectronic sensor is attached to this fixed component. Regarding the reflector, as can be seen in Figure 5.5b, starting on one end, the thickness of the curve is 3 mm, and this gradually decreases to a thickness of 1 mm, therefore reducing by 2 mm in total over a certain angle range (α) around the circular path, in order to coincide with the range selected from the data sheet (Figure 5.3). With this gradual change in curvature, an assumption is made as described in the model in section 5.2.1, that the point at which light reflects on the surface is taken to be flat.

To study the sensor response with varying reflective surfaces, the experimental setup was constructed to generate the joint motion, with the fixed component rotationally coupled to the motor using the bearing within the motor horn. On this fixed component, the optoelectronic sensor is mounted into place. The components were 3D printed using PLA (Polylactic acid) plastic, other than the interchangeable curved slopes to be tested, which were designed, and 3D printed using a high-resolution resin printer so that the surface finish was as smooth as possible. The curved edge of the surfaces were covered with reflective aluminium tape in order to maximise reflectance rate. These were screwed onto the motor horn component to move together with the motor. The sensor was wired to an Arduino Mega ADK board (5 V) and connected to the PC. The motor (12 V supply) was connected to a U2D2 communication device also connected to the PC.

Python software was used to synchronously interface the motor encoder position as it was commanded to rotate for a given angular range, along with the analogue sensor values. This data was recorded and stored through each of the experiments. With each curved surface that was tested, the thickness of the curved structure was varied by changing the angular range (α) over which the thickness ranged from 3-1 mm, as depicted in Figure 5.4. The initial disk tested had the thickness range descend over $\alpha = 200°$. Subsequent curved surfaces tested were over $\alpha = 180°$, 140°, 120° and 100°. These are labelled in Figure 5.5 as Surfaces 1-5. Figure 5.8 in the following section shows the results of each of the tested surfaces that essentially change in curvature, and the effect this has on the sensor output over an angular range of motion of the experimental joint, while also comparing to the theoretical output predicted by the light intensity model described prior in section , and this is discussed in the Discussion section.

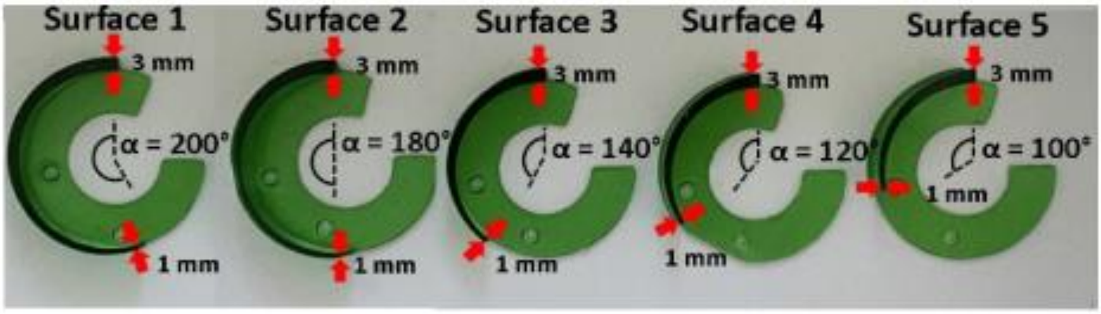

Figure 5.5: Bottom section view of the design of Surfaces (1-5) showing curvature change over range of α values [137].

Once each of the reflectors shown in Figure 5.5 of different curve parameters were tested under the single joint angle sensor experimental platform (Figure 5.4), a further set of experiments were undertaken with a multilink, chain-like, planar, multi-jointed structure. This prototype is shown in Figure 5.6, and is a rigid 4-link chain, with the integrated optoelectronic joint angle sensing system within each joint. This idea is based on the concept for a planar wearable curvature shape sensor, as is illustrated in Figure 5.2, that also illustrates the joint sensor principle. Each link comprised of the curved reflecting surface, with parameters chosen based on the results shown in Figure 5.8. Set over a range of 140°, the thickness of the reflector changes over a 2mm range, shown in Figure 5.7. This again, is in line with the sensor responsive range in reference to the sensor's technical data sheet, and so proximity between the sensor and the curve will increase as rotation ensues, resulting in a varying voltage signal. The prototype consists of 30 mm diameter disk joints, linked together using rotational bearings. The curvature-based surface reflector is designed as part of the rotational joint, with a 47mm distance between each link. The optoelectronic sensor is fixed within a channel along the joining link on a sensor mount that can slide along the link and allows optimisation of sensor placement. The joint link also consists of a bracket used to block some external ambient light source. Bearings are used at each joint to allow rotational motion between the units.

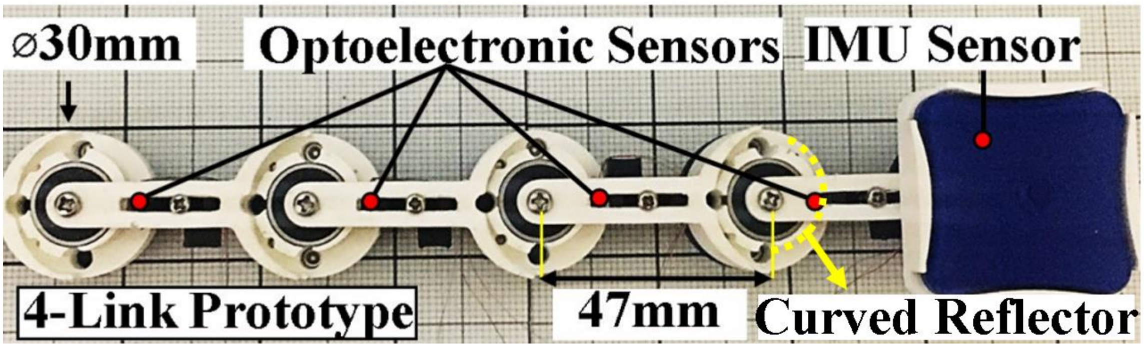

Figure 5.6: Fabricated 4 links chain structure, coupled using bearings for one degree of freedom planar motion. Each joint houses curvature based optoelectronic joint sensing. The IMU sensor is attached to the end of the chain, for measurement of orientation it this location [138].

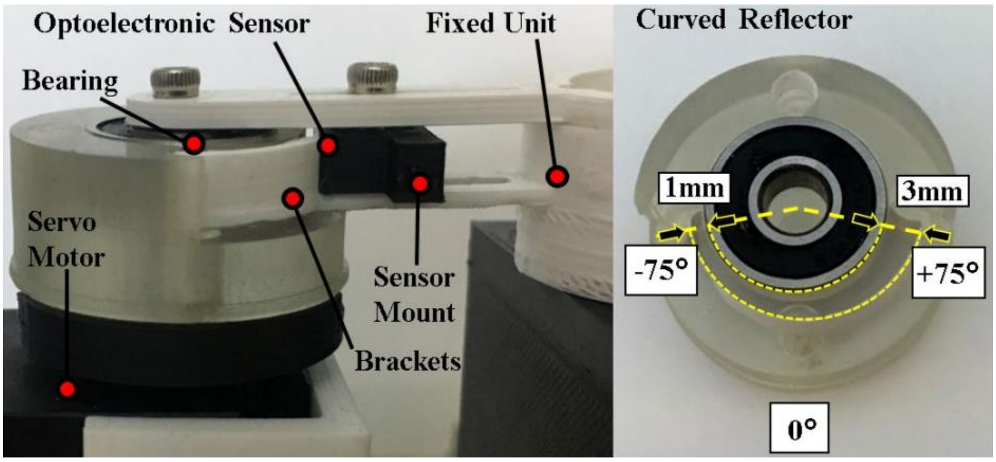

Figure 5.7: (Left) Experimental platform for carrying out calibration of each sensing joint in the four-link chain. Each rotating unit is attached to motor horn, with the optoelectronic sensor component mounted onto a sliding sensor mount component, on following fixed link. Each joint is rotated with a set angular range using the motor, and sensor data is recorded. This is used for calibration of each joint. (Right) Curved surface reflector parameters [138].

To calibrate each sensor, the testing set up as shown is Figure 5.7 was used, which is very much similar to the motor-based calibration used in Figure 5.4. Again, the DC Servo was used to generate rotational motion. Each optoelectronic sensor was calibrated individually by mounting the disk of one link to the motor horn, with the coupled link fixed onto an adjacent fixture. In this way, the sensor was fixed within the link, and the coupled unit was able to rotate with the motor. All components were also designed using CAD and 3D printed using PLA (Polylactic acid) plastic material. The curved surface reflector area was coloured white for higher reflectivity. The sensors were wired to an Arduino Mega ADK board (5V). The Dynamixel Motor was powered using a 12V supply and connected to a PC using a U2D2 communication USB device. Developed python interface software was used to synchronously send motor position commands and record analogue sensor data along with motor encoder position data. From this, angular range data was known. Hence, each sensor, and coupled link unit was fixed onto the testing rig, where the motor was rotated through a set angular range, while the sensor signal was recorded.

Using the motor encoder position as ground truth, a fifth order linear polynomial regression model was used to map the sensor values. Equation 5.1 shows this model for link angle estimation using the coefficients C1 to C5, multiplied by the sensor value v_i for that link. Results of this calibration are shown in the following section.

$$\theta_i = C_1 v_i^5 + C_2 v_i^4 + C_3 v_i^3 + C_4 v_i^2 + C_5 v_i + C_6 \qquad (5.1)$$

$$x_i = x_{i-1} + l_i \cos(\theta_i + \theta_{i-1}) \qquad (5.2)$$

$$y_i = y_{i-1} + l_i \sin(\theta_i + \theta_{i-1}) \qquad (5.3)$$

where $i = 1,2,3,4$

$$\theta_{\text{final}} = \theta_1 + \theta_2 + \theta_3 + \theta_4 \qquad (5.4)$$

Once all the sensors were calibrated, the next tests were used to evaluate the sensing performance. Here, a range of shapes were constructed using the chain of links of the prototype structure shown in Figure 5.6. An inertial measurement unit (IMU) (LPMS-B2, LP-Research, Tokyo, Japan) sensor was fixed to the end link, to read ground truth angular values of the final link, while all sensor data was simultaneously recorded. The sensor data along with the calibration coefficients were used to estimate the final link angle using a simple rigid link model. Equations (5.2) and (5.3) show link position coordinates x and y, using link length l and joint angle estimation θ for each link with the initial link grounded. Equation (5.4) describes the overall angle of the final link as a summation of each estimate. This was compared to the final angle value given by the IMU sensor. Results for this are shown in the following section.

5.2.3 Results & Analysis

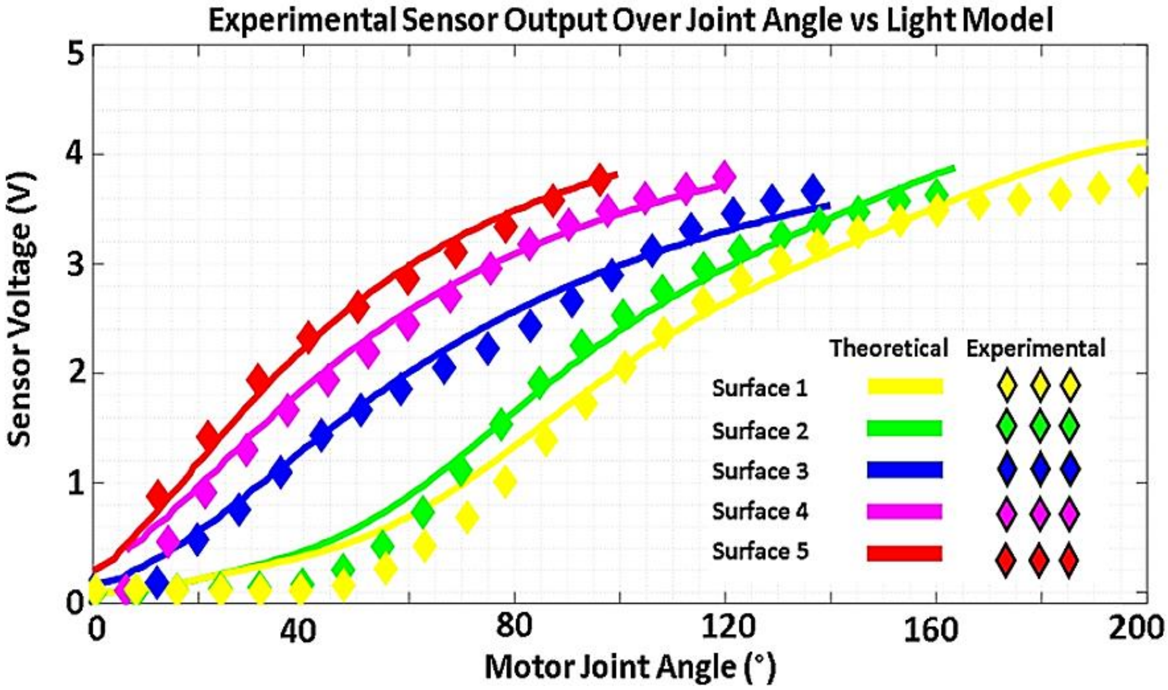

Figure 5.8: Results showing the sensor voltage output over a joint angle range of a set of different curvature surfaces (shown in Figure 5.5) collected during experiments (dotted). Each curve is compared to the theoretical output light intensity model [137].

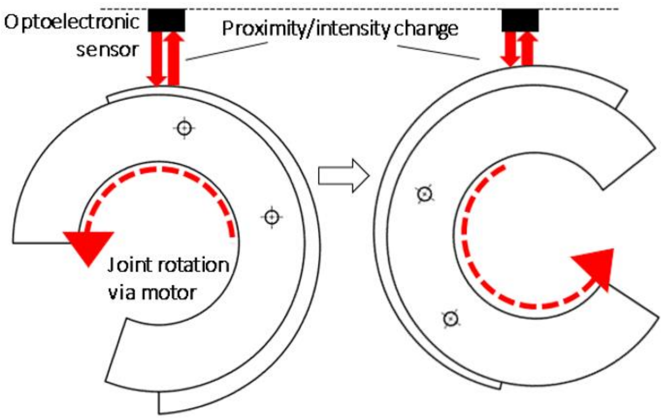

Figure 5.9: Schematic illustrates how sensor signal changes due to linear proximity change due to rotational motion of reflector, in reference to the graph responses in Figure 5.8.

Figure 5.8 shows the sensor output over the angular motion range of the servo motor based on the motor encoder data, with different reflective surfaces used of varying curvatures, as shown with the dotted lines. Figure 5.9 illustrates how the sensor response changes due to linear proximity change of the sensor to the reflector, during rotational motion of the reflector. As seen for Surface 5 (α = 100°), which changes through the thickness range (3-1 mm) over 100°, therefore having the highest curvature, the sensor output shows a high voltage variation.

TABLE 5.1: EXPERIMENTAL VS THEORETICAL JOINT ANGLE SENSOR OUTPUT

Curved Reflector	PERCENTAGE ERROR (%)	RMSE (°)
Surface 1	56.36	0.44
Surface 2	27.97	0.22
Surface 3	14.38	0.19
Surface 4	8.35	0.15
Surface 5	8.72	0.17

The voltage level increases from around 0 V to 4 V. Voltage variation decreases in looking at subsequent surfaces, such as surface 4 (α = 120°) and 3 (α = 140°), although show a longer angular sensing range, with the graph starting to plateau at later point. This is due to the signal starting to reach a saturation point as the maximum distance of the reflector to sensor is reached, where steeper curves reach this point earlier in the angle range. Surfaces 2 (α = 180°) and 1(α = 200°) on the other hand show the lowest voltage variation. Unlike prior tested surfaces, the initial increase of the graph is slower, likely due to a slower change in distance between sensor and reflector as the motor rotated, owing to the lower curvature. Comparing to the experimental data (dotted) is the theoretical output (solid line) for each of the surfaces, based on the equations describing the light model. The theoretical curves generated by the model show a good fit to the experimental data, which appears to follow the trend set by this predicted model data. Table 5.1 shows both percentage error and Root Mean Square Error (RMSE) between the experimental and theoretical data. Surface 5 (α = 100°) having a larger curvature shows the lowest error, while the largest error is seen for Surface 1 (α = 200°), having the lower curvature. As some assumptions were made to simplify the model, such as assuming the surface was flat despite the designed curvature, this may have been the reason for some deviation between the experimental data and the theoretical values. It is possible that in the lower curvature surfaces that were tested, more reflected light was directed towards the sensor in terms of scattering, as these surfaces were flatter compared to high curvature surfaces. Another general reason may have also been that although steps were taken to design a smooth surface with a highly reflective face, this may not have been as fully reflective as in the ideal case shown by the model. A resin 3D printer was used to fabricate the surfaces; however, some unevenness may have remained, which could have led to more scattering or the source of some noise in the data, adding to some mismatch between the experimental and theoretical data. Alternatively, this may have been due to some vibration in the motor during rotation. To improve upon these aspects, steps can be taken to create more ideal experimental conditions, such as better fabrication of the reflective surface, for example by the use of an aluminium evaporation technique. Experimental set ups and subsequent prototypes should be shielded from external ambient light to account for any background noise. Although these steps can be taken to improve results, it can be said however that the approach shows the basis of developing a simple joint angle sensor. The curved surface structure can be said to have increased the sensing range, for example as seen for surface 3 (α = 140°), that has a fully usable sensing range of 0° up to 140°, with a voltage variation of around 3.5 V. This is an improvement when considering previous attempts using a flat reflecting surface as shown in chapter 4 [106], which had a sensing range of around 40° due to the sensing configuration. Results are also comparable to some of the works listed earlier in Chapter 2. For example, [12], which shows the stretch conductive fluid sensor using for finger joint angle measurement, displayed a sensing range of up to 90°, as at larger angles the stretch sensor deteriorated, as well as during higher temperatures and humidities. Th exoskeleton robotic joint sensor [107], showed performance of joint angle measurement with 3.23° mean error, with a sensing range of around 90° and sensitivity of 0.047 V/°. The joint angle sensor based on an optoelectronic sensor and variable thickness canal to modulate the light intensity [108] showed performance of joint angle measurement with a maximum error of around 2.5°, with sensing range of 110° with 2.3 V voltage range. The principle of varying curvature of the reflectors to increase this voltage variation can be utilized depending on the required angular sensing range by the user. This is ideal as it allows the increase of sensor sensitivity, or resolution, and therefore accuracy to be achieved as required.

In reference to Figure 5.10, this shows the fit between the motor encoder angle data and regression model estimates for the calibration experiments of each sensor in the four-link chain. In using a fifth-degree polynomial model for fitting, this was able to fit well to the data, with Root Mean Square Error (RMSE) ranging between 0.86 to 1.59°.

Following on from this, Figure 5.11 (1-6) show the results of the shape sensing test, which included arranging the chain link in varying configurations and comparing estimated final link angles to that given by the IMU sensor attached at the end of the final link. The shape configurations are imaged, with an overlay of estimated angles for each link. Table 5.2 shows the percentage error between these two quantities. It can be seen that the shape sensing technique works relatively well and is able to estimate link angles with a degree of accuracy with different constructions of shape, with an overall average root mean square error of 2.40°. This error is comparable to some of the mentioned planar robots with integrated shape sensing, for example the magnet and hall effect-based shape sensor integrated into a 70 mm long planar robot, shown in [62], displayed average shape errors of 1.308°±0.15°. Another example was the micro-inertial sensor planar snake robot [109], for which joint angle measurement performance showed an average orientation error between 1.29° and 3.2° for pitch and roll orientations, or the optical fibre based planar snake robot [110], which showed

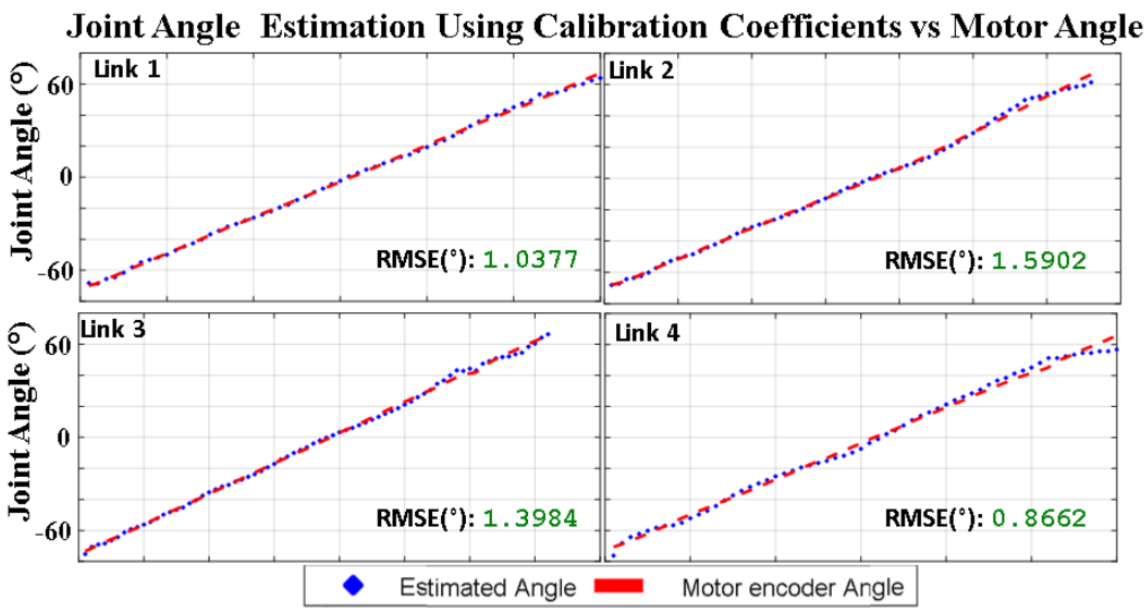

Figure 5.10: Results of calibrating each of the 4 sensors (using experimental set up shown in Figure 5.7, using the servo motor encoder data to map the sensor voltage to a joint estimation angle using a linear polynomial regression model. Root Mean Square Error (RMSE) between estimation and true joint angle is shown [137].

absolute mean orientation error of 0.71°. To improve upon this, future evaluation will involve development of more specialised application, with the aim of increasing accuracy and miniaturising the structure.

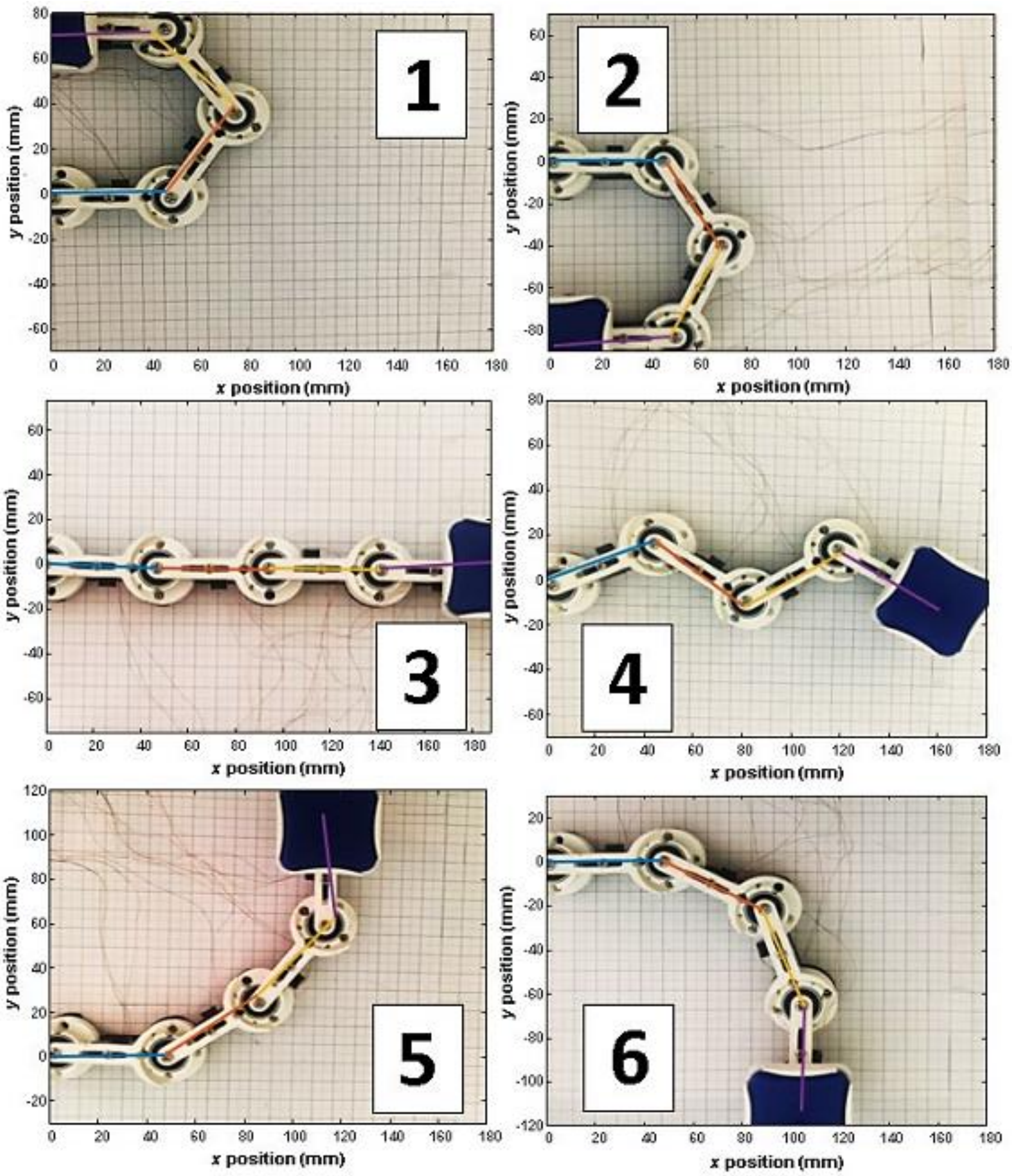

Figure 5.11: Shape sensing tests were carried out by constructing varying curvatures and positions of the prototype chain (numbered 1-6) and comparing estimates of final link angle against IMU sensor values. Images of the constructed shapes are graphically overlapped with estimated link angles [138].

TABLE 5.2: 4-LINK SHAPE SENSING RESULTS

Link Shape	Angle Estimation (°)	Actual Angle (°)	RMSE (°)
1	181.78	183.11	1.33
2	-174.94	-177.75	2.81
3	1.21	0.83	0.38
4	-32.72	-30.52	2.20
5	95.10	91.72	3.38
6	-96.06	-91.57	4.31

5.3 Two-Axis Tendon Actuated Robot Integrating Optoelectronic Shape Sensing With A Curved Reflector

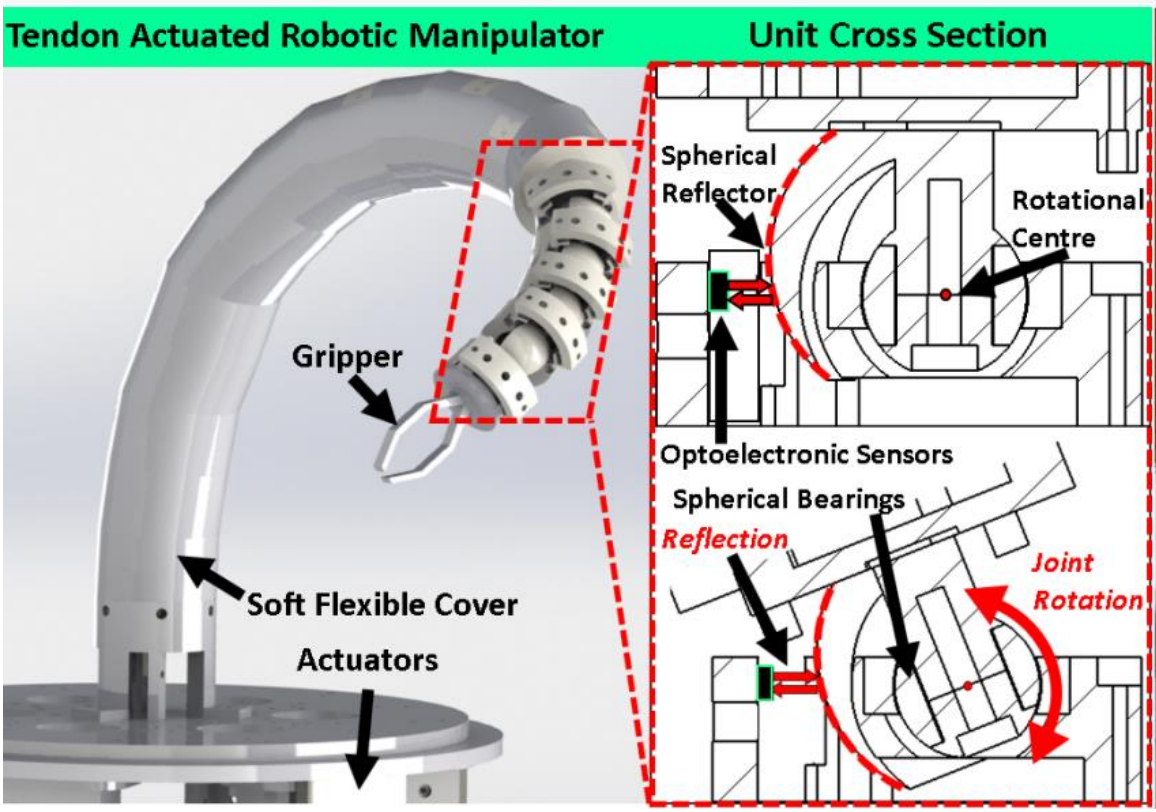

Figure 5.12: Concept image for a tendon actuated robotic segment with integrated optoelectronic shape sensing, with the sensing principle based on proximity modulation using a convex spherical reflector. As each unit of the robotic actuator bends, the linear proximity changes between the spherical reflector and optoelectronic sensors [115].

In this section, a novel optoelectronic shape sensing technique will be developed (shown in Figure 5.12). The results of the study demonstrated in Chapter 4 were able to prove the effectiveness of the optoelectronic based technique for shape sensing utilising the 'triple' sensor configuration, which was based on setting three optoelectronic sensors into the robotic actuator disks for proximity-based shape sensing. However, certain areas of improvement were identified, as were previously mentioned in Chapter 4. Firstly, each link of the robotic manipulator required three embedded sensors directly onto the disk. In longer tendon robots, this would lead to an excessive number of optoelectronic sensors and electric wires, occupying substantial space on the manipulator and limiting future tool passage. Secondly, the links were connected using a 3D-printed ball joint made of PLA, resulting in significant friction and subsequent vibration during prototype motion, which adversely affected calibration measurements. The prototype was also substantially larger than typically required size of MIS based robotic tools. Lastly, each sensor was separately installed in individual disks, resulting in excessive and disorganised wiring. Along with improvements to the structure of the robot, improvements to the sensor performance will also be made. As explored in the previous section of this chapter, it was known that sensor linearity, range and resolution could be altered through adapting different reflector shapes for intensity-based modulation as a sensing principle. This was tested on a prototype of a planar multi-jointed shape sensor, utilising curved reflectors, to estimate shape in one orientation. Here, these principles are applied in two dimensions, for shape sensing in two orientations, in this case by using a spherically shaped reflector rather than a curved one. As such, this section will present a new shape sensing mechanism that addresses the aforementioned limitations of the previous version with a novel shape sensing configuration.

5.3.1 Sensing Principle For Convex Spherical Reflector Based Optoelectronic Shape Sensing

In line with the same sensing principle based on light intensity modulation, a novel surface reflector shape was designed for the tendon actuated robot links. This new reflector takes on a spherical shape and acts as a convex reflector (Figure 5.13). The inner part of this convex reflector section aligns with the centre of rotation of the rotational unit. However, the outer boundary of the spherical reflector section, facing the sensors, has a slightly offset centre from the rotational centre, as shown in Figure 5.14. This has the effect of creating a sphere with a gradually changing radius upon rotation relative to the sensors. As a result, the proximity between the sensors and the reflector varies during rotation, enabling modulation of the reflected light. This modulation can be utilised to estimate the orientation in both pitch and roll rotations. As mentioned in section 5.2 regarding the joint angle sensor with a curved reflector, this demonstrated the potential for adapting sensing response of optoelectronic sensors for increased sensing sensitivity, and this is replicated here in for two orientations. Figure 5.15 illustrates the rotations in pitch (about y axis) and roll (about the x axis), with the

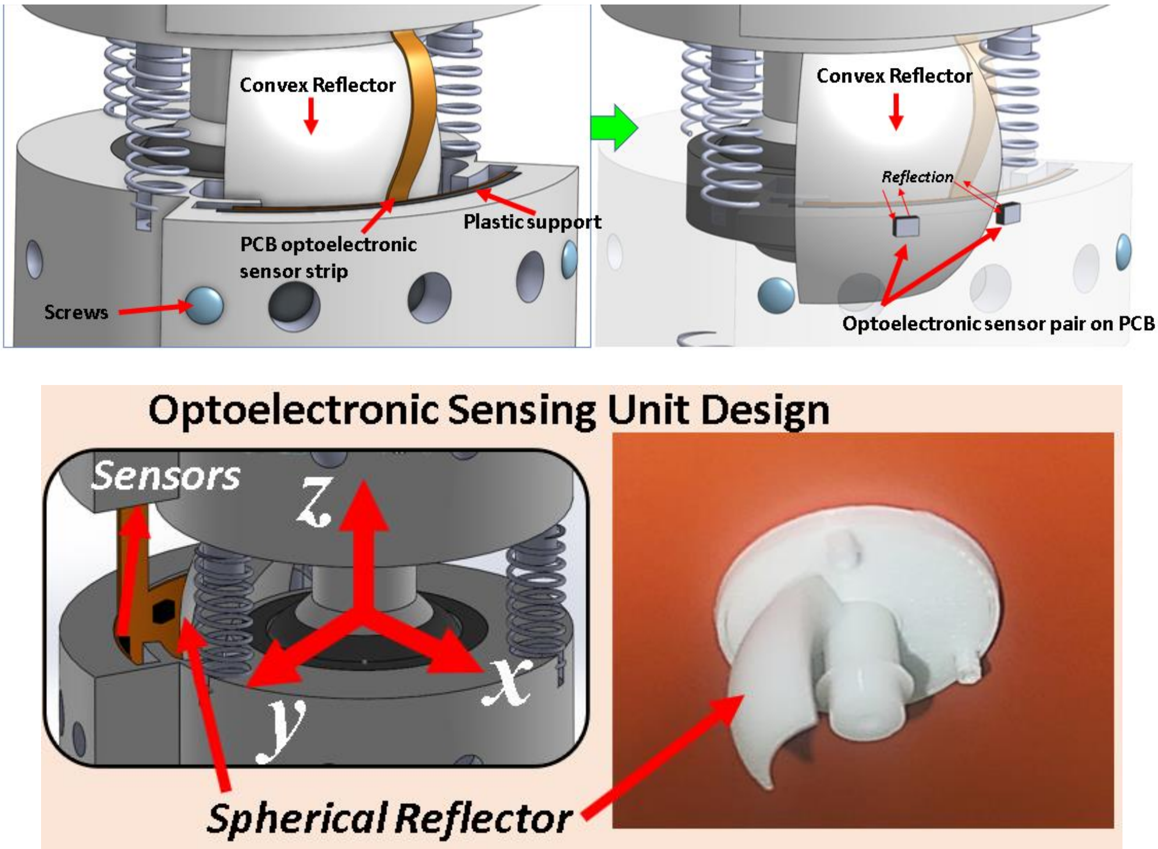

Figure 5.13: Convex/Spherical reflector integrated into the unit of the tenson actuated robot [115]. mounted onto the flexible PCB strip (orange) is place vertically along a channel in the tendon actuated, so that the mounted pair of optoelectronic sensors are place opposite to the spherical reflector. For a smooth surface, the spherical reflectors have been 3D printed using white resin.

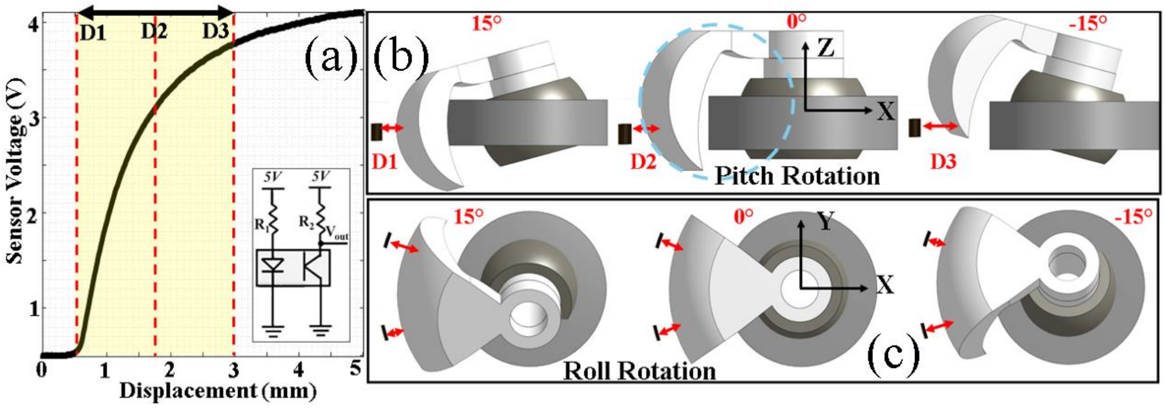

Figure 5.14: (a) The ideal sensing range (red dotted) is identified from the characteristic optoelectronic sensor output vs linear displacement against a reflective surface. Proximity between the sensor pair (black) and the convex reflector are shown for (b) pitch, and (c) roll orientations.

optoelectronic sensor pair placed circumferentially around the origin of rotation O, on the *xy* plane. Light is reflected from the convex reflector section (Figure 5.14) and recorded by the sensors. Considering the schematic in Figure 5.15a, the reflector with centre C is placed at a location offset to the rotation origin O. As such, when the reflector rotates about origin O, either in the pitch or roll orientations, the distance between the sensor and the reflector varies. This displacement variation with change in orientation allows change in sensor voltage readings due to varied light intensity for proximity-based sensing. Considering (Figure 5.14) pitch rotation, at 0°, the distance between the reflector and the sensors are set to D2, corresponding to the midpoint of the selected sensor output range (Figure 5.14a, yellow). The radius of the convex reflector is set so that at -15° and +15° in pitch rotation, the distance between the reflector and the sensors is D1 and D3. As the centre of the 'sphere' of the convex reflector is not aligned with the centre of rotation, it allows these proximity changes to be achieved during rotation. The large sensor voltage variation measured from this range allowed improvement to sensitivity and range of the sensor response, to aid in improved accuracy of shape sensing. The roll motion between -15° to +15° allows alternating proximities between the sensors, although these are smaller than the highlighted range identified in Figure 5.14a. Given these distance ranges, the spherical radius and centre C required could be identified and designed.

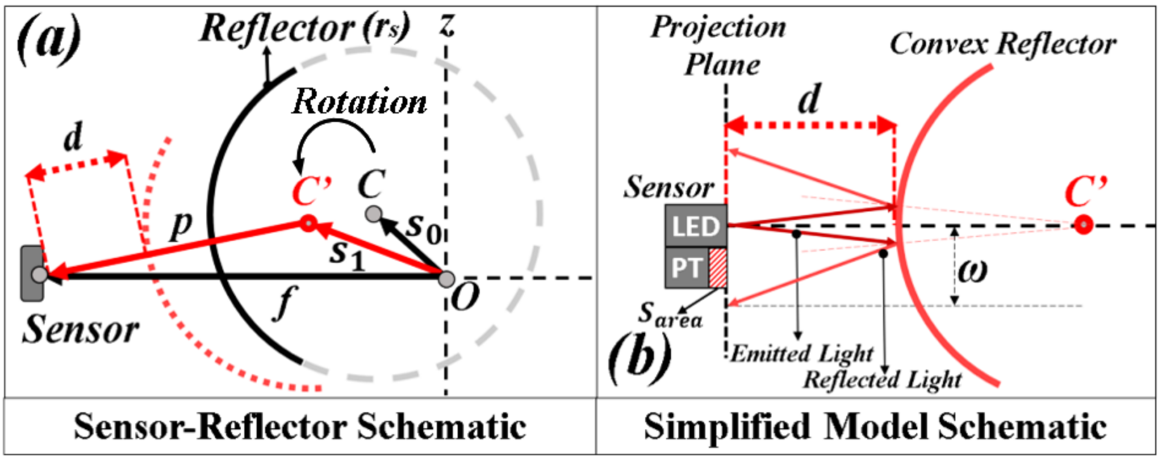

Figure 5.15 (a) Schematic diagram for calculation of proximity 'd' between the sensor and reflector (with radius r_s) upon rotation [115]. (b) Light intensity model schematic diagram, showing simplified path of gaussian beam between sensor and reflector.

5.3.2 Mathematical Model For Convex Spherical Reflector Based Optoelectronic Shape Sensing

The mathematical theoretical concept behind this sensing principle is simply based on the gaussian reflection of light against a convex reflector [111][112][113][96]. Figure 5.15a illustrates a schematic of the sensing configuration and shows a cross-sectional view of one sensor placement around the rotational spherical reflector component. It shows a system of how to calculate distance 'd' between the sensor and reflector. Given the centre of rotation *O*, vectors $\boldsymbol{f}$, between *O* and the sensor, as well as vector $\boldsymbol{s_o}$, between *O* and the spherical reflector centre *C*, can be known. Upon rotation of the unit about the origin in both pitch and roll orientations, as new vector $\boldsymbol{s_1}$ can be calculated using Equation 5.5, using rotation matrices R_x and R_y. From this, distance d can be calculated as shown in Equations 5.6 and 5.7.

$$s_1 = R_x R_y s_0 \quad (5.5)$$

$$p = f - s_1 \quad (5.6)$$

$$d = |p| - r_s \quad (5.7)$$

Considering Figure 5.15b, the schematic can be simplified, by making a few assumptions, to allow the set-up of a mathematic model to describe the sensing principle. As the LED size on the sensor is quite small, we can assume that light emitted from this to be of a point source. We can also assume, due to the small scale, that the area where light is incident on the reflector is small, and so it is taken to be a spherical convex reflector with a constant radius about centre *C'*. Using this, and values for d, as well as known phototransistor area (s_{area}) (Fig 5.15b), a theoretical reflected light intensity can be calculated using the gaussian power equation in Equation 5.8 [112]. Power is proportional to the light intensity and factors the cross-sectional area along the light beam path. Therefore, the initial power emitted by the LED, P_E, can indicate the input intensity, and the reflected power P, can indicate the output intensity detected by the PT. This equation integrates the reflected light beam with cross-sectional radius ω at the projection plane, over a circular cross section s_{area} of the phototransistor.

$$P = P_E \frac{s_{area}}{\pi \omega^2} \quad (5.8)$$

where,

$$\omega = f(d)$$

To validate the model, a series of simulated pitch and roll values were chosen to measure two sets of values 'd' for each sensor in a rotational unit. From these values, two sets of theoretical intensity values were calculated for the sensors using Equation (5.8). Next, MATLAB (R2022) was used to generate a calibration matrix by calculating coefficients through a linear regression algorithm, based on a least squares approach. Equation (5.9) shows the calibration matrix for estimating orientation (pitch (γ) and roll (α)) from the intensities (i_1 and i_2) using the coefficients $k_{1\text{-}4}$. To validate the coefficient matrix, another set of pitch and roll values were used to estimate intensity values for two sensors. These were multiplied by the coefficient matrix to get estimate pitch and roll values (α and γ). These were plotted against the actual pitch and roll values used, as can be seen in Figure 5.16. Here it can be seen that the estimation compared to the actual values have substantial overlap. It is assumed that deviation from the expected values that occurs may be due to not deriving an exact model due to the generalisations made. Despite this, it can be seen that orientation motion patterns can be estimated with some accuracy using two theoretical intensity values belonging to two sensors. Therefore, as intensity is proportional to voltage induced in the phototransistor of the optoelectronic sensor, it can be deduced that the sensing principle could work in practice and that two sensor voltage values can be used to estimate two orientations during motion.

$$\begin{bmatrix} k_1 & k_2 \\ k_3 & k_4 \end{bmatrix} \begin{bmatrix} i_1 \\ i_2 \end{bmatrix} = \begin{bmatrix} \alpha \\ \gamma \end{bmatrix} \qquad (5.9)$$

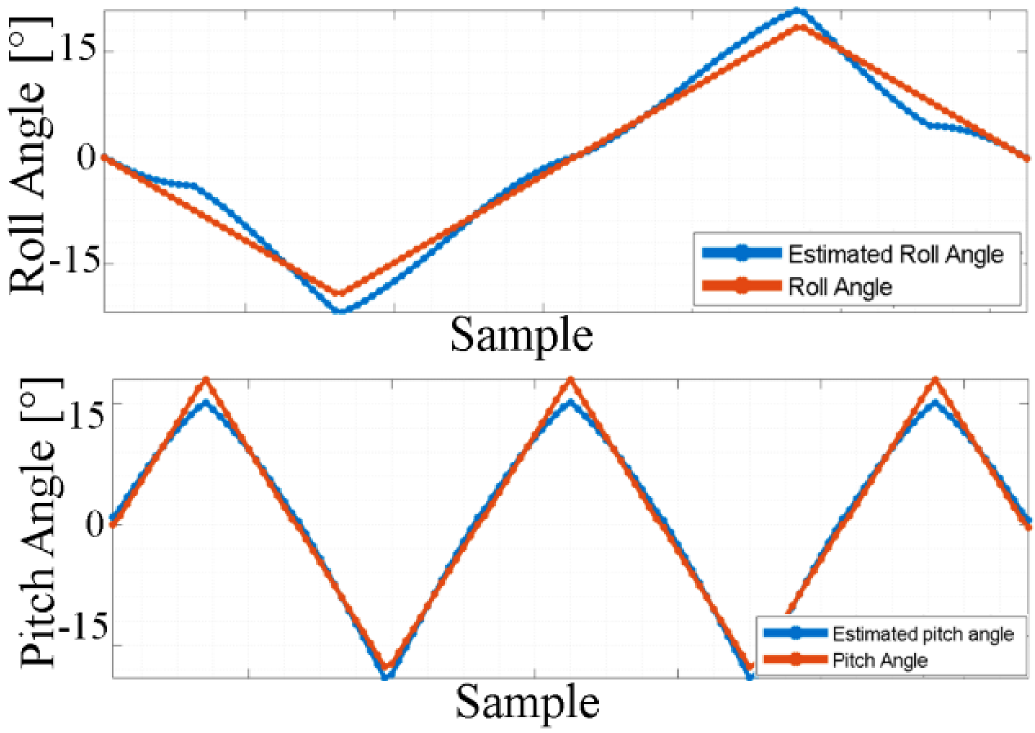

Figure 5.16: Estimated pitch and roll based on the theoretically calculated intensity values P1 and P2 compared to generated motion data in pitch and roll [115].

5.3.3 Development of Two-Axis Tendon Actuated Robot Integrating a Convex Spherical Reflector

To improve upon the constructed tendon actuated robot demonstrated in Chapter 4, the new prototype shown Figure 5.17a, and 5.17b has the following upgrades installed. Firstly, the 3D PLA printed socket-ball joints were substituted with spherical bearing (GE6-DO 6mm Bore Spherical Bearing, 14mm O.D, INA) components. These bearings are securely fixed within the rotational unit and connected to the consecutive unit via a shaft that fits into the spherical bore. This modification greatly enhances motion and virtually eliminates friction, resulting in seamless rotation between joints. The diameter of the disks was further reduced to 22 mm, with 12 mm height gap between disks. Further reduction in diameter was limited by the spherical bearing, as this was the smallest commercially available model for order. However, this can be solved through special order of a smaller spherical bearing, which can be applied

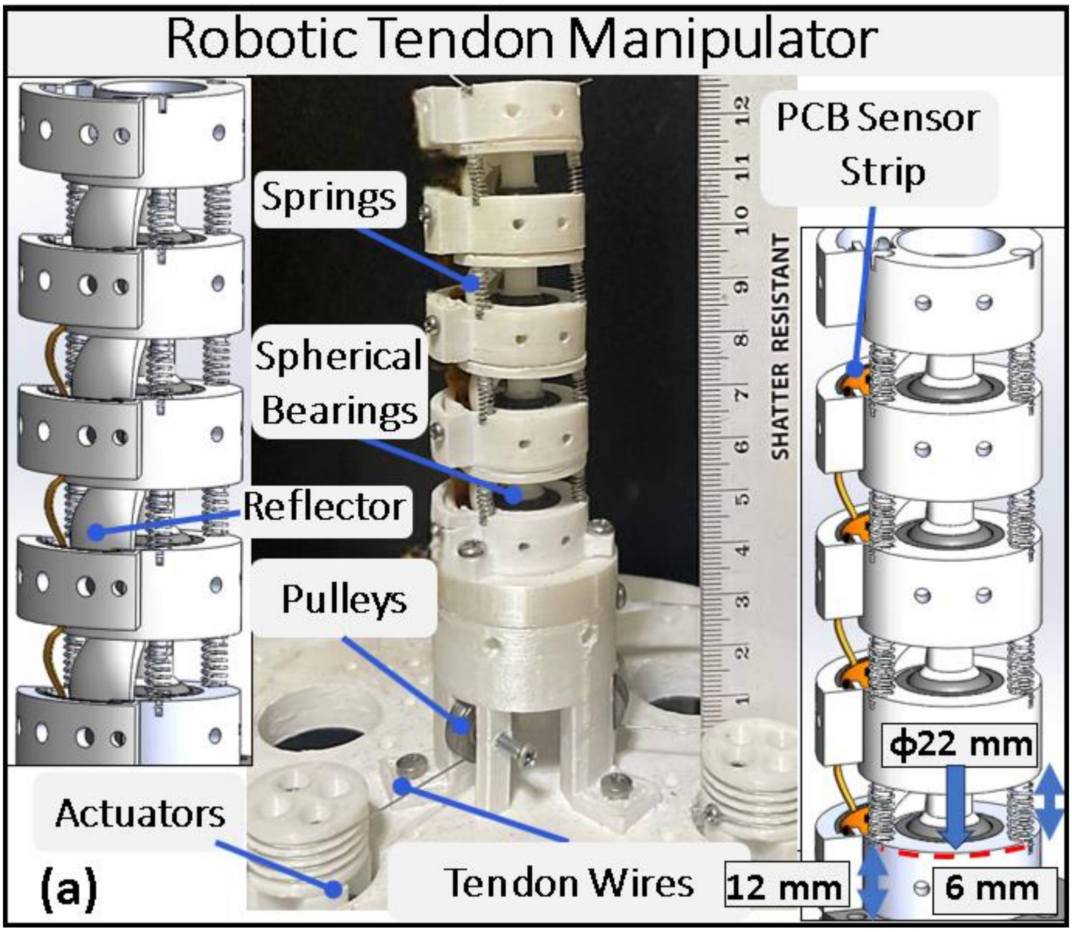

Figure 5.17: (a) New tendon actuated robot with integrated improvements, including spherical bearings, integrated flexible PCB strip, and convex spherical reflectors [115].

to future prototypes. Additionally, the sensing configuration in the new system has been improved. Instead of three optoelectronic sensors per rotational unit, the new design utilizes two vertically fitted sensors, significantly reducing the space occupied by each link. All sensors are integrated onto a single flexible circuit (Figure 5.17c), eliminating the need for complex wiring and simplifying the overall design onto a single strip. For the sensors, a smaller model of optoelectronic reflective sensor, the NJL5901R-2 (1 x 1.4 x 0.6 mm, New Japan Radio), was chosen compared to the previously used QRE113 ON Semiconductor (3.6 x 2.9 x 1.7 mm). This choice further reduces the space required by the sensors. The PCB sensor strip, which was designed in EAGLE, this was a two-layer design, with 8 sensors arranged into pairs, each for

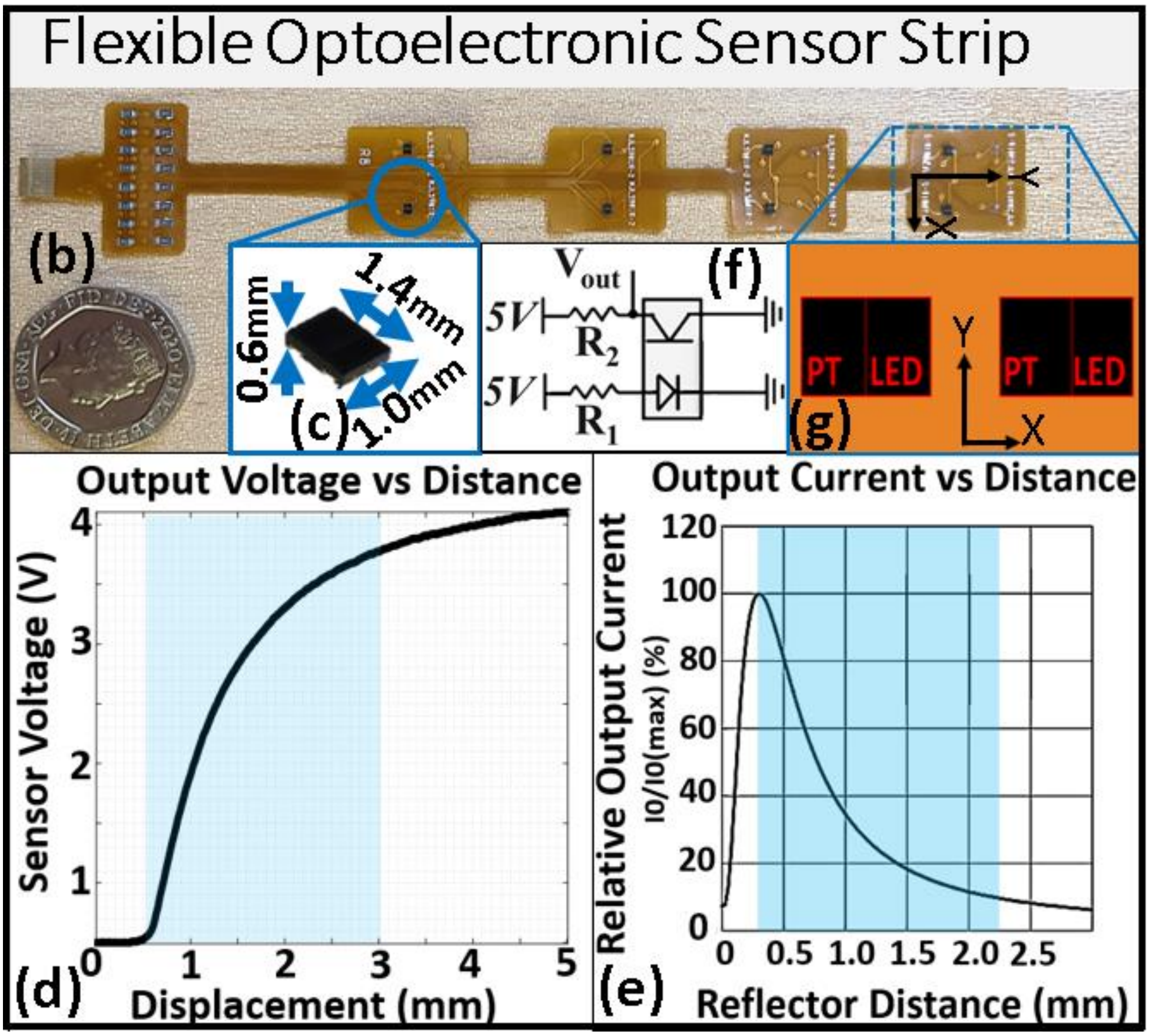

Figure 5.17: (b) Flexible PCB strip (c) NJL5901R-2 optoelectronic sensor dimensions, (d) Characteristic voltage sensor output of NJL5901R-2, R_1 = 680Ω, and R_2 = 10 kΩ. (e) NJL5901R-2 sensor relative output current vs displacement (datasheet), (f) Optoelectronic sensor circuit, (g) Optoelectronic sensor component placement of PCB [115].

fitting into each disk of the tendon actuated robot. At the base of the sensor strip, the resistors are arranged, with eight LED resistors R_1, and eight PT resistors R_2 on the bottom row. The connector of the PCB comprises of eight voltage output pins, for each sensor, one ground pin, and one 5V pin to supply power to the sensors. Sensor can be connected to a 10-pin FPC converter board, and to this jumper cables were used to connect the pins to the Arduino Uno microcontroller. Other than this, the actuation mechanism of the robot was similar to the first prototype, comprising of three DC motors to actuate three wire tendons, utilising a pully system to achieve motion in the pitch and roll orientations. For verifying the sensing principle of the new shape sensing mechanism, to be described in the following sections, four consecutive units are used as a one bending segment, with the fitted flexible sensor circuit. Each disk consisted of a newly designed spherical reflector, which was to be used for a novel sensing proximity-based configuration. Set of springs between each unit were again fitted to limit some of the torsion motion. The springs between each unit were 6mm in height. A channel down one side of the structure was used to allow the optoelectronic sensor strip, to be fitted (Figure 5.17a). The sensor strip was fixed along the channel at each unit of the robotic structure using two small screws. On the top unit, a frame is fitted for allowing the IMU sensor (LPMS B2, LPRESEARCH Inc, Tokyo, Japan) to be fixed. The platform components were designed using CAD software (Onshape) and other than the convex reflector component, were 3D printed using white PLA (Polylactic Acid) plastic. The convex reflector component was printed using a UV Resin SLA 3D Printer, with white coloured resin, for high resolution surface finish in order to maximise reflectivity and reduce noise in the sensor signal. For actuation – motion was controlled using similar software developed on Python, with real-time interfaced motor control, optoelectronic sensor recordings, as well as IMU sensor recordings. To achieve motion, an input target orientation of the top plate is chosen, and a vector-based model, described in Chapter 4, is used to calculate the required tendon lengths in order to convert to three target motor positions. As the three motors move simultaneously, each pulls a tendon wire over the pulley for continuous motion.

5.3.4 Calibration of Convex Reflector Based Optoelectronic Shape Sensing for Tendon Actuated Robot

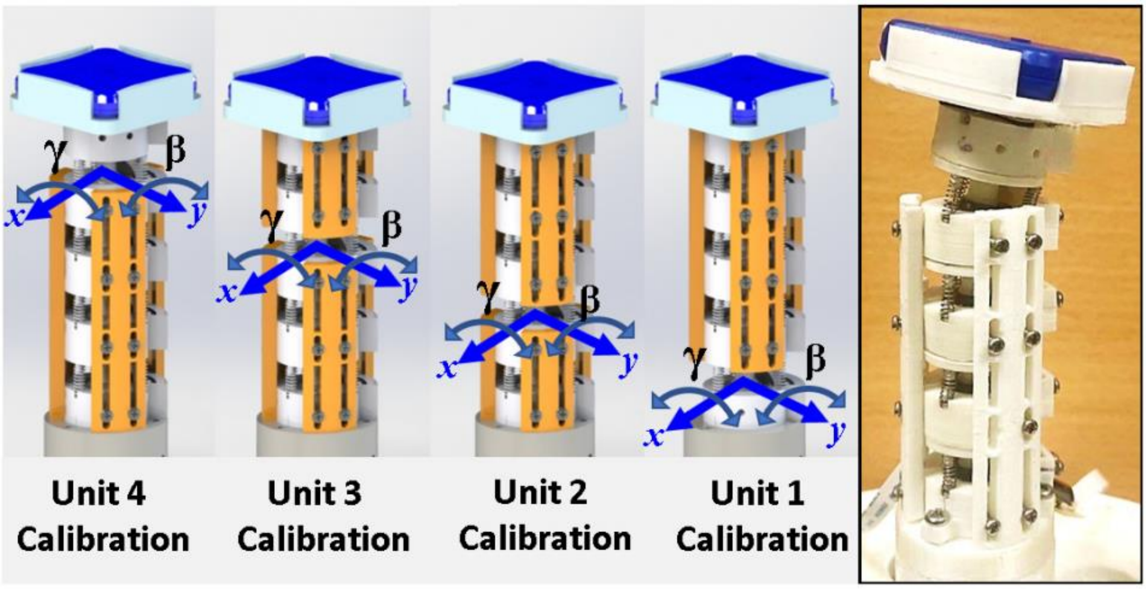

Figure 5.18: calibration Process for each pair of sensors in each disk by recording full range of motion data at each level [115].

The experimental platform was designed as shown in Figure 5.17a, comprising of a section of a flexible tendon actuated robot. For the calibration of each pair of sensors at each disk, the same process was used as described in Chapter 4 for the first prototype. This is shown in Figure 5.18. Here, an improved design of the locking mechanisms was used, using 3D printed rigid fixtures that could be screwed around the robotic structure in a way that limits its motion, rather than directly locking into the gaps between the disks. Once again, to calibrate the two sensors on the top unit, the fixtures were fixed onto the three lower units, removing any capability for motion in these units while allowing motion due to tendon actuation in the top unit. A motion pattern was generated to cover all angles in both pitch and roll direction in increments of 0.1° in these two orientations up to ±15°. During the motion, both sensor readings and IMU orientation data readings were recorded. This provided a full set of sensor readings for the full range of motion for that disk. Calibration was carried out using the IMU data and sensor readings with non-linear regression algorithms to find coefficients that transformed the two sets of sensor voltages to an estimation of pitch and roll. This was repeated for all four units involving each pair of sensors. As such, an estimation of pitch and roll could be made at each rotational unit, and therefore, an estimation of the total orientation of the full manipulator could be made.

Validation of the calibration results is carried out by setting the full robot to move to its maximum angle range of ±60°in both orientations. All sensor voltages were recorded during this motion and multiplied by the calibration coefficients to give estimated orientations during motion and compared to the orientations given by the IMU sensor. These results are shown in the following section. Regarding the light intensity model described in 5.3.2, we can further evaluate the validity of this by comparing sensor output voltages during motion to estimated light intensities given the same motion pattern.

5.3.5 Calibration Results & Analysis

Figure 5.19 shows the output of calibration for one unit of the robotic structure. It shows the recorded IMU data, with both pitch and roll measurements between ±15° in incremental steps as described previously. This data is recorded along with the two sets of sensor voltages during motion, shown also in Figure 5.19. As can be seen, the motion data is more stable compared

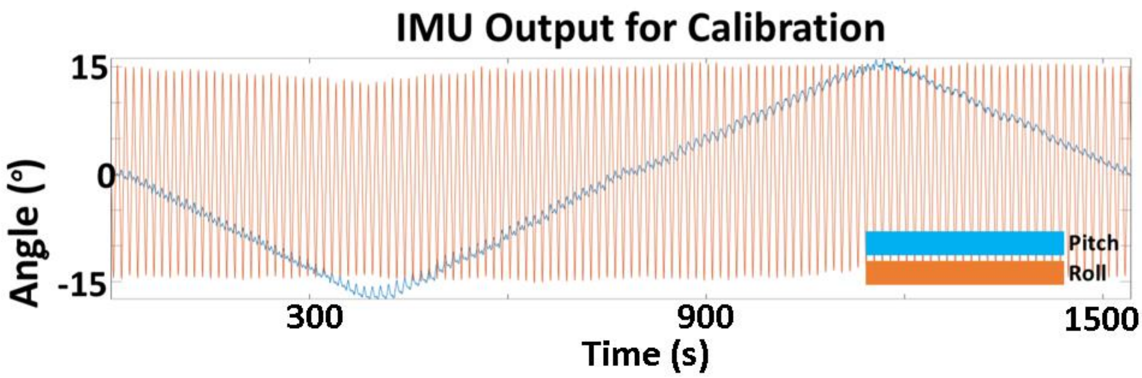

Figure 5.19a: Output for single unit calibration, displaying sensor output along with full set of recorded IMU orientation data [115].

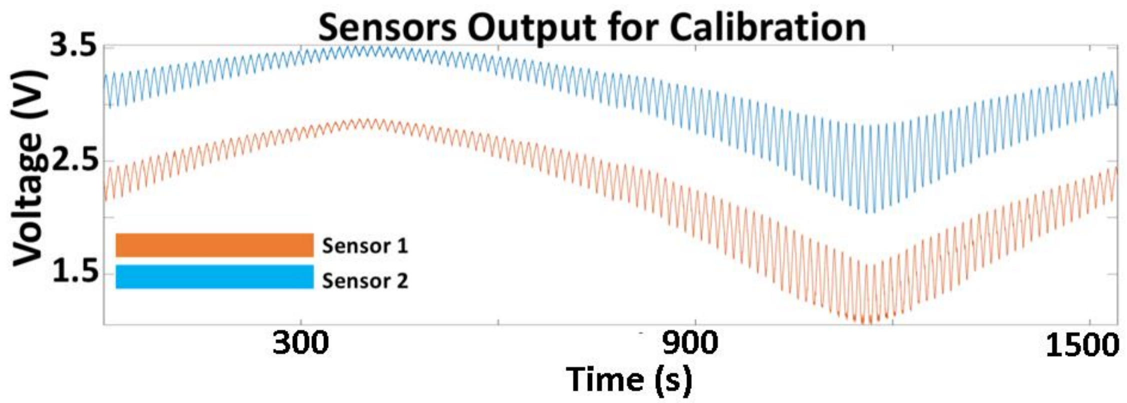

Figure 5.19b: Output for single unit calibration, displaying sensor output along with full set of recorded IMU orientation data [115].

to previously referenced technique [85], that used a PLA printed ball joint as opposed to a spherical bearing as is done here. The use of this bearing eliminated some of the noise previously seen in the sensor data, owing to friction, and motion is a lot smoother. Another observation is that the sensor response between sensor 1 and sensor 2 are not identical and have difference maximum ranges. This is despite the optimisation of sensor signal that was carried by through identifying the ideal spherical reflector shape based on the characteristic graphs of the sensor. This appeared to be the case due to the sensor placement design. The placement of the sensor pairs were not symmetric around point O in regard to the orientation of the LED and Phototransistor (Figure 5.17g). This resulted in slightly different sensor responses, which may have affected the sensing system properties in terms of range and sensitivity. This can be rectified in future prototypes through redesigning sensor placement of the flexible printed sensor strips.

Next, Figure 5.20 shows the graphs for both sensors one and two during one rotational unit calibrating motion and compares the sensor voltage output to estimated relative reflected light

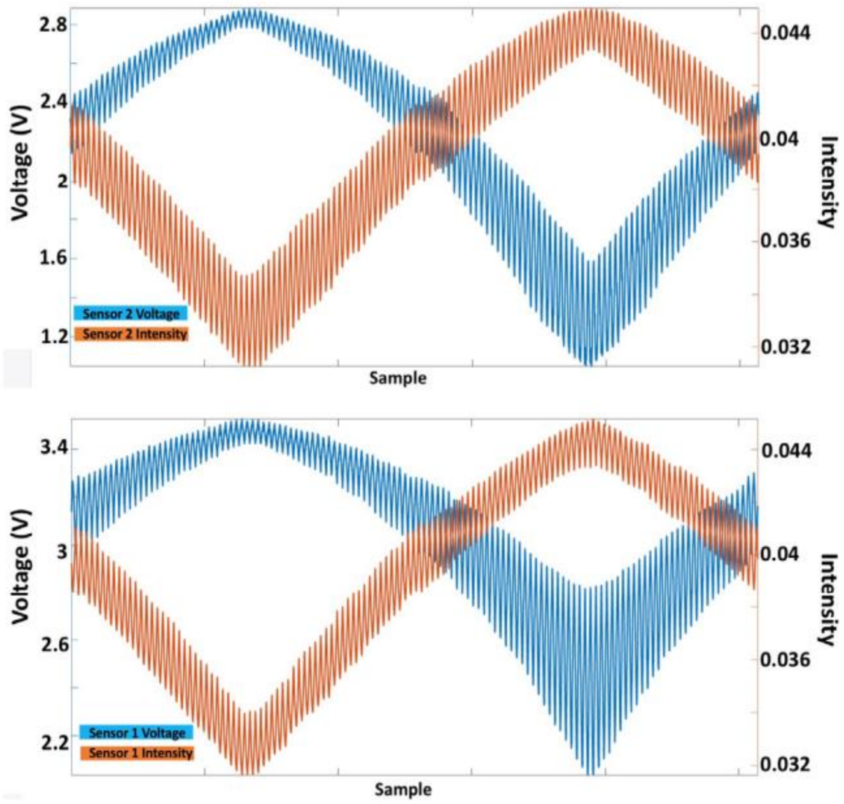

Figure 5.20: Comparing sensor voltage output with theoretically estimated light intensity [115].

intensity. As can be seen, the estimated light intensity generally follows the sensor voltage pattern. It is however inverted relative to the sensor voltage. This is because when considering the interaction of light with the sensor - the intensity collected by the phototransistor is proportional to the current. This current induces a drop in the voltage output of the collector in the phototransistor (Figure 5.17e), which is the value shown in the graphs in Figure 5.20. This current is inversely proportional to the voltage drop displayed in the graph. This was also seen when comparing Figures 5.17d and 5.17e, which show the characteristic sensor behaviour, comparing relative output current, to output voltage. As such, we must update the model to find a relation between the actual sensor output and the theoretical intensity currently described by the model. In another aspect of this comparison, we can see that sensor 1 and 2 voltage outputs differ in range and starting voltage level, whereas for the estimated intensity series, the starting values are almost identical in range and starting value- indicating

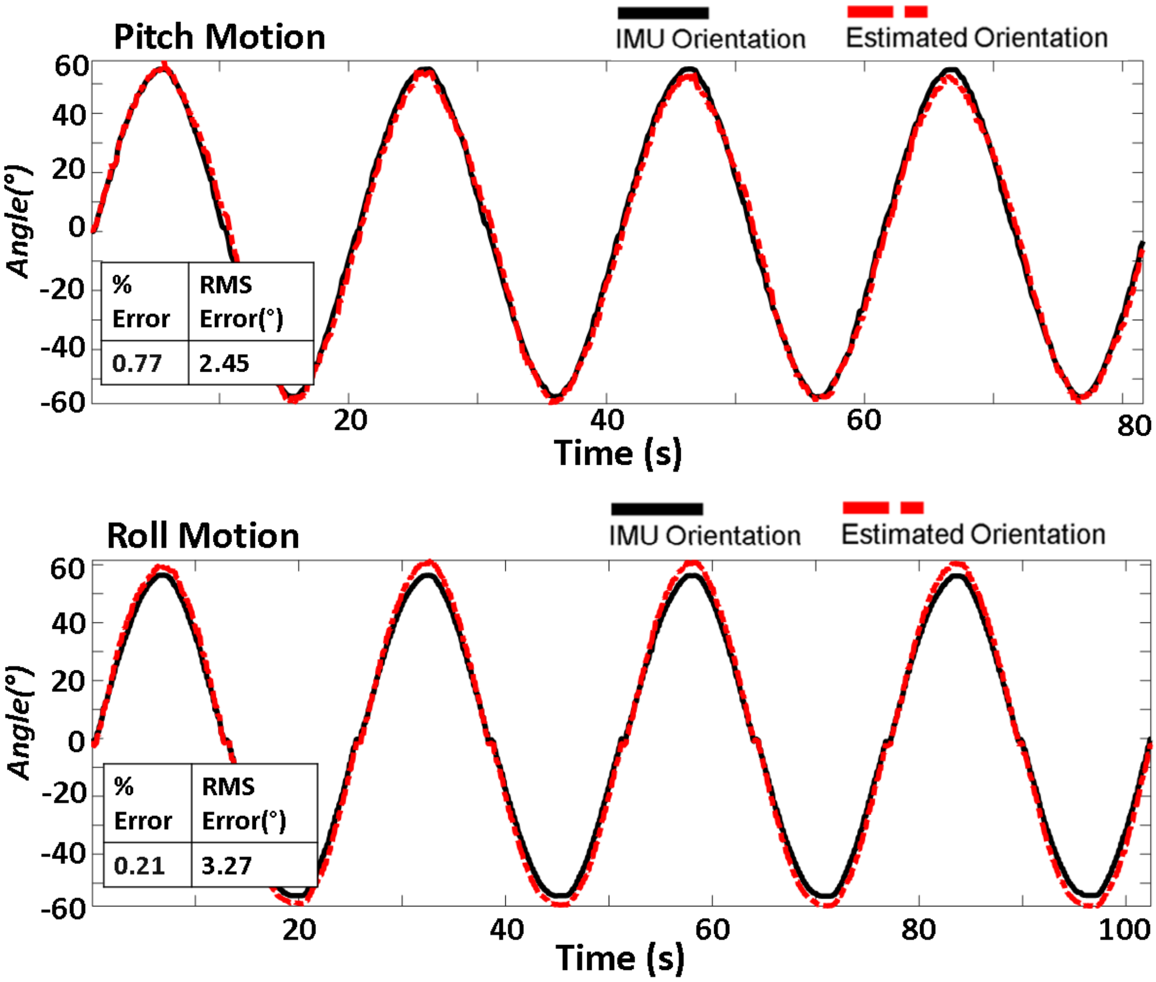

Figure 5.21: Orientation estimation validation results based on calibration of sensors [115].

symmetry between the sensors. As this is the case described by the model, a reason for which this is not reflected in the real sensor output may be due to non-symmetric sensor placement as mentioned previously. By updating the modelled sensor placement, this can, in the future be directed to a more correct prediction. Nonetheless, it can be shown that the model may predict tendencies displayed practically in the experiments. Upon further refinement of the model for more realistic output, the estimated light intensities can be used to closely predict real sensor responses for this shape sensing technique.

For calibration validation results shown in Figure 5.21, it can be seen that orientation estimation was successful. The maximum motion range of ±60° in purely pitch, as well as roll orientations were carried out. Orientation estimations based on the calibration coefficients calculated through a non-linear regression model closely follow the orientation given by the IMU sensor, with **maximum RMS orientation error of 3.27°, and percentage error of 0.77%.** These are promising results and show potential for further development of shape sensing in flexible robotic applications.

Looking back at the early work of this optoelectronic based shape sensing [85], this work comprised of three disks of a tendon actuated robot, with length of 100 mm, with three optoelectronic sensors embedded in each disk to measure two orientations. Results showed error of 18° (33.3%) in the roll direction, and 9.7° (21.2%) in the pitch direction. The more advanced development of the optoelectronic shape sensing shown at the end of Chapter 4 showed improved results (Figures 4.17 and 4.18) [114], with 2.52° (1.11%) in the roll direction and 3.23° (1.31%) in the pitch direction. As can be seen there is an improvement over the two. Comparing the optoelectronic shape sensing shown in Chapter 4.7, with the spherical based optoelectronic shape sensor shown in this chapter [115], results are comparable although the latter is slightly higher. This is despite however a shape sensing system that utilises two rather than three optoelectronic sensors per disk of the robotic structure. Having a look at some of the alternative shape sensors mentioned in Chapter 2, results can also be compared. The electromagnetic sensor-based shape sensing integrated into a three-segment tendon actuated robot, with a length of 360 mm, showed an average positional tip error of 1.77 mm [59].

Another optical fibre-based shape sensor that utilised magnet to estimate shape through intensity modulation, integrated into a tendon actuated robot of length 60 mm, showed performance of 4.1 mm average positional shape error, with an average orientation error of 4.5° [71]. The FBG based tendon actuated robot (160 mm long), showed distal tip errors of 0.67, 1.17 and 0.87 mm for a range of trajectories in a circular, square and helical shape [116][18]. Another FBG based shape sensor integrated into a tendon actuated robot (80 mm long), that utilised the braided lattice wire, displayed the following performance: Tip tracking error of 0.84 ± 0.62 mm and an orientation error of 1.21 ± 0.91°[16].

5.4 Conclusion

This chapter explored the design and experimental validation of an optoelectronic joint angle sensor utilizing a curved reflector to improve measurement range and sensitivity. By varying the curvature of the reflective surface, different sensor outputs were analysed, showing that higher curvature surfaces yielded a larger voltage variation and improved sensitivity. Experimental results aligned well with theoretical light intensity models. The approach was extended to a multi-link system, demonstrating its applicability in planar shape sensing for wearable sensors and robotics. Calibration tests confirmed the reliability of the sensor, with shape-sensing experiments showing an average root mean square error (RMSE) of 2.40°, comparable to other state-of-the-art sensing techniques. Future work will focus on further miniaturization, refining surface fabrication for improved reflectivity, and exploring specialized applications to enhance accuracy. These findings highlight the potential of curved reflectors in optoelectronic sensing, offering a scalable and adaptable solution for various robotics applications. For this reason, the concept is extended to two dimensions, by developing a spherical reflector integrated into a two-axis tendon actuated robot, using a pair of optoelectronic sensors to estimate shape in two orientations.

It can be said that shape sensing technique using optoelectronic sensors coupled with a spherically convex shaped reflector is successful in orientation estimation in two degrees of orientation. The sensing configuration in this system is greatly reduced in size and utilises fewer sensors while successfully estimating orientation in the same motion range of the robotic manipulator, compared to previous prototypes. The use of a single flexible circuit eliminates wiring for a more simplified design, while use of a spherical bearing for the robot structure allows for smoother motion and subsequently better calibration results. The smaller sensor model along with the sensor configuration only require a very small range of change in proximity for a large voltage variation, compared to the previous sensing configuration and sensor model. For this reason, miniaturisation is further supported in this way, and there as the proximity range is short, there is less likelihood of the recorded sensor signal becoming infiltrated by external noise such as from any sources of ambient light, or reflectance from nearby surfaces or objects other than the spherical reflector.

For future improvement in consequent prototypes, certain features can be addressed to improve suitability to different applications. The overall size of the current version is still big for use in MIS, and its safety pertaining to large-scale electric current from multiple optoelectronic sensors in all segments should be guaranteed. Regarding the current design of the tendon actuated robot, by decreasing the size of the spherical bearing that forms the ball joints between the units, the overall diameter of the units can be reduced. An example is if a commercially sourced spherical bearing of 8 mm outer diameter is used, the diameter of the robot can get down to 12 mm. Commonly MIS based continuum robots are much smaller than this scale, although this is very dependent on the application and procedure. There has been reported designs for a surgical continuum robot for surgical interventions, by Degani et al [117], of the HARP robot, which had a diameter of around 12 mm, at a length of 300 mm, or for example work in [118] shows a continuum robot with diameter of 12.5 mm used in in vivo trials for liver retraction. However, it is apparent that a more suitable application for this work would be for purposes such as inspection of engines/machines/airplanes or search operations, for example, [119] and [120] demonstrate designs for continuum robots for use in turbine engine inspection and engine repairs, with diameters of 12.5 mm to 18 mm. Other tasks such as soil exploration [121], [122] has been studied with robots of slightly larger diameters of 20-25 mm.

Regarding safety, use of a power source switching circuit through an is proposed to provide all the current required for all the optoelectronic sensors, thereby reducing overall power consumption in the robotic manipulator. This would also eliminate interference of signal between adjacent pairs of sensors, which would likely provide more accurate and stable shape estimation. The maximum angle measurement range of this shape sensing mechanism is limited due to a lower number of units in a one segment so more units will be added to achieve up to 90° bending range. In addition, for testing in more realistic conditions, a full-length robot will be designed in the next chapter, integrating this shape sensor for testing in more application-based environment.

CHAPTER 6: TWO-SEGMENT TENDON ACTUATED ROBOT INTEGRATING OPTOELECTRONIC SHAPE SENSING WITH A CURVED REFLECTORS

6.1 Introduction

The previous chapter introduced an optoelectronic shape sensing technique integrated into a single segmented tendon actuated continuum robot. In this chapter, the constructed continuum robot is extended to two segments, actuated by three motors each. The segments are made up of six units, connected by a ball joint using a spherical bearing. For installation of the sensors, a flexible PCB strip housing the pairs of sensors are designed and fabricated. These are fitted along the manipulator as shown in Figure 6.1, along with the convex reflectors. In the subsequent sections, the sensing principle, system design, calibration process, as well

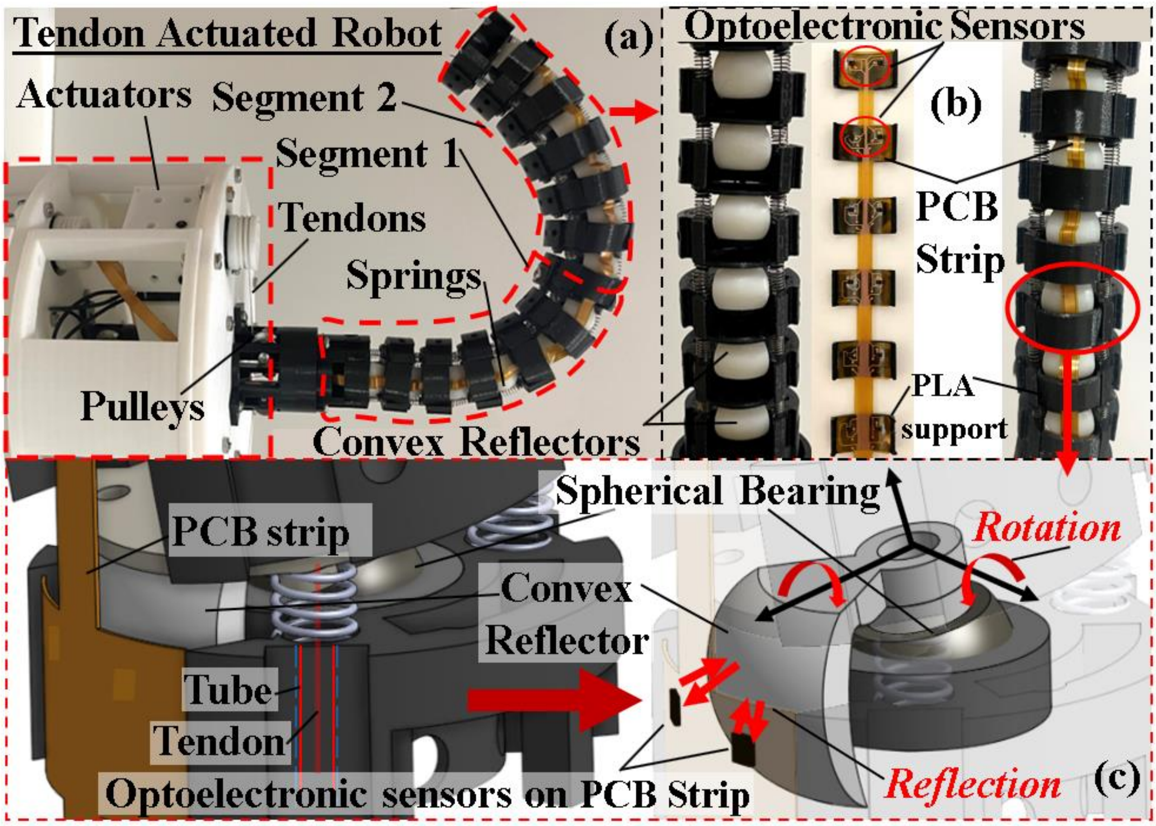

Figure 6.1: (a) Two Segment tendon actuated robot with optoelectronic shape sensing integrated for shape estimation on two orientations. (b) Flexible optoelectronic PCB strip integration. (c) Light intensity varies sensor signal during rotation of each unit, depending on proximity to convex reflector.

as shape sensing evaluation experiments will be described. Some of the improvements made to the system, compared to the spherical reflector-based shape sensing technique demonstrated in [115], are as follows. The new design includes a power switching circuit, that alternates power between pairs of optoelectronic sensors during operation, in order to eliminate instances of interference between sensors, which was a previous potential source of error of shape estimation. This also serves to reduce overall power consumption. A new optoelectronic PBC is fabricated to accommodate this, comprising of six pairs of sensors to fit into six units of the robot segments. Thirdly, the mechanical robustness of the tendon actuated robot is improved through the use of low friction tubes to line the routing paths of the tendons of the continuum robot, to ensure smooth motion for accurate calibration and during actuating to large curvatures. Lastly, a new calibration procedure is designed, using a linear frame that can slide vertically along the robotic structure and fix the motion of a number of units while the pairs of sensors are calibrated consecutively. This is a simplified process compared to the calibration process in [115], which utilised a number of rigid fixtures around the structure of the robotic manipulator. These improvements will be further explored in the following sections.

6.2 Design of Two-Segment Tendon Actuated Robot with Integrated Optoelectronic Shape Sensing using Spherical Reflector

6.2.1 Design Concept

Based on the previous work [16], some improvements were mentioned to aid in improving the performance of the shape sensing. These have been implemented in the following design. Firstly, there was some friction caused by the tendon wires being pulled through the units, which inhibited smooth motion of the tendon actuated robot. In anticipation of this effect increasing in a longer length of the continuum robot prototype, this was mitigated by fixing sections of a narrow low friction tubes into the tendon wire routing paths of each unit, as can be seen in Figure 6.1c. This is so that the walls of the routing paths became smooth, enabling the tendons to pass through the centre easily. Secondly, a new flexible optoelectronic PCB strip

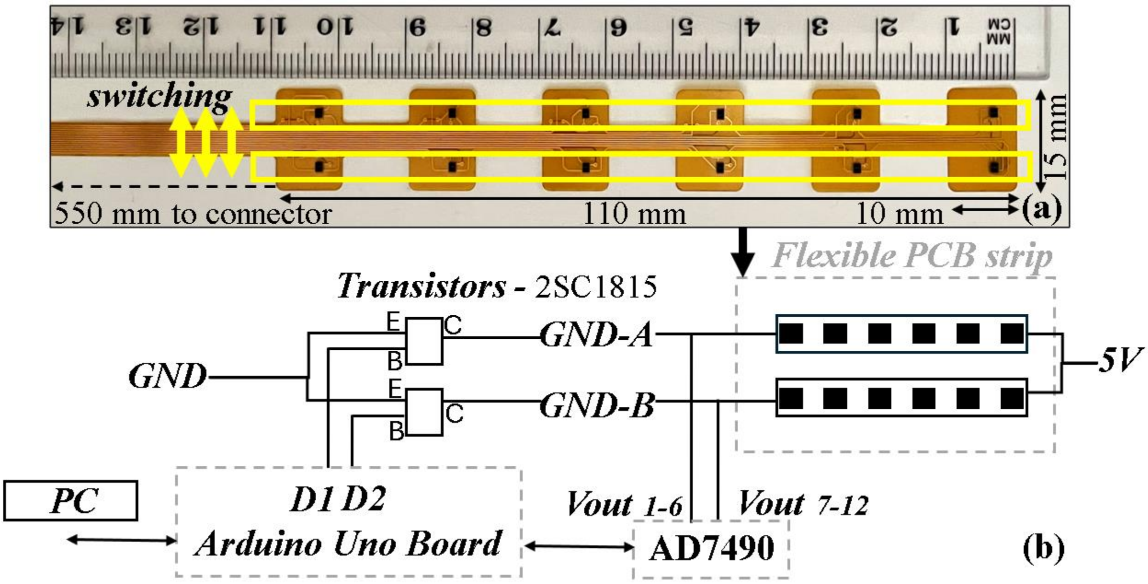

Figure 6.2: (a) Flexible optoelectronic PCB strip design. (b) simplified schematic to illustrate switching of column of sensors in one PCB.

(Figure 6.2a) was fabricated, housing six pairs of optoelectronic sensors (totalling 12). These sensors are used to estimate orientations of six units of the tendon actuated robot segment. With the rotation range of each unit set to ±15° in both pitch and roll orientations, each segment can now reach a larger bending range of 90°, and with two segments, 180° can be achieved. This allows more practical evaluations of the shape sensing techniques. Finally, the authors previously mentioned that potential shape estimation error that accumulated through each unit may have been due to interference between the sensor pair at each unit. This referred to an instance where infrared light emitted from one optoelectronic sensor may have been unintentionally detected by the second sensor. To resolve this, a current switching feature was designed with the new PCB, so that power is alternated between the two adjacent columns of optoelectronic sensors. This is described in the following section. To aid this, the components of the tendon actuated robot were also 3D printed in black colour, to reduce instances of increased scattering that may cause sensor signal interference.

6.2.2 Flexible PCB Design

The updated sensor PCB design introduces some features for ensuring the reduction of interference between the sensors. Figure 6.2 shows the fabricated flexible PCB strip. The optoelectronic sensor components are organised in pairs along the strip, to spatially coincide with the units of the robotic manipulator. The pairs of sensors are spaced 8 mm apart. The sections housing the six pairs of optoelectronic sensors measures 110 mm in length, and 15 mm in width (Figure 6.2a). A long section of the PCB extending from this measures 550 mm, allowing connection at the distal end to the main circuit board. Due to their proximity, it was identified that there may be a risk of interference between the sensors during operation at certain configurations, which may subsequently affect accuracy of shape sensing. To avoid interference within the signal of either of the sensors during operation, the sensors on the left and right side were controlled separately. That is, the ground connection of the phototransistor portion of the optoelectronic components were separated between left and right. As such, six sensors on the left were connected to one transistor (NPN 2SC1815, Central Semiconductor Corp, US), and the ground connection of the six on the right to another transistor (Figure 6.2b). These transistors served as switches, alternating between HIGH-LOW states via connection to digital pins on an Arduino Mega Board. This meant that the left and right-side optoelectronic sensors on the strips alternate between the on and off state, so that both sensors are never on in the same instance. This ensures that all light reflected into the phototransistor belongs to the same optoelectronic sensor as the emitting sensor. Another advantage of this switching is that it reduces the power consumption by half, compared to if the full strip of sensors was powered. As such, for the two sensors strips that are used for two robotic segments, 24 sensors operate at a safe low level of power, allowing for more potential for integration into different continuum robot applications. For the reading of all the sensors' outputs, the AD7490 (Analog Devices, 16-Channel, 1 MSPS, 12-Bit ADC, MA, US) chip is used, using SPI communication with the Arduino Mega Board. As such, by using just a few ADC channels, all optoelectronic sensor signals can be read, for a possibility of up to three flexible PCB strips. Although depending on the intensity of light, and load of the phototransistor, the frequency response of the optoelectronic sensor (NJL5901R-2, New Japan Radio, Tokyo, Japan) is in the range of 8.8 kHz - 16.7 kHz. Along with the maximum switching frequency of the Arduino Mega at 16MHz, this ensures suitability for data acquisition for up to three optoelectronic PCB strips (switching six times to read a set of six optoelectronic sensors), at a fast-sampling rate, for real-time motion and shape detection.

6.3 Development of Experiment Platforms for the Two-Segment Tendon Actuated Robot

6.3.1 Sensor Integration into two segment robotic manipulator

The design of the tendon-actuated robot incorporated six DC motors (Dynamixel XL430-W250T, ROBOTIS, Seoul, Korea), three per actuated segment. For one robotic segment, the three motors were used to operate three wire tendons. To validate the sensing principle of the new shape-sensing mechanism, six consecutive units were employed as a single segment, depicted in Figure 6.1a, with the integrated flexible sensor circuit displayed in Figure 6.1b.

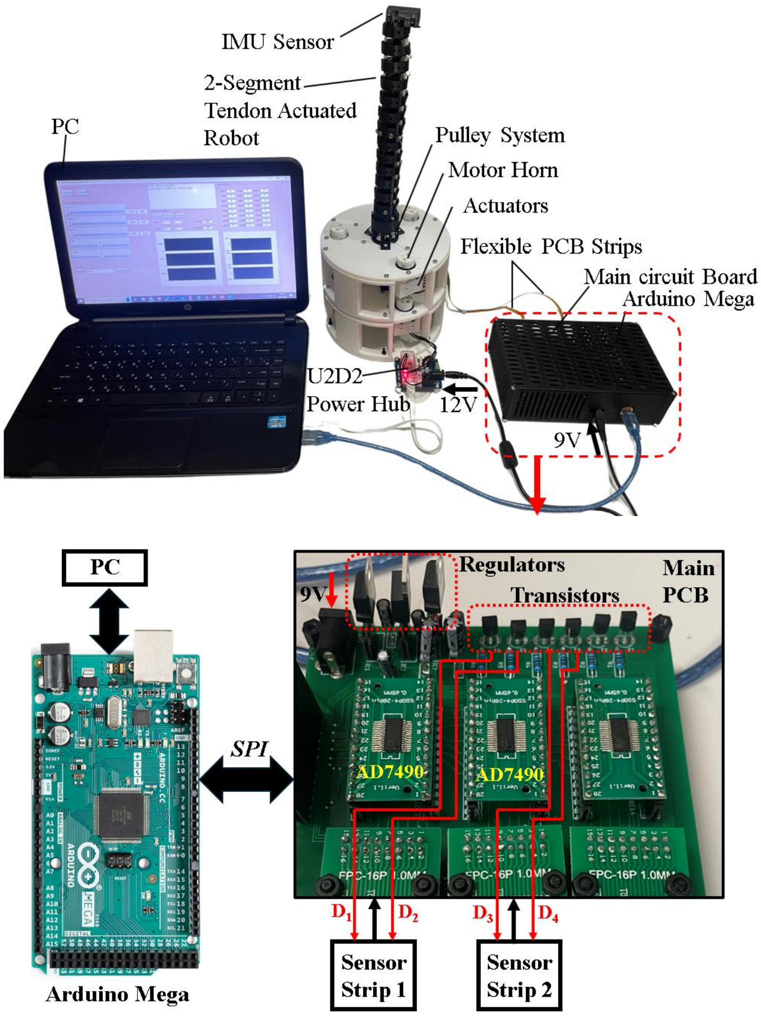

Figure 6.3 System overview for the experimental platform of the tendon actuated robot prototype.

Twelve sensors in total were distributed across the six units, with two sensors allocated to each unit. These units were interconnected using spherical bearings (INA GE6-DO 6mm Bore Spherical Bearing, 14mm O.D, Schaeffler, Germany) to form a ball joint, each unit measuring 22 mm in diameter and 10 mm in height. Each unit contained a convex reflector with a central shaft that was inserted into the spherical bearing bore. Each unit accommodated sets of three springs (6 mm height) to restrict torsional motion. The tendons were wound around pulleys and attached to the motor horns of each DC servo motor at the base actuating platform (Figure 6.3), enabling actuation in both pitch and roll orientations. To install the optoelectronic PCB strip, shown in Figure 6.1, the sections of the PCB housing the sensor pairs were glued to curved plastic supports (Figure 6.1c), and they were fixed along the side of the robotic structure at each unit. Additionally, a frame was mounted on the top unit to accommodate the IMU sensor (LPMS B2, LP-RESEARCH Inc, Tokyo, Japan) (Figure 6.3). All the experimental platform components were designed using CAD software (Onshape) and were 3D printed using white and black PLA (Polylactic Acid) plastic. The tendon actuated robot section was printed in black to reduce any chanced of scattering of ambient infrared light that may cause interference. The convex reflector component was 3D printed using a UV Resin SLA 3D printer, employing a white coloured resin to achieve a high-resolution surface finish, maximizing reflectivity, and minimising noise in the sensor signal.

For motion control, software developed in Python facilitated real-time motor control, optoelectronic sensor recordings, and IMU sensor recordings. Motion was achieved by selecting a target orientation for the top unit and utilising a vector-based model to calculate the necessary tendon lengths for conversion to three target motor positions. As the three motors moved simultaneously, each pulled a tendon wire over the pulley, enabling continuous motion per segment.

The motors were powered at 12 V, using a U2D2 (ROBOTIS) power hub for communication. The main circuit board is fitted at the base (Figure 6.3). While it is designed to connect to three flexible optoelectronic sensor strips, only two flexible PCB strips are connected as two robotic segments are used. Each flexible PCB strip, housing 12 sensors, is read using an AD7490 chip

(Analog Devices, Unites States) (16-Channel, 1 MSPS, 12-Bit ADC, MA, US), using SPI protocol communication. This vastly simplifies the amount of electrical wiring required and simplifies the system design. The main circuit board is powered using an external 9V Supply. On the main circuit board, one voltage regulator (L7805CV, STMicroelectronics, Switzerland) supplies 5V to the flexible sensor strips, while another two 2.5V (LM2937ET-2.5/NOPB, Texas Instruments, US) and 3.3V (LD1117V33C, STMicroelectronics, Switzerland) regulators supply power to the ADC chips. Two ADC chips are used, for two sensor strips. Amongst the ADC chips used, they share the CLK, DIN, and DOUT SPI lines, but each are connected to a separate CS line. These lines are connected to an Arduino Mega Board, and the sensor output is read via serial communication with the PC using the developed GUI interface (Python).

6.3.2 Calibration process

In order to calibrate each pair of sensors at every unit, the process outlined in Figure 6.4 was employed. This involved a new technique that streamlined the process of calibrating multiple sets of sensors along the tendon actuated robot. As shown in Figure 6.4, a linear, vertical sliding frame was designed. This sliding frame was designed to fit around the robotic structure. Three sets of ball bearings (diameter of 13 mm, 4 mm depth) were set equidistantly along the frame and fixed with screws. The bearings were able to slide into the grooves set into each unit of the robotic manipulator. In this way, all units encased within the sliding frame would become rigid, as the ball joints would become locked. Each pair of sensors is calibrated unit

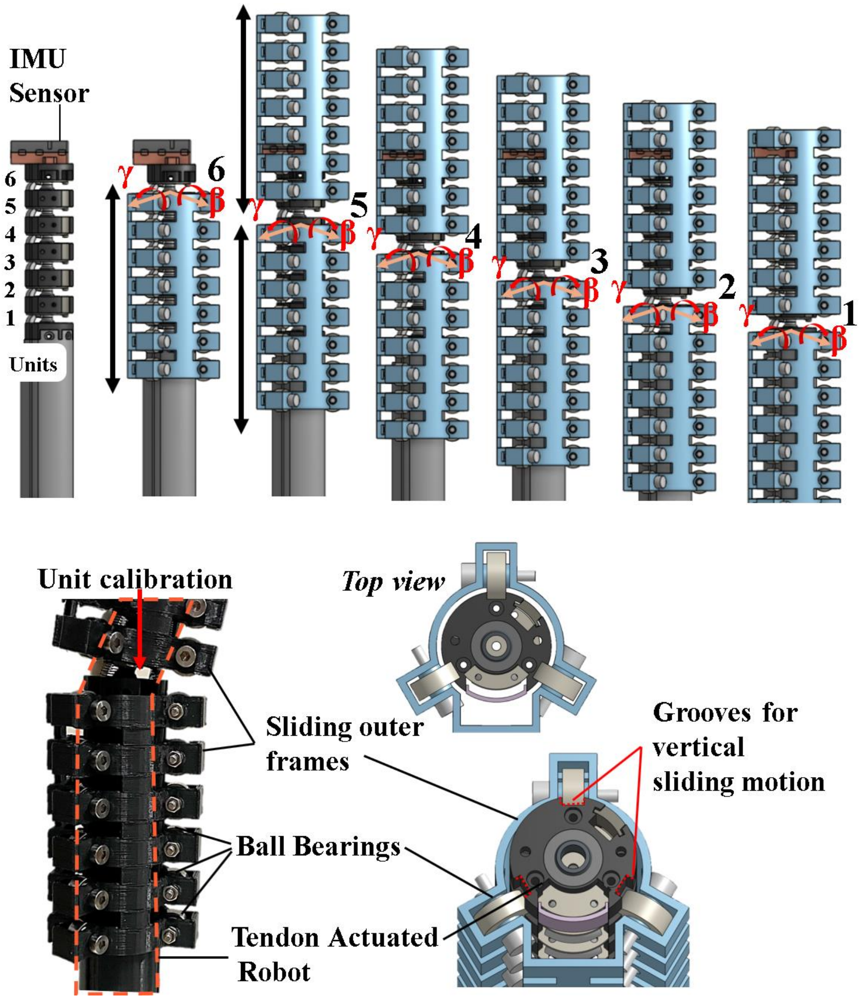

Figure. 6.4 Linear sliding calibration platform using bearings. Each of the six units is calibrated one by one. For this, the frames are slid over other units, allowing only the unit that is being calibrated to achieve motion in two orientations, with other units remaining rigid. For the calibration, motion pattern covering all angle ranges in pitch and roll is achieved, while pair of sensor data, and IMU data, is recorded.

by unit. For instance, to calibrate the two sensors on the top unit (6) as shown in Figure 6.4 on the top image, the sliding frame was secured onto the five lower units, restricting their motion while only allowing movement of the top unit (6) under tendon actuated control. A motion pattern covering all angles in both pitch and roll directions was generated in increments of 0.1° up to ±15° in these orientations. Subsequently, optoelectronic sensor voltage readings and IMU orientation data readings were recorded during this motion, providing a comprehensive dataset for each rotational unit, as illustrated in Figure 6.5.

This method compares to the previously used method for calibration [115], which involved using rigid components of various lengths, that were screwed around the structure of the robotic manipulator, in order to limit motion in sections of the robot, and allow motion limited to one unit, for calibration of sensors belonging to that unit. This was a laborious process, as each rigid component was screwed and unscrewed manually, and multiple components were required for each unit of calibration. However, the updated calibration process outlined prior (Figure 6.4), simplifies the process, as only two sliding frame components are required, that only move vertically, to allow calibration of a large number of units with ease, compared to the calibration process previously described in Chapter 5 that used multiple rigid frames of different lengths that could be attached along the body of the robotic manipulator.

Next, by using the IMU sensor (attached to top unit) data as ground truth, this data, along with the full set of voltage sensor readings were input into a non-linear regression algorithm [115] to determine coefficients that allowed the transformation of the sensor voltages into estimations of pitch and roll values (α and γ). The data was fed into MATLAB to generate a set of 8 coefficients per orientation estimation (Equation 6.1), (k_{1-8}) and (j_{1-8}), to map the two voltage values (v_1, v_2) to an estimate of pitch (γ^i) and roll (α^i).

This process was repeated for all six units (i = 1 to i = 6), as shown in the sequence at the top of Figure 6.4, for both segments of the tendon actuated robot prototype. In having an estimation of pitch and roll at each rotational unit, the total tip orientation, as well as the reconstructed shape of the full robotic manipulator could be modelled. Validation of the calibration results involved setting the full robot segment to move within its maximum angle range of ±180° in both orientations. Sensor voltages recorded during this motion were multiplied by the calibration coefficients to achieve estimated orientations, which were then compared to orientations provided by the IMU sensor. This is shown in Figure 6.7.

$$\gamma^i = k_1^i v_1^i + k_2^i v_2^i + k_3^i {v_1^i}^2 + k_4^i {v_2^i}^2 + k_5^i v_1^i v_2^i + k_6^i v_1^i {v_2^i}^2 + k_7^i v_2^i {v_1^i}^2 + k_8^i$$

$$\alpha^i = j_1^i v_1^i + j_2^i v_2^i + j_3^i {v_1^i}^2 + j_4^i {v_2^i}^2 + j_5^i v_1^i v_2^i + j_6^i v_1^i {v_2^i}^2 + j_7^i v_2^i {v_1^i}^2 + j_8^i$$

i = 1, 2, 3, 4, 5, 6 (6.1)

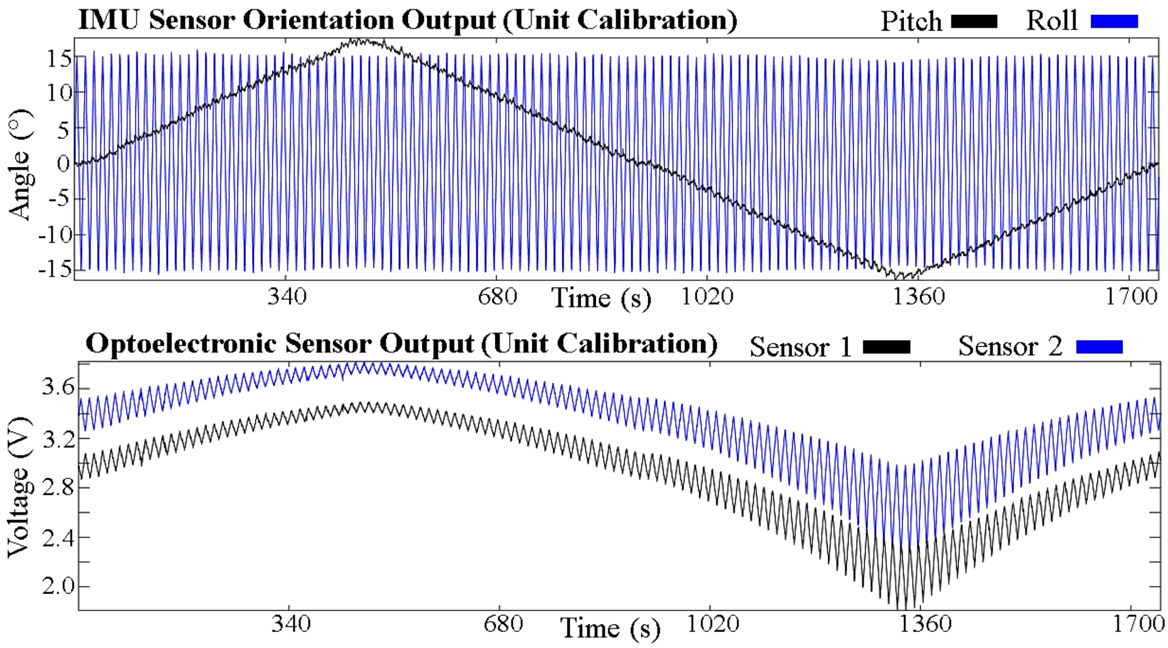

Figure. 6.5: Data collected during calibration of one unit, including IMU data, and two sets of optoelectronic sensor data

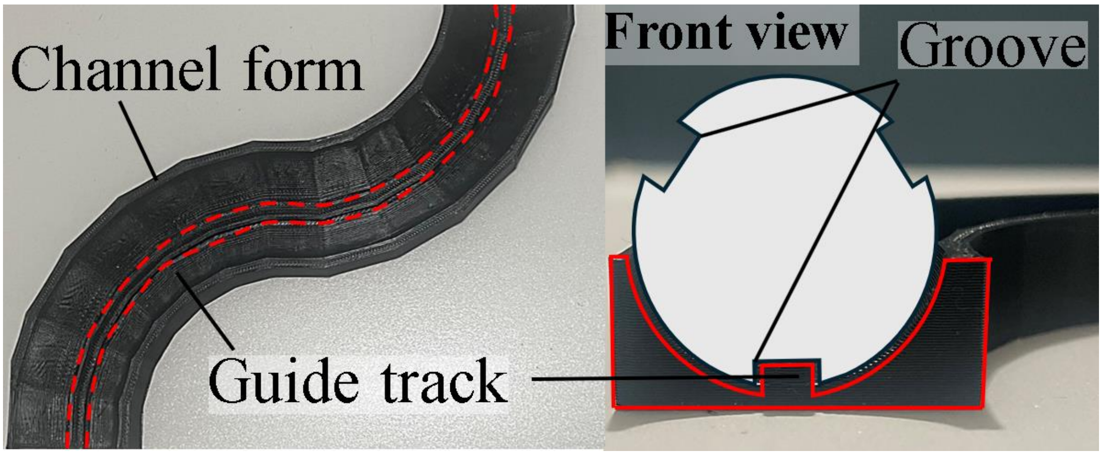

Figure 6.6: Design of channel forms for shape sensing validation experiments.

6.3.3 Shape Sensing Validation

Upon the validation of the calibration, another set of experiments involved designing more application-based tests to evaluate the shape sensing capabilities. The experiment design is shown in Figure 6.6. With the intended application of such continuum robots in a variety of fields, a series of channels were designed to mimic curved contours and pathways. Using the current prototype of the continuum robot, channels of various shapes were designed to encapsulate a cross section of the robotic structure. Using the existing grooves within the structure of the units of the robotic manipulator, these are guided along a track within the channel design. This ensures that the robotic manipulator maintains the expected shape along the channel path. These channel forms were designed using CAD, and 3D printed using black PLA, as shown in Figure 6.8, labelled (A-F). Three channel shapes are designed, with both pitch and roll channel orientations tested for each shape, which are labelled A, C, and E for the roll orientation, and B, D and F for the pitch orientation. These shape profiles are displayed in the Z-X plane and Z-Y plane accordingly. The robot segment is placed within each channel, and the full set of sensor data is measured at each shape. The sensor data is then transformed into estimations of the orientations of each of the 12 units. These estimations are then used to reconstruct the shape of the continuum robot, through a simple kinematic chain link model. This shape is compared to the known pre-set shape of the channel, as a test of shape detection. The results are shown in Figure 6.8, and Table 6.2.

6.4 Shape Sensing Calibration and Validation Results & Analysis

Figure 6.7 shows the results for the calibration validation experiment, with the error values shown in Table 6.1. For this, the whole robotic manipulator was set to move within its full bending range (±180 °), in both the pitch (Figure 6.7a) and roll (Figure 6.7b), continuously moving within this range for four cycles. The estimated orientation based on sensor values multiplied by the calibration coefficient matrix (blue) is compared to the actual tip orientation given by the IMU sensor (black). As shown in Table 6.1, the **average RMS tip error during the trajectory is 1.92° for pitch and 3.36° for roll,** with maximum tip errors measured as 5.65° and 7.28° respectively. Comparing this to the single segment version of this prototype shown in chapter 6, this had calibration validation mean RMS errors of 2.45° (0.77%) for pitch and 3.27° (0.21%) for roll. While this is slightly higher in value, this is like due to the longer length of robot, where accumulation of error is likely. As a measure of repeatability, the mean standard deviation for pitch orientation was 1.43° and 1.58° for roll, over four cycles of motion between ±180°. The calibration validation tested in this way demonstrated free motion, that is, free from constraint or obstruction. For this reason, the following channel tests described

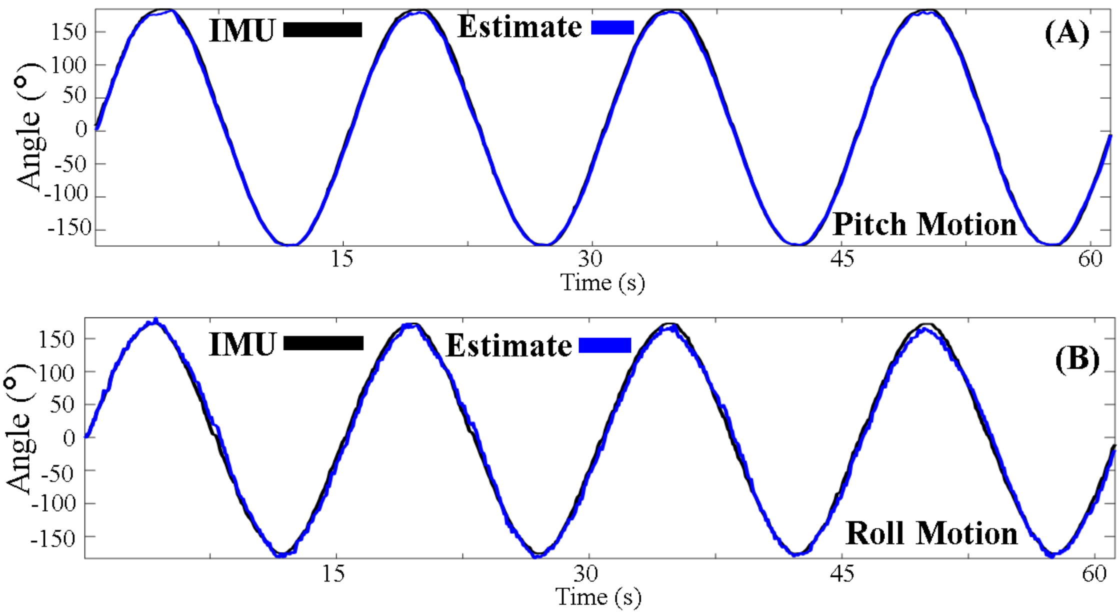

Figure. 6.7: Validation of calibration results for full motion of the two-segment robotic prototype (±180°). It compares the (pitch and roll) to the IMU measured orientation. Estimated tip-orientation is found through multiplying each pair of voltages by the calibration coefficients and summating the estimated link orientations along the full structure to get the estimated tip orientation.

TABLE 6.1: CALIBRATION VALIDATION ERROR

Orientation	% Error	RMS Tip Error (°)	Maximum Tip Error (°)
Pitch	0.78	1.92	5.65
Roll	1.23	3.46	7.28

in section 6.3.3 allowed more realistic evaluation of the shape sensing performance of the robotic segment, mimicking obstruction or external force applied on the robotic structure. The experiments for shape sensing validation is illustrated in Figure 6.8. Figure 6.8 shows the shape sensing validation of the robotic manipulator, using a series of preset curved channels. For both the pitch and roll orientations, this compares the estimated shape of the robot segments (blue), to the pre-curved channels of known curvature (red). The results are shown in Table 6.2, which shows the error values for each channel shape. Here, the tip position and orientation are compared to the expected value, as well as average shape error, which is the mean orientation error of each of the 12 units along the channel structure. The shape estimation based on the calibration matrix under these preset curves is relatively successful, with a maximum tip position error of 3.62 mm, and tip orientation error of 3.21°, and proving potential for further investigation into more specialized applications. Despite a large number of units, the summation of error to the tip is relatively low. This may in part be owing to the elimination of sensor interference by the use of the power switching circuit, and this shows prospects for further development.

TABLE 6.2: SHAPE SENSING VALIDATION ERRORS

Shape		Tip Position Error (mm)	Tip Orientation Error (°)	Average shape Error (°)
Roll	**A**	2.96	1.23	0.10
	C	3.15	2.25	0.18
	E	2.32	1.05	0.08
Pitch	**B**	1.01	2.37	0.20
	D	3.62	1.45	0.12
	F	3.21	3.13	0.26

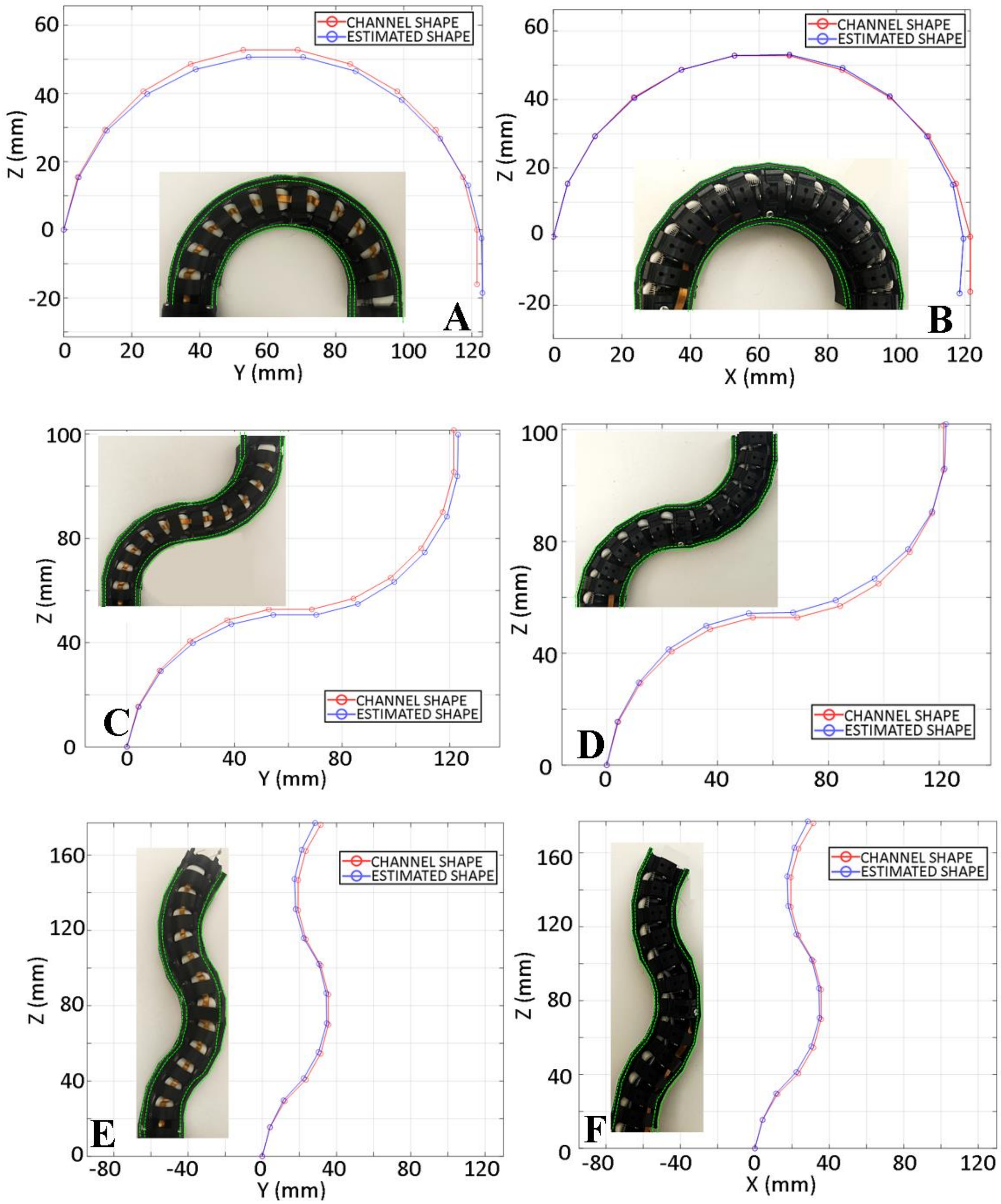

Figure 6.8: Shape sensing validation tests using pre-set curved frames, to evaluate estimated shape through chain link model and constant curvature model estimations. Boundaries of the channel frames are highlighted in green.

6.5 Conclusion

This work has demonstrated the development of a two-segment tendon actuating robot with integrated optoelectronic shape sensing. Through improved mechanical design, including reduction of friction of the tendon wires by introducing low friction tubes along the routing paths, as well as a simplified and robust calibration process, the resulting calibration matrix is used to transform the sensor voltage values to estimated orientations is robust and able to estimate shape and tip position and orientation within a degree of accuracy. This was also supported by reducing signal interference between sensor pairs during motion, by introducing a power switching circuit. Overall, this work has shown a viable option for integration into continuum robots for real time shape sensing. As the presented system was a prototype, this meant that the overall size and diameter of the continuum robot was larger than that of many specialised robots used in various industries. While in areas such as in minimally invasive surgery, diameters of utilised continuum robots are smaller, and fall within the range of 0.7-30 mm [19], whereas other applications such as turbine and engine inspection, the diameters can be larger, for example up to 70 mm [20]. Future work will aim to miniaturise the system so that a more comprehensive study may be undertaken, including closed loop position control for the targeted application.

CHAPTER 7: CONCLUSION AND FUTURE WORK

7.1 Thesis Conclusion

Overall, this thesis accomplishes its aims outlined in Chapter 1. These were to discover solutions for a novel shape sensing method for continuum robots that was simple, cheap, miniaturised, adaptable, while also overcoming some of the limitations of standard shape sensing techniques - combining these qualities to develop robotic applications that can utilise this optimised method of shape sensing. Another aim was to demonstrate how any optoelectronic sensor can be integrated in various configurations into robotic applications, from simple joint angle sensors to multi-segmented flexible robots and identify how to optimise the sensor response various design parameters, to improve sensitivity and measurement range. This was completed by achieving the outlined objectives, and through this a number of novel contributions to knowledge in the field of robotic shape seeing have been achieved:

1. A study of the behaviour of optoelectronic sensors, more specifically photo-reflective sensors was carried out. This included extensive experimental studies to explore the effect of various circuit properties (LED and PT resistors), reflective surface properties such as colour (reflectivity) and shape, as well as linear and lateral proximity to a reflector as well as angle of a reflective surface to the photo-reflective sensor. With this vast set of data, one can easily extract the required design parameters or circuit properties to achieve the desired optoelectronic sensor response, for a variety of applications, from simple proximity sensing, joint angle sensing, or multidimensional shape sensing.
2. An original gaussian light intensity theoretical mathematical model was developed for the optoelectronic sensors, based on a series of models developed for fibre optics. This was adapted to a photo-reflective sensor against a reflective surface, to estimate the flux collected by the sensor depending on various parameters such as surface

proximity, angle, or reflectivity. The model was validated against experimental values comparing different design parameters and was also validated against a one-axis joint angle sensor. It most cases, the results closely approximated the real experimental data, although it needs further development to account for certain quantities such as resistance values. Nevertheless, based on this one may use the mathematical model to propose further optoelectronic sensing configuration beyond that demonstrated in the experimental sensor study and establish feasibility for any proposed robotic design utilising optoelectronic sensing.

3. A single link one-axis joint angle sensor was developed, comprising a simple finger-like link structure, for robotic application. It can be simply integrated directly into robotic joint structures, have a large voltage variation without an amplifier and with low level noise, and offer simple fabrication at considerably low cost in comparison.
4. A single segment tendon actuated robot was constructed, integrating a novel optoelectronic shape sensing technique using three optoelectronic sensors per unit of the segment. A flat surface of the consecutive unit was used as the reflector. Each set of three sensors were used to estimate bending in two orientations. A novel calibration technique, involving calibrating three sensors per unit successively along the structure of the robotic segment using a motorised motion pattern ensured improved calculation of a calibration matrix, with improved orientation estimation results when compared to an IMU sensor. Compared to some other robotic structures integrating shape sensing, results showed comparable performance, with maximum RMSE of 3.23° with non-linear fitting in tip orientation estimation.
5. An experimental study was completed exploring how to improve joint angle sensor performance by adapting the geometry of the reflective surface into a curved surface. The technique to achieve the desired response is explored in this study in terms of sensor sensitivity and range, through the design of multiple curved surface reflectors. A 4-link structure is developed to evaluate this concept, and results showed feasibility in use of this technique for planar shape sensing. Results show improved performance

in sensing range compared to other joint angle sensors, demonstrating a case with 140° measurement range with 3.5V voltage variation. This inspired the application of curved reflectors in continuum robots for measuring orientation in three dimensions, beyond the planar case.

6. Another single segment tendon actuated robot was developed using a novel optoelectronic shape sensing technique based on the use of a curved convex spherical reflector. Sensors per unit were reduced to two using this configuration, to measure two orientations in three-dimensional space. Results showed comparable results, with a maximum RMS error of 3.27° for tip orientation estimation.
7. A two-segment tendon actuated robot was created integrating the spherical-reflector based optoelectronic shape sensing. Improved performance through robot design modifications, circuit modifications (power switching), and flexible PCB design was achieved. A power switching circuit allowed elimination of interference of signals between each set of sensors, leading to more accurate calibration and shape sensing estimation.

In all, this shape sensing technique overcomes some of the limitations of existing shape-sensing techniques. It offers sensing that is non-contact, and based purely on light intensity detection, meaning the sensors are not affected by material properties (they do not directly measure quantities such as stretch or strain) or load limitations and have a hysteresis of almost zero, meaning calibration of the sensors in free space can remain intact in almost any scenario, regardless of curvature, load, or external forced applied. Real time sensing can be achieved through the sensors' high sampling rate, which do not require an amplifier. Photo-reflective sensors are miniature, easy to integrate, and low is cost.

7.2 Future Works

The next steps would be to focus on a specified application, as this will more clearly provide the guidelines, such as exact sensing range, accuracy, and dimensions required for a flexible manipulator with integrated optoelectronic shape sensing. More specialised manufacturing of the components, especially the convex reflector could be explored. The design was initially made simple, and sectioned from part of a sphere, and therefore it is expected that many machining tools would be able to realise this design, so that it may be tested further with a range of materials. Sensing range and sensitivity may be improved with the use of highly polished or reflective metals for the reflector, as this would boost reflectance rate and reduce scattering. Another aspect of the shape sensing that may be explored is more dynamic shape sensing through more realistic phantom experiments, through the u se of for example constantly changing channel shapes, for real time shape sensing during actuation, as within the scope of this project, only static conditions for the channel shape sensing tests were evaluated. A further simplified calibration technique for multiple optoelectronic sensors integrated into longer lengths of a continuum manipulator may be explored, using a fully automated technique with the aid of an external robot arm. In all, this work has provided proof of concept through the preliminary groundwork, including theory, experimental platforms, and test results of various prototypes, showing potential for further development of optoelectronic shape sensing.

REFERENCES

[1] "Monarch platform | J&J medtech." [Online]. Available: https://www.jnjmedtech.com/en-US/product-family/monarch

[2] T. Da Veiga *et al.*, "Challenges of continuum robots in clinical context: A review," *Progress in Biomedical Engineering*, vol. 2, no. 3, 2020, doi: 10.1088/2516-1091/ab9f41.

[3] C. Lapusan, O. Hancu, and C. Rad, "Shape Sensing of Hyper-Redundant Robots Using an AHRS IMU Sensor Network," *Sensors*, vol. 22, no. 1, 2022, doi: 10.3390/s22010373.

[4] J. Hughes, F. Stella, C. Della Santina, and D. Rus, "Sensing Soft Robot Shape Using IMUs: An Experimental Investigation," *Springer Proceedings in Advanced Robotics*, vol. 19, no. March, pp. 543–552, 2021, doi: 10.1007/978-3-030-71151-1_48.

[5] Zhang Zhiqiang, Shang Jianzhong, Seneci Carlo, and Yang Guang-Zhong, "Snake Robot Shape Sensing Using Micro-inertial Sensors," Tokyo: IEEE/RSJ International Conference on Intelligent Robots and Systems (IROS), Nov. 2013.

[6] T. Lisini Baldi, F. Farina, A. Garulli, A. Giannitrapani, and D. Prattichizzo, "Upper Body Pose Estimation Using Wearable Inertial Sensors and Multiplicative Kalman Filter," *IEEE Sens J*, vol. 20, no. 1, pp. 492–500, Jan. 2020, doi: 10.1109/JSEN.2019.2940612.

[7] M. S. Sofla, M. J. Sadigh, and M. Zareinejad, "Shape estimation of a large workspace continuum manipulator with fusion of inertial sensors," *Mechatronics*, vol. 80, no. October, p. 102684, 2021, doi: 10.1016/j.mechatronics.2021.102684.

[8] M. El-Gohary and J. McNames, "Human Joint Angle Estimation with Inertial Sensors and Validation with A Robot Arm," *IEEE Trans Biomed Eng*, vol. 62, no. 7, pp. 1759–1767, 2015, doi: 10.1109/TBME.2015.2403368.

[9] H. Guo *et al.*, "Continuum robot shape estimation using permanent magnets and magnetic sensors," *Sens Actuators A Phys*, vol. 285, pp. 519–530, 2019, doi: 10.1016/j.sna.2018.11.030.

[10] T. Baaij *et al.*, "Learning 3D shape proprioception for continuum soft robots with multiple magnetic sensors," *Soft Matter*, vol. 19, no. 1, pp. 44–56, 2022, doi: 10.1039/d2sm00914e.

[11] T. Alam, F. Saidane, A. al Faisal, A. Khan, and G. Hossain, "Smart- textile strain sensor for human joint monitoring," *Sens Actuators A Phys*, vol. 341, Jul. 2022, doi: 10.1016/j.sna.2022.113587.

[12] J. W. Park, T. Kim, D. Kim, Y. Hong, and H. S. Gong, "Measurement of finger joint angle using stretchable carbon nanotube strain sensor," *PLoS One*, vol. 14, no. 11, Nov. 2019, doi: 10.1371/journal.pone.0225164.

[13] M. Xu, J. Qi, F. Li, and Y. Zhang, "Highly stretchable strain sensors with reduced graphene oxide sensing liquids for wearable electronics," *Nanoscale*, vol. 10, no. 11, pp. 5264–5271, 2018, doi: 10.1039/c7nr09022f.

[14] S. Kim, J. Lee, and B. Choi, "Stretching and twisting sensing with liquid-metal strain gauges printed on silicone elastomers," *IEEE Sens J*, vol. 15, no. 11, pp. 6077–6078, 2015, doi: 10.1109/JSEN.2015.2462314.

[15] H. Yan *et al.*, "Cable-Driven Continuum Robot Perception Using Skin-Like Hydrogel Sensors," *Adv Funct Mater*, vol. 32, no. 34, pp. 1–11, 2022, doi: 10.1002/adfm.202203241.

[16] S. C. Ryu and P. E. Dupont, "FBG-based shape sensing tubes for continuum robots," *Proc IEEE Int Conf Robot Autom*, pp. 3531–3537, 2014, doi: 10.1109/ICRA.2014.6907368.

[17] Y. Lu, W. Chen, Z. Chen, J. Zhou, and Y. H. Liu, "FBG-Based Variable-Length Estimation for Shape Sensing of Extensible Soft Robotic Manipulators," *IEEE International Conference on Intelligent Robots and Systems*, vol. 2022-Octob, pp. 10051–10058, 2022, doi: 10.1109/IROS47612.2022.9981501.

[18] R. J. Roesthuis and S. Misra, "Steering of Multisegment Continuum Manipulators Using Rigid-Link Modeling and FBG-Based Shape Sensing," *IEEE Transactions on Robotics*, vol. 32, no. 2, pp. 372–382, 2016, doi: 10.1109/TRO.2016.2527047.

[19] L. Zhang, J. Qian, Y. Zhang, and L. Shen, "On SDM/WDM FBG sensor net for shape detection of endoscope," *IEEE International Conference on Mechatronics and Automation, ICMA 2005*, no. July, pp. 1986–1991, 2005, doi: 10.1109/icma.2005.1626867.

[20] Z. Lunwei, Q. Jinwu, S. Linyong, and Z. Yanan, "FBG sensor devices for spatial shape detection of intelligent colonoscope," *Proc IEEE Int Conf Robot Autom*, vol. 2004, no. 1, pp. 835–840, 2004, doi: 10.1109/robot.2004.1307253.

[21] R. Xu, A. Yurkewich, and R. V. Patel, "Curvature, Torsion, and Force Sensing in Continuum Robots Using Helically Wrapped FBG Sensors," *IEEE Robot Autom Lett*, vol. 1, no. 2, pp. 1052–1059, 2016, doi: 10.1109/LRA.2016.2530867.

[22] I. Floris, J. M. Adam, P. A. Calderón, and S. Sales, "Fiber Optic Shape Sensors: A comprehensive review," *Opt Lasers Eng*, vol. 139, no. April, 2021, doi: 10.1016/j.optlaseng.2020.106508.

[23] "Inspection and Maintenance Robot Market Growth, Analysis, Scenario and Forecast 2030." [Online]. Available: https://www.snsinsider.com/reports/inspection-and-maintenance-robot-market-1364?trk=article-ssr-frontend-pulse_little-text-block

[24] "Medical Robotic Systems Market Size, Share Report, 2030." [Online]. Available: https://www.grandviewresearch.com/industry-analysis/medical-robotic-systems-market#:~:text=How big is the medical,USD 25.6 billion in 2023

[25] The Royal College of Surgeons of England, "Future of Surgery Report," 2018.

[26] L. A. DiDomenico, L. A. Ford, C. B. Jones, C. Krettek, and J. M. Schuberth, "Minimally Invasive Surgery," *Foot Ankle Spec*, vol. 5, no. 3, pp. 201–207, 2012, doi: 10.1177/1938640012445565.

[27] J. Burgner-Kahrs, D. C. Rucker, and H. Choset, “Continuum Robots for Medical Applications: A Survey,” *IEEE Transactions on Robotics*, vol. 31, no. 6, pp. 1261–1280, 2015, doi: 10.1109/TRO.2015.2489500.

[28] M. Russo *et al.*, “Continuum Robots: An Overview,” *Advanced Intelligent Systems*, vol. 5, no. 5, 2023, doi: 10.1002/aisy.202200367.

[29] P. J. Sincak *et al.*, “Sensing of Continuum Robots: A Review,” *Sensors*, vol. 24, no. 4, pp. 1–21, 2024, doi: 10.3390/s24041311.

[30] M. D. M. Kutzer, S. M. Segreti, C. Y. Brown, R. H. Taylor, S. C. Mears, and M. Armand, “Design of a new cable-driven manipulator with a large open lumen: Preliminary applications in the minimally-invasive removal of osteolysis,” *Proc IEEE Int Conf Robot Autom*, no. Dm, pp. 2913–2920, 2011, doi: 10.1109/ICRA.2011.5980285.

[31] D. B. Camarillo, C. F. Milne, C. R. Carlson, M. R. Zinn, and J. K. Salisbury, “Mechanics modeling of tendon-driven continuum manipulators,” *IEEE Transactions on Robotics*, vol. 24, no. 6, pp. 1262–1273, 2008, doi: 10.1109/TRO.2008.2002311.

[32] N. Simaan *et al.*, “Design and Integration of a Telerobotic System for Minimally Invasive Surgery of the Throat,” *International Journal of Robotics Research*, vol. 28, no. 9, pp. 1134–1153, 2009, doi: 10.1177/0278364908104278.

[33] Y. J. Kim, S. Cheng, S. Kim, and K. Iagnemma, “A stiffness-adjustable hyperredundant manipulator using a variable neutral-line mechanism for minimally invasive surgery,” *IEEE Transactions on Robotics*, vol. 30, no. 2, pp. 382–395, 2014, doi: 10.1109/TRO.2013.2287975.

[34] H. S. Yoon, H. J. Cha, J. Chung, and B. J. Yi, “Compact design of a dual master-slave system for maxillary sinus surgery,” *IEEE International Conference on Intelligent Robots and Systems*, pp. 5027–5032, 2013, doi: 10.1109/IROS.2013.6697083.

[35] P. Dario *et al.*, “A novel mechatronic tool for computer-assisted arthroscopy,” *IEEE Transactions on Information Technology in Biomedicine*, vol. 4, no. 1, pp. 15–29, 2000, doi: 10.1109/4233.826855.

[36] L. Wu, S. Song, K. Wu, C. M. Lim, and H. Ren, “Development of a compact continuum tubular robotic system for nasopharyngeal biopsy,” *Med Biol Eng Comput*, vol. 55, no. 3, pp. 403–417, 2017, doi: 10.1007/s11517-016-1514-9.

[37] L. Wu, B. L. W. Tan, and H. Ren, “Prototype development of a hand-held robotic light pipe for intraocular procedures,” *2015 IEEE International Conference on Robotics and Biomimetics, IEEE-ROBIO 2015*, pp. 368–373, 2015, doi: 10.1109/ROBIO.2015.7418795.

[38] E. J. Butler *et al.*, “Robotic neuro-emdoscope with concentric tube augmentation,” *IEEE International Conference on Intelligent Robots and Systems*, pp. 2941–2946, 2012, doi: 10.1109/IROS.2012.6386022.

[39] R. J. Webster and B. A. Jones, "Design and kinematic modeling of constant curvature continuum robots: A review," *International Journal of Robotics Research*, vol. 29, no. 13, pp. 1661–1683, 2010, doi: 10.1177/0278364910368147.

[40] E. Amanov, T. D. Nguyen, and J. Burgner-Kahrs, "Tendon-driven continuum robots with extensible sections—A model-based evaluation of path-following motions," *International Journal of Robotics Research*, pp. 1–17, 2019, doi: 10.1177/0278364919886047.

[41] D. Trivedi and C. D. Rahn, "Model-based shape estimation for soft robotic manipulators: The planar case," *J Mech Robot*, vol. 6, no. 2, 2014, doi: 10.1115/1.4026338.

[42] N. J. van de Berg, J. Dankelman, and J. J. van den Dobbelsteen, "Design of an actively controlled steerable needle with tendon actuation and FBG-based shape sensing," *Med Eng Phys*, vol. 37, no. 6, pp. 617–622, 2015, doi: 10.1016/j.medengphy.2015.03.016.

[43] B. L. Gray, "A Review of Magnetic Composite Polymers Applied to Microfluidic Devices," *J Electrochem Soc*, vol. 161, no. 2, pp. B3173–B3183, 2014, doi: 10.1149/2.023402jes.

[44] K. Ikuta, Y. Matsuda, D. Yajima, and Y. Ota, "Pressure pulse drive: A control method for the precise bending of hydraulic active catheters," *IEEE/ASME Transactions on Mechatronics*, vol. 17, no. 5, pp. 876–883, 2012, doi: 10.1109/TMECH.2011.2138711.

[45] J. Walker *et al.*, "Soft robotics: A review of recent developments of pneumatic soft actuators," *Actuators*, vol. 9, no. 1, pp. 1–27, 2020, doi: 10.3390/act9010003.

[46] D. P. Noonan, V. Vitiello, J. Shang, C. J. Payne, and G. Z. Yang, "A modular, mechatronic joint design for a flexible access platform for MIS," *IEEE International Conference on Intelligent Robots and Systems*, pp. 949–954, 2011, doi: 10.1109/IROS.2011.6048575.

[47] J. Shang *et al.*, "An articulated universal joint based flexible access robot for minimally invasive surgery," *Proc IEEE Int Conf Robot Autom*, vol. 1, pp. 1147–1152, 2011, doi: 10.1109/ICRA.2011.5980261.

[48] S. K. Sahu, C. Sozer, B. Rosa, I. Tamadon, P. Renaud, and A. Menciassi, "Shape Reconstruction Processes for Interventional Application Devices: State of the Art, Progress, and Future Directions," *Front Robot AI*, vol. 8, no. November, pp. 1–26, 2021, doi: 10.3389/frobt.2021.758411.

[49] "Intuitive - DaVinci system." [Online]. Available: https://www.intuitive.com/en-us/products-and-services/da-vinci/vision

[50] "Auris Monarch Paltform," 2020.

[51] M. Patil, P. Gharde, K. Reddy, and K. Nayak, "Comparative Analysis of Laparoscopic Versus Open Procedures in Specific General Surgical Interventions," *Cureus*, vol. 16, no. 2, pp. 1–6, 2024, doi: 10.7759/cureus.54433.

[52] J. R. Romanelli and D. B. Earle, "Single-port laparoscopic surgery: An overview," *Surg Endosc*, vol. 23, no. 7, pp. 1419–1427, 2009, doi: 10.1007/s00464-009-0463-x.

[53] P. Gomes, *Medical robotics: Minimally invasive surgery*. 2012. doi: 10.1533/9780857097392.

[54] M. Amanzadeh, S. M. Aminossadati, M. S. Kizil, and A. D. Rakić, "Recent developments in fibre optic shape sensing," *Measurement (Lond)*, vol. 128, no. April, pp. 119–137, 2018, doi: 10.1016/j.measurement.2018.06.034.

[55] A. Farvardin, R. J. Murphy, R. B. Grupp, I. Iordachita, and M. Armand, "Towards real-Time shape sensing of continuum manipulators utilizing fiber Bragg grating sensors," *Proceedings of the IEEE RAS and EMBS International Conference on Biomedical Robotics and Biomechatronics*, vol. 2016-July, pp. 1180–1185, 2016, doi: 10.1109/BIOROB.2016.7523791.

[56] M. Antico *et al.*, "Ultrasound guidance in minimally invasive robotic procedures," *Med Image Anal*, vol. 54, pp. 149–167, 2019, doi: 10.1016/j.media.2019.01.002.

[57] C. Shi, S. Giannarou, S. L. Lee, and G. Z. Yang, "Simultaneous catheter and environment modeling for Trans-catheter Aortic Valve Implantation," *IEEE International Conference on Intelligent Robots and Systems*, no. Iros, pp. 2024–2029, 2014, doi: 10.1109/IROS.2014.6942832.

[58] Y. F. Wang, D. R. Uecker, and Y. Wang, "A new framework for vision-enabled and robotically assisted minimally invasive surgery," *Computerized Medical Imaging and Graphics*, vol. 22, no. 6, pp. 429–437, 1998, doi: 10.1016/S0895-6111(98)00052-4.

[59] S. Song, Z. Li, M. Q. H. Meng, H. Yu, and H. Ren, "Real-time shape estimation for wire-driven flexible robots with multiple bending sections based on quadratic Bézier curves," *IEEE Sens J*, vol. 15, no. 11, pp. 6326–6334, 2015, doi: 10.1109/JSEN.2015.2456181.

[60] S. Elayaperumal *et al.*, "Autonomous real-time interventional scan plane control with a 3-d shape-sensing needle," *IEEE Trans Med Imaging*, vol. 33, no. 11, pp. 2128–2139, 2014, doi: 10.1109/TMI.2014.2332354.

[61] A. M. Franz, T. Haidegger, W. Birkfellner, K. Cleary, T. M. Peters, and L. Maier-Hein, "Electromagnetic tracking in medicine -A review of technology, validation, and applications," *IEEE Trans Med Imaging*, vol. 33, no. 8, pp. 1702–1725, 2014, doi: 10.1109/TMI.2014.2321777.

[62] S. Ozel *et al.*, "A composite soft bending actuation module with integrated curvature sensing," *Proc IEEE Int Conf Robot Autom*, vol. 2016-June, pp. 4963–4968, 2016, doi: 10.1109/ICRA.2016.7487703.

[63] J. So *et al.*, "Shape Estimation of Soft Manipulator Using Stretchable Sensor," *Cyborg and Bionic Systems*, vol. 2021, 2021, doi: 10.34133/2021/9843894.

[64] A. I. Faisal, S. Majumder, T. Mondal, D. Cowan, S. Naseh, and M. J. Deen, "Monitoring methods of human body joints: State-of-the-art and research challenges," *Sensors (Switzerland)*, vol. 19, no. 11, Jun. 2019, doi: 10.3390/s19112629.

[65] L. Yan, J. Hao, Z. Zhang, R. Liu, H. Yang, and C. Shi, "Curvature Estimation of Soft Grippers Based on a Novel Highly Stretchable Strain Sensor With Worm-Surface-Like Microstructures," *IEEE Sens J*, vol. 24, no. 4, pp. 4246–4257, 2024, doi: 10.1109/JSEN.2023.3343370.

[66] K. C. Galloway, Y. Chen, E. Templeton, B. Rife, I. S. Godage, and E. J. Barth, "Fiber Optic Shape Sensing for Soft Robotics," *Soft Robot*, vol. 6, no. 5, pp. 671–684, 2019, doi: 10.1089/soro.2018.0131.

[67] A. Schmitz, A. J. Thompson, P. Berthet-Rayne, C. A. Seneci, P. Wisanuvej, and G. Z. Yang, "Shape sensing of miniature snake-like robots using optical fibers," *IEEE International Conference on Intelligent Robots and Systems*, vol. 2017-Septe, pp. 947–952, 2017, doi: 10.1109/IROS.2017.8202259.

[68] F. Al Jaber and K. Althoefer, "Towards creating a flexible shape senor for soft robots," *2018 IEEE International Conference on Soft Robotics, RoboSoft 2018*, no. 1, pp. 114–119, 2018, doi: 10.1109/ROBOSOFT.2018.8404906.

[69] S. Sareh, Y. Noh, M. Li, T. Ranzani, H. Liu, and K. Althoefer, "Macrobend optical sensing for pose measurement in soft robot arms," *Smart Mater Struct*, 2015, doi: 10.1088/0964-1726/24/12/125024.

[70] "Keyence Product," 2020, [Online]. Available: https://www.radwell.co.uk/en-GB/Search/Advanced?TopCategoryId=61&CategoryId=20&Manufacturer=KEYENCE CORP

[71] T. C. Searle, K. Althoefer, L. Seneviratne, and H. Liu, "An optical curvature sensor for flexible manipulators," *Proc IEEE Int Conf Robot Autom*, pp. 4415–4420, 2013, doi: 10.1109/ICRA.2013.6631203.

[72] M. P. Farook Afsari, "(12) United States Patent Date of Patent :," *System and Method for Programming a Weighing Scale Usinga Key Signal To Enter a Programming Mode*, vol. 1, no. 12, p. 14, 2009.

[73] Y. L. Park *et al.*, "Real-time estimation of 3-D needle shape and deflection for MRI-guided interventions," *IEEE/ASME Transactions on Mechatronics*, vol. 15, no. 6, pp. 906–915, 2010, doi: 10.1109/TMECH.2010.2080360.

[74] K. R. Henken, J. Dankelman, J. J. Van Den Dobbelsteen, L. K. Cheng, and M. S. Van Der Heiden, "Error analysis of FBG-based shape sensors for medical needle tracking," *IEEE/ASME Transactions on Mechatronics*, vol. 19, no. 5, pp. 1523–1531, 2014, doi: 10.1109/TMECH.2013.2287764.

[75] K. Henken, D. Van Gerwen, J. Dankelman, and J. Van Den Dobbelsteen, "Accuracy of needle position measurements using fiber Bragg gratings," *Minimally Invasive Therapy and Allied Technologies*, vol. 21, no. 6, pp. 408–414, 2012, doi: 10.3109/13645706.2012.666251.

[76] R. J. Roesthuis, S. Janssen, and S. Misra, "On using an array of fiber Bragg grating sensors for closed-loop control of flexible minimally invasive surgical instruments," *IEEE International Conference on Intelligent Robots and Systems*, pp. 2545–2551, 2013, doi: 10.1109/IROS.2013.6696715.

[77] R. J. Roesthuis, M. Kemp, J. J. Van Den Dobbelsteen, and S. Misra, “Three-dimensional needle shape reconstruction using an array of fiber bragg grating sensors,” *IEEE/ASME Transactions on Mechatronics*, vol. 19, no. 4, pp. 1115–1126, 2014, doi: 10.1109/TMECH.2013.2269836.

[78] B. Kim, J. Ha, F. C. Park, and P. E. Dupont, “Optimizing curvature sensor placement for fast, accurate shape sensing of continuum robots,” *Proc IEEE Int Conf Robot Autom*, pp. 5374–5379, 2014, doi: 10.1109/ICRA.2014.6907649.

[79] C. Ledermann, H. Pauer, O. Weede, and H. Woern, “Simulation tool and optimization for 3D shape sensors based on Fiber Bragg gratings,” pp. 195–200, 2013.

[80] H. Liu *et al.*, “Shape Tracking of a Dexterous Continuum Manipulator Utilizing Two Large Deflection Shape Sensors,” *IEEE Sens J*, vol. 15, no. 10, pp. 5494–5503, 2015, doi: 10.1109/JSEN.2015.2442266.

[81] H. Liu, A. Farvardin, S. A. Pedram, I. Iordachita, R. H. Taylor, and M. Armand, “Large deflection shape sensing of a continuum manipulator for minimally-invasive surgery,” *Proc IEEE Int Conf Robot Autom*, vol. 2015-June, no. June, pp. 201–206, 2015, doi: 10.1109/ICRA.2015.7139000.

[82] J. P. Moore and M. D. Rogge, “Shape sensing using multi-core fiber optic cable and parametric curve solutions,” *Opt Express*, vol. 20, no. 3, p. 2967, 2012, doi: 10.1364/oe.20.002967.

[83] D. Grobnic, C. Hnatovsky, S. Dedyulin, R. B. Walker, H. Ding, and S. J. Mihailov, “Fiber bragg grating wavelength drift in long-term high temperature annealing,” *Sensors*, vol. 21, no. 4, pp. 1–29, 2021, doi: 10.3390/s21041454.

[84] R. Li, Y. Tan, Y. Chen, L. Hong, and Z. Zhou, “Investigation of sensitivity enhancing and temperature compensation for fiber Bragg grating (FBG)-based strain sensor,” *Optical Fiber Technology*, vol. 48, no. January, pp. 199–206, 2019, doi: 10.1016/j.yofte.2019.01.009.

[85] J. H. Benjamin Koh, T. Jeong, S. Han, W. Li, K. Rhode, and Y. Noh, “Optoelectronic Sensor-based Shape Sensing Approach for Flexible Manipulators,” *Proceedings of the Annual International Conference of the IEEE Engineering in Medicine and Biology Society, EMBS*, pp. 3199–3203, 2019, doi: 10.1109/EMBC.2019.8856882.

[86] H. A. Wurdemann *et al.*, “Embedded electro-conductive yarn for shape sensing of soft robotic manipulators,” in *Proceedings of the Annual International Conference of the IEEE Engineering in Medicine and Biology Society, EMBS*, 2015. doi: 10.1109/EMBC.2015.7320255.

[87] H. Wang, M. Totaro, and L. Beccai, “Toward Perceptive Soft Robots: Progress and Challenges,” 2018. doi: 10.1002/advs.201800541.

[88] M. Cianchetti, F. Renda, A. Licofonte, and C. Laschi, “Sensorization of continuum soft robots for reconstructing their spatial configuration,” in *Proceedings of the IEEE RAS and EMBS International Conference on Biomedical Robotics and Biomechatronics*, 2012. doi: 10.1109/BioRob.2012.6290788.

[89] D. Decoster and J. Harari, “Optoelectronic Sensors,” *Optoelectronic Sensors*, pp. 42–43, 2010, doi: 10.1002/9780470611630.

[90] A. Pini, “The basics of photodiodes and phototransistors and how to apply them.” [Online]. Available: https://www.digikey.co.uk/en/articles/the-basics-of-photodiodes-and-phototransistors-and-how-to-apply-them

[91] B. Jia, L. He, G. Yan, and Y. Feng, “A differential reflective intensity optical fiber angular displacement sensor,” *Sensors (Switzerland)*, vol. 16, no. 9, 2016, doi: 10.3390/s16091508.

[92] P. Polygerinos, L. D. Seneviratne, and K. Althoefer, “Modeling of light intensity-modulated fiber-optic displacement sensors,” *IEEE Trans Instrum Meas*, vol. 60, no. 4, pp. 1408–1415, 2011, doi: 10.1109/TIM.2010.2085270.

[93] L. Yuan, X. Lin, Y. Liang, and Y. Jiang, “Applications of angled-mirror in ÿber-optic sensors,” vol. 32, pp. 255–260, 2000.

[94] P. Puangmali, K. Althoefer, and L. D. Seneviratne, “Mathematical modeling of intensity-modulated bent-tip optical fiber displacement sensors,” *IEEE Trans Instrum Meas*, vol. 59, no. 2, pp. 283–291, 2010, doi: 10.1109/TIM.2009.2023147.

[95] Y. Li, K. Guan, and Z. Hu, “Fiber optic displacement measurement model based on finite reflective surface,” *Opt Laser Technol*, vol. 84, pp. 32–39, 2016, doi: 10.1016/j.optlastec.2016.03.031.

[96] I. B. Wanninayake, P. Dasgupta, L. D. Seneviratne, and K. Althoefer, “Modeling and optimizing output characteristics of intensity modulated optical fiber-based displacement sensors,” *IEEE Trans Instrum Meas*, vol. 64, no. 3, pp. 758–767, 2015, doi: 10.1109/TIM.2014.2347694.

[97] D. Osman, X. Du, W. Li, and Y. Noh, “An Optical Joint Angle Measurement Sensor based on an Optoelectronic Sensor for Robot Manipulators,” *2020 8th International Conference on Control, Mechatronics and Automation, ICCMA 2020*, pp. 28–32, 2020, doi: 10.1109/ICCMA51325.2020.9301526.

[98] R. Li and H. Qiao, “A Survey of Methods and Strategies for High-Precision Robotic Grasping and Assembly Tasks - Some New Trends,” *IEEE/ASME Transactions on Mechatronics*, vol. 24, no. 6, pp. 2718–2732, 2019, doi: 10.1109/TMECH.2019.2945135.

[99] T. Mańkowski, J. Tomczyński, K. Walas, and D. Belter, “Put-hand—hybrid industrial and biomimetic gripper for elastic object manipulation,” *Electronics (Switzerland)*, vol. 9, no. 7, pp. 1–26, 2020, doi: 10.3390/electronics9071147.

[100] S. Mathis, “Resolution, accuracy and precision of encoders,” *Assembly*, vol. 62, no. 10, p. 2020, 2019.

[101] B. Lukic, K. Jovanovic, and T. B. Sekara, “Cascade Control of Antagonistic VSA-An Engineering Control Approach to a Bioinspired Robot Actuator,” *Front Neurorobot*, vol. 13, no. September, pp. 1–15, 2019, doi: 10.3389/fnbot.2019.00069.

[102] D. G. Lee and T. W. Seo, “Lightweight multi-DOF manipulator with wire-driven gravity compensation mechanism,” *IEEE/ASME Transactions on Mechatronics*, vol. 22, no. 3, pp. 1308–1314, 2017, doi: 10.1109/TMECH.2017.2681102.

[103] C. Michael, “BURNISHING AND ADHESIVE WEAR OF AN ELECTRICALLY CONDUCTIVE POLYESTER-CARBON Experiments were carried out to examine the friction and wear behavior of an electrically conductive polyester-carbon film during small ampli- tude reciprocating sliding against,” vol. 132, pp. 265–285, 1998.

[104] G. Palli and S. Pirozzi, “An optical joint position sensor for anthropomorphic robot hands,” *Proc IEEE Int Conf Robot Autom*, pp. 2765–2770, 2013, doi: 10.1109/ICRA.2013.6630958.

[105] F. Li, “DESIGN AND ANALYSIS OF A FINGERTIP STEWART PLATFORM FORCE/TORQUE SENSOR,” Simon Fraser University, 1998.

[106] D. Osman, X. Du, W. Li, and Y. Noh, “An Optical Joint Angle Measurement Sensor based on an Optoelectronic Sensor for Robot Manipulators,” in *2020 8th International Conference on Control, Mechatronics and Automation, ICCMA 2020*, Institute of Electrical and Electronics Engineers Inc., Nov. 2020, pp. 28–32. doi: 10.1109/ICCMA51325.2020.9301526.

[107] B. He *et al.*, “Optoelectronic-Based Pose Sensing for a Hand Rehabilitation Exoskeleton Continuous Structure,” *IEEE Sens J*, vol. 22, no. 6, pp. 5606–5615, Mar. 2022, doi: 10.1109/JSEN.2022.3147227.

[108] G. Palli and S. Pirozzi, “An optical joint position sensor for anthropomorphic robot hands,” *Proc IEEE Int Conf Robot Autom*, pp. 2765–2770, 2013, doi: 10.1109/ICRA.2013.6630958.

[109] Z. Zhang, J. Shang, C. Seneci, and G. Z. Yang, “Snake robot shape sensing using micro-inertial sensors,” *IEEE International Conference on Intelligent Robots and Systems*, pp. 831–836, 2013, doi: 10.1109/IROS.2013.6696447.

[110] A. Schmitz, A. J. Thompson, P. Berthet-Rayne, C. A. Seneci, P. Wisanuvej, and G. Z. Yang, “Shape sensing of miniature snake-like robots using optical fibers,” *IEEE International Conference on Intelligent Robots and Systems*, vol. 2017-Septe, pp. 947–952, 2017, doi: 10.1109/IROS.2017.8202259.

[111] D. Osman, W. Li, X. Du, T. Minton, and Y. Noh, “Miniature Optical Joint Measurement Sensor for Robotic Application Using Curvature-Based Reflecting Surfaces,” *IEEE Sens Lett*, vol. 6, no. 5, 2022, doi: 10.1109/LSENS.2022.3169915.

[112] A. D. Gaikwad, J. P. Gawande, and A. K. Joshi, “An intensity-modulated optical fiber sensor with concave mirror for measurement of displacement,” vol. 42, no. December, pp. 300–306, 2013, doi: 10.1007/s12596-013-0143-z.

[113] A. D. Gaikwad, J. P. Gawande, A. K. Joshi, and R. H. Chile, “An Intensity-Modulated Optical Fibre Displacement Sensor with Convex Reflector,” *International Journal of Advanced Research in Electrical, Electronics and Instrumentation Engineering*, vol. 1, no. 1, pp. 29–35, 2012, [Online]. Available: www.ijareeie.com

[114] D. Osman, X. Du, W. Li, and Y. Noh, “Development of an Optical Shape Sensing Method Using Optoelectronic Sensors for Soft Flexible Robotic Manipulators in MIS,” *IEEE Trans Med Robot Bionics*, vol. 4, no. 2, pp. 343–347, 2022, doi: 10.1109/TMRB.2022.3155200.

[115] D. Osman, X. Du, T. Minton, and Y. Noh, “Shape Sensing for Continuum Robotics using Optoelectronic Sensors with Convex Reflectors,” *Electronics (Basel)*, 2024, doi: doi:10.36227/techrxiv.22637704.v1.

[116] R. J. Roesthuis, S. Janssen, and S. Misra, “On using an array of fiber Bragg grating sensors for closed-loop control of flexible minimally invasive surgical instruments,” *IEEE International Conference on Intelligent Robots and Systems*, pp. 2545–2551, 2013, doi: 10.1109/IROS.2013.6696715.

[117] A. Degani, H. Choset, A. Wolf, and M. A. Zenati, “Highly articulated robotic probe for minimally invasive surgery,” *Proc IEEE Int Conf Robot Autom*, vol. 2006, no. May, pp. 4167–4172, 2006, doi: 10.1109/ROBOT.2006.1642343.

[118] R. Das, B. Saravana Prashanth Murali, P. Stefano, and M. Barbara, “Laparoscopic Tissue Retractor Based on Local Magnetic Actuation,” *IEEE International Conference on Soft Robotics (RoboSoft)*, 2015.

[119] W. Yaming *et al.*, “An inspection continuum robot with tactile sensor based on electrical impedance tomography for exploration and navigation in unknown environment,” *Industrial Robot*, vol. 47, no. 1, pp. 121–130, 2020, doi: 10.1108/IR-06-2019-0132.

[120] X. Dong *et al.*, “Continuum Robots Collaborate for Safe Manipulation of High-Temperature Flame to Enable Repairs in Challenging Environments,” *IEEE/ASME Transactions on Mechatronics*, vol. 27, no. 5, pp. 4217–4220, 2022, doi: 10.1109/TMECH.2021.3138222.

[121] R. Das, S. P. Murali Babu, S. Palagi, and B. Mazzolai, “Soft Robotic Locomotion by Peristaltic Waves in Granular Media,” *2020 3rd IEEE International Conference on Soft Robotics, RoboSoft 2020*, no. April, pp. 223–228, 2020, doi: 10.1109/RoboSoft48309.2020.9116032.

[122] B. Liu, Y. Ozkan-Aydin, D. I. Goldman, and F. L. Hammond, “Kirigami skin improves soft earthworm robot anchoring and locomotion under cohesive soil,” *RoboSoft 2019 - 2019 IEEE International Conference on Soft Robotics*, pp. 828–833, 2019, doi: 10.1109/ROBOSOFT.2019.8722821.

[123] C. Tang *et al.*, “A pipeline inspection robot for navigating tubular environments in the sub-centimeter scale,” *Sci Robot*, vol. 7, no. 66, 2022, doi: 10.1126/scirobotics.abm8597.

[124] “Rolls-royce to accelerate future aerospace technologies with ATI programme.” [Online]. Available: https://www.rolls-royce.com/media/press-releases/2020/02-11-2020-intelligentengine-rr-to-accelerate-future-aerospace-technologies-with-ati-programme.aspx

[125] “utmel electronic - TMG4903.” [Online]. Available: https://www.utmel.com/pdf/datasheets?PdfFile=r/datasheets/ams-tmg49033-datasheets-2416.pdf&product=ams-tmg49033-6099502

[126] “Vishay VCNT2020.” [Online]. Available: https://4donline.ihs.com/images/VipMasterIC/IC/VISH/VISH-S-A0020274177/VISH-S-A0020285513-1.pdf?hkey=6D3A4C79FDBF58556ACFDE234799DDF0

[127] "VISHAY TCRT5000L." [Online]. Available: https://www.arrow.com/en/products/tcrt5000l/vishay

[128] "Altech - photodiode." [Online]. Available: https://www.ebee.com/product-detail/Altech-655-4955-001_805687.html

[129] "ONSEMI QRE1113." [Online]. Available: https://docs.rs-online.com/ea75/0900766b810e25b7.pdf

[130] "Inductive proximity sensor." [Online]. Available: https://www.leocom.kr/datasheets/340798_6259.pdf

[131] "Capacitive proximity sensors." [Online]. Available: https://www.micro-epsilon.in/fileadmin/download/products/cat--capaNCDT--en.pdf

[132] "US proximity sensor." [Online]. Available: https://www.microsonic.de/en/about-microsonic/novelties/news.htm

[133] S. Guerbaoui, "Hall effect magnetic sensor." [Online]. Available: https://prod-edam.honeywell.com/content/dam/honeywell-edam/sps/siot/en-us/products/sensors/magnetic-sensors/omnipolar-position-sensor-ics/nanopower-series/documents/sps-siot-nanopower-series-datasheet-50095501-c-en-ciid-149711.pdf

[134] "Inertial Sensor." [Online]. Available: https://files.seeedstudio.com/wiki/Grove-6-Axis_AccelerometerAndGyroscope/res/LSM6DS3TR.pdf

[135] "Rotary encoder." [Online]. Available: https://docs.broadcom.com/doc/AV02-1584EN

[136] "Resistive strip sensor." [Online]. Available: https://docs.rs-online.com/8e1a/A700000011099021.pdf

[137] D. Osman, W. Li, X. Du, T. Minton, and Y. Noh, "Miniature Optical Joint Measurement Sensor for Robotic Application Using Curvature-Based Reflecting Surfaces," *IEEE Sens Lett*, vol. 6, no. 5, 2022, doi: 10.1109/LSENS.2022.3169915.

[138] D. Osman, W. Li, X. Du, T. Minton, and Y. Noh, "Prototype of An Optoelectronic Joint Sensor Using Curvature Based Reflector for Body Shape Sensing," *BHI-BSN 2022 - IEEE-EMBS International Conference on Biomedical and Health Informatics and IEEE-EMBS International Conference on Wearable and Implantable Body Sensor Networks - Proceedings*, pp. 1–4, 2022, doi: 10.1109/BSN56160.2022.9928463.